Optical investigations of low-dimensional semiconductor structures

Daniel James Sercombe

Department of Physics and Astronomy

University of Sheffield

A thesis submitted for the degree of

Doctor of Philosophy

September 2013

I would like to dedicate this thesis to my supportive parents

Sam and Vivienne

and my girlfriend Amy for being so patient.

Acknowledgements

I would like to acknowledge and sincerely thank my supervisor, Alexander Tartakovskii (Sasha), for giving me the opportunity to do this PhD and for helping me through the last three years. I would also like to thank Prof. Maurice Skolnick, whose group leadership has allowed me to learn about and understand other areas of research as well as my own. I would particularly like to express thanks to Odilon Couto and Evgeny Chekhovich for their expert teaching, without which I would not have got so far, as well as their friendship and support. I would also like to thank EPSRC for providing me with the funding.

I would like to thank my fellow students; S. Schwarz, O. Del Pozo-Zamudio, F. Liu and J. Puebla, all of whose hard work and dedication informed the success of this project. I would like to acknowledge and thank M. Sich and I. Luxmoore for helping to measure data and for providing experience of time resolved spectroscopy and finally our collaborators B. J. Robinson and O. Kolosov at the University of Lancaster, L. Otubo at the Instituto de Pesquisas Energeticas e Nucleares IPEN and H.Y. Liu at UCL.

I would like to thank all my friends and colleagues in the LDSD who I have not already mentioned for making my time in Sheffield so pleasant. In particular I would like to thank A.M. Fox, L.R. Wilson, M.N. Makhonin, A. Ramsay , P. M. Walker, D.M. Whittaker, Chris, John Q, John B, Jasmin, Rikki, James, Scott, Ben, Andrew, Lloyd, Deivis, Maksym, Andreas, Nathan, Tim, Romain, Nikola, Magda and Rob; the staff of the EPSRC National Centre for III-V Technologies in particular, Rob Airey, K. Kennedy and John Milner. I would also like to thank the cryogenics and workshop staff C. Vickers, P. Robinson, P. Kemp-Russell and Simon Dixon.

Thanks are due also to my friends outside of the LDSD: Tom Dymond, Emma Parr, Laura Rhodes, Sophy Appleby, Joe Roberts, Rik Bailey, Ross Carter, Sujit Kumarasinghe, Hannah Gibbs, Liz Double, Toni, Bob, Tammy, Gaz, Jamie, Dan, Bethan, Rhian, Ana, Katie, Olive, Matt, my girlfriend Amy and my loving parents!

Daniel Sercombe

Sheffield, 2013.

Abstract

This thesis discusses two optical emitters, gallium arsenide (GaAs) nano-wires (NWs) and 2D molybdenum disulfide (MoS_2) films, which have the potential to be integrated into silicon (Si) and graphene based electronics. Optical properties of these systems are studied using a combination of micro-photoluminescence spectroscopy (μ-PL) and microscopy techniques to understand the effects of structure and environment on light emission. Firstly, it is demonstrated that GaAs NWs can be grown directly on Si using molecular beam epitaxy (MBE). By applying a capping material to the NW surface, in this case GaAsP, we achieve an enhancement of emission yield of up to 10^4, as well as a method of controlling emission wavelength through the application of lattice strain. The second part of this thesis concerns 2D sheets of MoS_2 under 5 atomic layers thick, a direct bandgap semiconductor which can be integrated into graphene electronics. A method for producing these films is discussed which utilises breaking of Van der Waals forces between atomic planes using the mechanical cleavage technique. In this work we show that the shape of PL emission from MoS_2 is heavily effected by the level of doping in the film, which is in turn influenced by interactions with dielectric environments. In the final section of this thesis the problem of irregular emission spectra is addressed and reproducibility of emission properties is found to increase with the deposition of a dielectric capping layer on the MoS_2 surface. By utilising the subsurface microscopy technique Ultrasonic Force Microscopy, we show this improvement occurs due to increased mechanical bonding between MoS_2 and the SiO_2 substrate, which increases the stability of the charge environment.

Publication List

Effect of a GaAsP shell on the optical properties of self-catalyzed GaAs nanowires grown on silicon
O. D. D. Couto, **D. Sercombe**, J. Puebla, L. Otubo, I. J. Luxmoore, M. Sich, T. J. Elliott, E. A. Chekhovich, L. R. Wilson, M. S. Skolnick, H. Y. Liu, A. I. Tartakovskii
Nano Letters 12 10 52695274 (2012)

Dielectric surface and capping effects on optical properties of a few atomic monolayer thick MoS_2
D. Sercombe, S. Schwarz, Del Pozo-Zamudio, F. Liu, B. J. Robinson, E. A. Chekhovich, I. I. Tartakovskii, O. Kolosov, and A. I. Tartakovskii
arXiv preprint arXiv:1304.7221 (2013).

Optical Properties Of High Quality GaAs/GaAsP Core-shell Nanowires on Silicon
D. Sercombe, O. D. D. Couto Jr., J. Puebla, I. J. Luxmoore, M. Sich, L. R. Wilson, M. S. Skolnick, H. Y. Liu, A. I. Tartakovskii
Presented as a poster at Quantum Dot Day, UCL, London, UK (2012)

Photoluminescence Studies Of Thin Film MoS_2
D. Sercombe, O. Del Pozo, E A Chekhovich, F.P Quacquarelli, A. I. Tartakovskii, M.S. Skolnick
Presented as a poster at UK Semiconductors (conference), Sheffield, UK (2012)

Dielectric substrate and capping effects on optical properties of a few atomic monolayer MoS_2 sheets (I)
D. Sercombe, S. Schwarz, Del Pozo-Zamudio, F. Liu, B. J. Robinson, E. A. Chekhovich, I. I. Tartakovskii, O. Kolosov, and A. I. Tartakovskii
Presented as a poster at Graphene Week, Chemnitz, Germany (2013)

Dielectric substrate and capping effects on optical properties of a few atomic monolayer MoS_2 sheets (II)
D. Sercombe, S. Schwarz, Del Pozo-Zamudio, F. Liu, B. J. Robinson, E. A. Chekhovich, I. I. Tartakovskii, O. Kolosov, and A. I. Tartakovskii
Presented as a poster at EP2DS-MSS, Wroclaw, Poland (2013)

Contents

List of Figures

Chapter 1

Background and motivation

1.1 Introduction

Modern electronics rely on logic circuits based on silicon field effect transistors developed for the first time in the 1950s (1, 2). Current technological goals focus on improving speed, cost, power consumption and miniaturization of circuit applications and the direct integration of photonics (3). This is a wide area of research which covers advances in fields such as spintronics (4), photonics (5), quantum computing (6, 7) and graphene based electronics (8). Another large area of semiconductor research concerns photovoltaics (9, 10). The generation of electrical power by conversion of solar radiation may be an important step in developing greener alternatives to fossil fuels (11). Research into these areas require a strong understanding of the properties of semiconductor materials, structures and devices (12). Novel nano-structures are at the forefront of research and these include quantum dots (13, 14), quantum nanowires (9, 15), quantum wells (16, 17) and atomic monolayers (8, 18).

This thesis focuses on the effects of crystalline structure and environment on

electronic and optical properties of semiconductor nano-structures. This is studied using a combination of optical spectoscopy and various microscopy techniques. The microscopy techniques used are transmission electron microscopy (TEM), scanning electron microscopy (SEM), atomic force microscopy (AFM) and ultrasonic force microscopy (UFM). Optical properties are studied using continuous wave (CW) and time resolved (TR) micro-photoluminescence spectroscopy (PL). The first part of this thesis covers GaAs nano-wires grown directly on silicon wafers and the second half covers optical properties of thin films of MoS_2, a material which recently was shown to have a transition to direct band-gap for few atomic monolayer thicknesses (19, 20).

1.2 III-V nanowires grown on silicon substrates

Nanowires (NWs) are a one dimensional nano-structure with a high length to diameter aspect ratio. Due to low dimensions NWs exhibit unique optical and electronic properties different from the bulk material. In this chapter we review interest in III-V semiconductor NWs which have potential uses in optoelectronics (21, 22) and photovoltaics (9, 23, 24). We focus on the integration of III-V NWs onto silicon substrates as this has the potential to significantly reduce the cost of devices. In particular we highlight the advantages of growing these NWs using a recently developed catalyst free molecular beam epitaxy (MBE) method. We then discuss the effects that crystalline structure, determined during growth, and the addition of a nanowire shell has on photoluminescence. In Chapter 3 we continue work on nanowires by investigating, for the first time, the optical properties of GaAs/GaAsP core-shell nanowires grown by this method on Si substrates.

1.2.1 Interest in III-V Nanowires grown on silicon

III-V materials, such as GaAs, GaN, InAs and InP, are direct bandgap semiconductors and therefore have bright photoluminescence (PL) and electroluminescence (12, 25, 26, 27). This property, discussed in more detail in section 2, has therefore allowed III-V materials to form the basis of many optoelectronic devices (21, 28, 29). Although so far no commercial devices based on III-V nanowires (NWs) are available (21), optical devices such as light emitting diodes (LEDs) (30, 31), electrically driven lasers (32) and photon detectors (33) have already been developed for research purposes. Growing nanowire heterostructures with embedded quantum dots may also be an important step for controlling the posi-

tion and dimensions of III-V quantum dots in photonic structures (34, 35, 36).

Current electronics are based on silicon technology because this is cost effective to produce (37). Si is an indirect band-gap material and therefore has only very weak optical emission (25). Integrating more expensive III-V photonics directly into silicon devices is therefore advantageous but it is difficult to achieve due to lattice mismatch, which is particularly large in the case of GaAs studied here (38). This leads to the formation of dislocations (39) between epitaxial layers during deposition and overcoming this require complicated growth patterns with limited success (40) or wafer bonding which is a costly process (41). III-V semiconductor NWs are naturally less reliant on lattice matching with the growth substrate as the narrow NW diameter allows radial variations which relieve strain without forming dislocations (22). Growing NWs directly on Si may therefore provide a future cost effective method for direct integration of III-V photonics into Si electronics (22).

NWs have been earmarked for future use in efficient photovoltaics. The global demand for energy is increasing rapidly and predicted to hit 30TW by 2050, double the current value (42), and solar energy is one of the most promising renewable energy sources. The main disadvantage of current solar devices is that they have unsustainably high production costs (43) compared to an extremely low efficiency of light-to-electricity conversion (44). The limit on efficiency for current p-i-n devices is only $\sim$30%. There are therefore two criteria for creating new sustainable devices, increasing efficiency and reducing costs. The efficiency of current devices is limited by the ray optics limit, which is the minimum thickness needed to fully absorb the solar spectrum (45). The high length-to-diameter ratio of NWs allows a tailored thickness to enhance optical absorption (44) and

therefore exceed this ray optics limit (46). This is particular promising when considering dense NW arrays (43). The small dimension of NWs also allows for small electron collection lengths which also heavily effects the efficiency of current devices (9, 46).

Recent developments in growing III-V NWs directly onto silicon and also exceptional new results showing up to 71% efficiency for absorbed light converted to electrical current in a single NW (46) may therefore point towards a future for producing highly efficient and cost effective photovoltaics (10, 23).

1.2.2 Fabrication of III-V nanowires, with a focus on growth on silicon.

Good quality NWs for use in photonics and photovoltaics require well controlled dimensions. For example, variations in axial width can lead to effects such as inhomogeneous broadening of photoluminescence (PL) emission (described in section 2.1). Stacking defects can act as charge traps (47) which will effect radiative recombination and photovoltaic efficiency. The structure of NWs is further complicated as two different crystal lattices, zinc-blend (ZB) and wurtzite (WZ), can form (47, 48). These have a different band-gap and therefore greatly effect electronic and optical properties of the NW, as discussed in section 1.2.3.

The most common process for NW growth is by a vapour-liquid-solid (VLS) phase process (22). This was originally demonstrated for Si NWs in 1964 (49) and is described in figure 1.1. A catalyst (in this case, a gold nano-particle) is deposited on the surface of a Si(111) substrate. The size of the nano-particle is important as this determines the width of the NW. The temperature of the

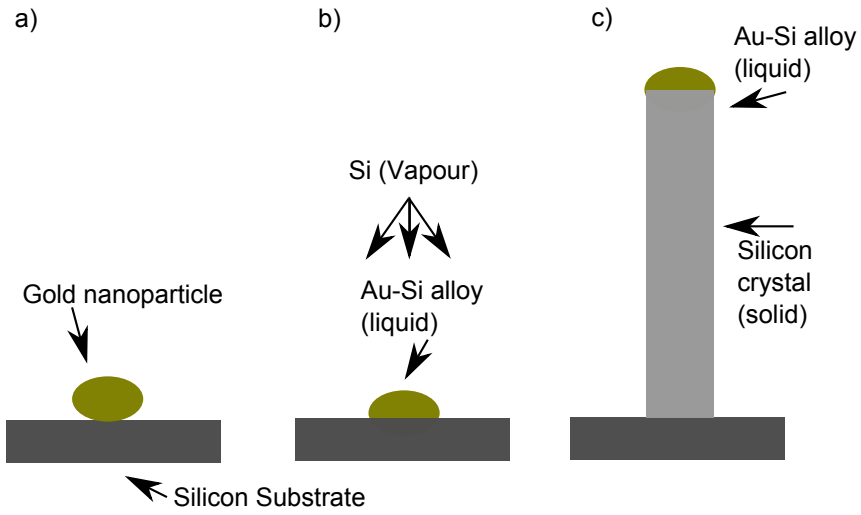

Figure 1.1: A diagram demonstrating the growth of silicon NWs using the vapour-liquid-solid (VLS) method. (a) Firstly, gold particles are deposited on the substrate to act as catalysts for growth. (b) High temperatures melt the Au particles, creating a liquid phase. The growth constituent Si, in a vapour form, is directed at the substrate by either MBE or MOVPE. (c) Si vapour is absorbed by the liquid Au forming a solution. When this solution becomes super-saturated a solid layer is deposited beneath the Au eventually forming a NW.

substrate is then raised and the gold nano-particle melts. To begin growth, Si is released into the growth chamber in a vapour-phase. This is commonly achieved by either molecular beam epitaxy (MBE) (50) or metalorganic chemical vapour deposition (MOVPE) (38). The Si vapour is then absorbed by the liquid gold forming a solution. As more vapour is added, the solution becomes supersaturated and Si is deposited in the interface between the gold and the substrate. By continuing to feed supersaturation a solid NW will grow beneath the liquid-phase of the catalyst. Radial growth of NWs (which causes effects such as tapering) can be kinetically controlled by using high temperatures and also by controlling the rate of deposition (38).

This method can be adapted to grow III-V material NWs directly onto Si, such

as GaP (38), InAs (51) and GaAs (50). By changing the constituent elements, heterostructure NWs with embedded quantum dots can be achieved (35, 36). Gold nano-particle assisted growth is currently the most common method used in research (22). A high accuracy, low defect density and narrow diameter down to 20nm (38) has been achieved. However, the gold catalyst can contaminate the purity of the crystal structure (42) which will likely affect electrical properties and may have adverse effects on photovoltaics. There is therefore a current drive to develop catalyst-free growth methods which have comparable quality and growth control.

The first catalyst free method demonstrated for III-V NWs on Si uses the deposition of a thin organic film to create growth sites on the substrate (52). The Si substrate is firstly HF etched to remove all oxides from the surface. Organic material is then deposited by spin coating and forms a natural mask where small nm regions are covered. The Si surface is then allowed to oxidise again, except in the regions covered by organic material. The sample is placed in a vacuum to remove remaining organic material by in-situ annealing. When III-V elements are released by MOVPE, they diffuse across the SiO_2 surface and form clusters in the less oxide regions where the polymer was, which act as growth sites for NWs. III-V materials grown on Si by this method include InAs (52, 53) and GaAs (54). Unfortunately NWs grown by this method are found to have relatively larger diameters (50nm+) and uncontrollable stacking defects (53).

A more recently demonstrated self-seeded MBE growth method (55) may therefore be the next step in developing catalyst free III-V semiconductors on silicon. This growth utilises the VLS method described above, but instead of a Au nanoparticle a droplet of a constituent element is used. So far this has only

been demonstrated for GaAs NWs (55, 56, 57, 58) and the constituent used in this case is always Ga. NWs produced by this method have demonstrated good control over crystal structure, low defects and narrow diameters (20nm) similar to gold catalysed methods (56). This is the method we consider in our work, and more details of our growth procedure are presented in Chapter 3.

1.2.3 Structural effects on optical properties of III-V nanowires

In this section we consider structural effects on the PL properties of NWs, looking specifically at results for III-V NWs grown on Si which are available in the literature. We firstly consider the effect of crystal phase polytypes WZ and ZB and then, by considering core-shell structures, we explore the effect of surface states on NWs. These observations are directly relevant to observations made in our work on catalyst free GaAs and GaAs/GaAsP NWs presented in Chapter 3.

1.2.3.1 Effect of crystal phase polytypes on optical properties of III-V nanowires

The crystalline structure of bulk GaAs is zinc-blend (ZB). A ZB structure is formed from two interpenetrating rather than face centred cubic (FFC) lattices of different elements which are displaced relative to each other in the [111] direction as depicted in figure 1.2a. In NWs a different lattice structure, Wurtzite (WZ), can also occur (47, 48). WZ forms from two hexagonal close packed (HCP) elemental lattices, rather that FFC, which are also interpenetrating as shown in figure 1.2b. In the (111) crystal direction these have different stacking structures,

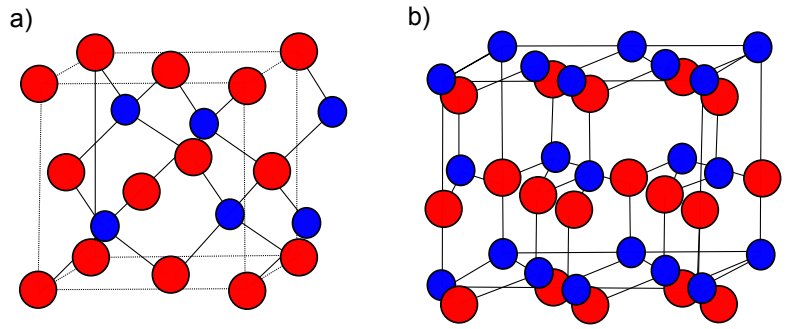

Figure 1.2: Diagrams showing the crystal structure of (a) zinc-blende and (b) wurtzite phases. The crystal lattice of zinc-blende is face centre cubic and the crystal lattice of wurtzite is hexagonal close packed.

which are ABCABC stacked for ZB and ABABAB for WZ (59) where A, B and C are repeating stacking structures. The phase of the entire NW crystal, or the density of ZB/WZ planes, can be controlled during both Au and catalyst free VLS growth techniques by varying the vapour-phase deposition speed and temperature (22, 56).

There is a 115meV offset between the band edges of ZB and WZ and quantum confinement can occur, along the NW length, between different sections if both are present (47, 60). In this case holes are confined in the valence band of WZ segments and electrons in the conduction of ZB segments (61) as shown in figure 1.3. Electrons and holes are therefore spatially separated and this is known as type-II confinement. For NWs where the radius of the NW is smaller than the radius of excitons, quantum confinement can also occur radially. In structures where both types of confinement occur strongly, the electron will be effectively confined in three dimensions in a system which has been dubbed as a crystal phase quantum dot. This has been observed for VLS Au assisted grown InP NWs (62).

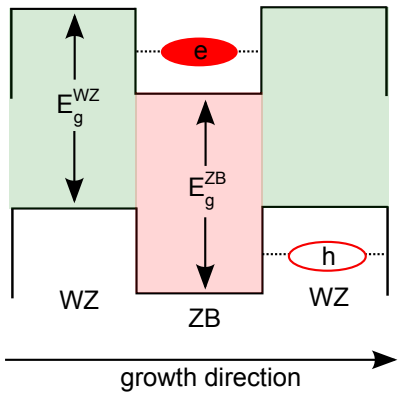

Figure 1.3: A diagram demonstrating type-II confinement of electrons and holes along the NW growth direction between different crystal phases. The electrons are confined in a ZB section and holes in a WZ section and are therefore spatially separated.

1.2.3.2 Effects of core-shell structures on the properties of III-V nanowires

Radiative recombination of excitons occurs along the NW length. Excitons can also recombine non-radiatively in charge traps on the surface of a semiconductor material (63) and this is expected to be particularly dominant for NWs due to the large surface-to-volume ratio. To reduce the density of surface charge traps NWs are often capped with an additional material to form a core shell nano-structure. A core-shell structure is demonstrated in figure 1.4. The shell is applied in the growth chamber after the VLS process has completed using either MBE or MOVPE. Examples of capping materials used for GaAs NWs include AlGaAs (64, 65), GaP (66) and GaAsP (54, 67).

Direct PL yield comparison between uncapped and core-shell NWs has been presented previously in the case of NWs grown on Si substrates with the aid of a gold catalyst. There is a measured 1 order of magnitude enhancement in PL yield for GaAs/AlGaAs (65) and a 2 order magnitude enhancement for GaAs/GaAsP

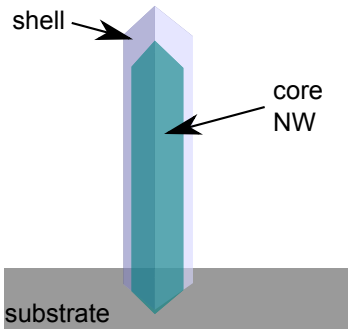

Figure 1.4: A diagram demonstrating a basic core-shell nanostructure. The core is grown by standard VLS methods described in the text. The shell is applied after growth by either MBE or MOVPE depending on the growth chamber.

(67) NWs compared with uncapped GaAs. In these works this is attributed to the capping layer reducing surface traps, something we investigate in greater detail in our work. There is often a lattice mismatch between the capping layer and core within these structures (68). By adding strain to the optically active core, the band-gap can be altered (66, 69, 70). This ability to tune the emission and absorption of NWs may have potential advantages in photonics (22) and photovoltaics (23).

1.2.4 Our work on GaAs and GaAs/GaAsP grown by catalyst free MBE on Si

Although the crystalline quality of catalyst free MBE grown NWs has previously been covered in detail (55, 56, 57), there are so far few reports on the optical properties of NWs grown by this method. This is particularly timely because, as we have discussed above, self-seeded NW growth may offer advantages over the more comprehensively studied Au-seeded NWs as they avoid catalyst contamination. In particular there are no other optical reports on catalyst free

GaAs/GaAsP core-shell structures produced in an MBE system. In Chapter 3 we present new in-situ micro-PL measurements on individual free standing GaAs and GaAs/GaAsP NWs grown by this method and demonstrate the effects of surface and structure on optical properties.

We find that while our uncapped GaAs NWs have a relatively small PL yield, our core-shell GaAs/GaAsP NWs have, in comparison, a PL yield enhancement exceeding 2000x. We observe that the addition of the GaAsP capping layer in our core shell structures leads to a reduction in the efficiency of thermal activation for non-radiative processes by a factor of 8, suggesting that these states are on the NW surface. We also find that additional charge traps can form on the surface of an uncapped NW which is exposed to air, a process we attribute to oxidation. Both of these observations therefore provide evidence that a weak PL yield in uncapped GaAs NWs is due to the effects of non-radiative surface states.

Unlike uncapped GaAs NWs, our core-shell GaAs/GaAsP NWs emit a bright PL signal up to room temperature. By considering the activation of PL quenching mechanisms with temperature, we demonstrate a new quenching process at high temperature which we attribute to electrons escaping from the GaAs core into the GaAsP shell. We also find that the addition of GaAsP shell imparts strain on the NW core, which is evident due to a blue shift of PL above the band gap of zinc blende GaAs. Varying the nominal concentration of P in the capping shell may prove to be a useful method for strain-tuning the NW band-gap.

Additionally, to surface effects and strain, we demonstrate the effect of type-II confinement, between WZ and ZB, for NWs grown by our method. This is concluded from relatively long lifetimes measured and also a shift in emission energy below the value for GaAs ZB, which reflects a previously accepted 115meV

band offset between GaAs WZ and ZB. The PL lifetime measured is 7.4ns for type-II confinement. For NWs grown at a slightly higher temperature (640^{o}C compared to 635^{o}C) we find pure ZB phase structures with lifetimes measured at 1.43ns.

1.3 MoS_2, a new direct band-gap semiconductor

Since its discovery, graphene has been suggested as the next step in developing high speed electronics due to its large conductivity (8, 71). There is a large family of other 2D materials that can be prepared similarly to graphene in a quasi-2D form including MoS_2 (19), $MoTe_2$ (72), WS_2 (73), boron nitride (74) and many more. Future devices may rely on combining electronic properties of these materials with the large conductivities found in graphene in stacked heterostructures (75, 76, 77, 78). It is therefore important to understand the properties of these materials and in Chapter 4 and 5 we look in detail specifically at molybdenum disulfide (MoS_2).

Particular interest in two-dimensional thin films of MoS_2 has formed due to the discovery of an indirect to direct band-gap transition for thicknesses less than 10 atomic layers, leading to observed bright photo-luminescence (PL) (19, 20) as well as attractive field effect transistor (FET) behaviour (79, 80, 81, 82, 83). A high Earth abundance of the material (80), relative inexpense and ease of production of 2D structures (84) make MoS_2 a desirable material for both research and potential industrial applications. The demonstration of optical valley polarization (85, 86, 87, 88) and high flexibility and strain tuning (89) suggest future applications in valleytronic devices and flexible electronics respectively; and bright PL emission may be used in optoelectronics (90).

In this section we discuss the recent interest in the optical and electronic properties of MoS_2 by reviewing the work available in literature. Our work on MoS_2 is continued in Chapter 4 and 5 where we explore in detail the processes

that influence the shape of PL spectra with a particular emphasis on interactions with Si/SiO_2 substrates. Functionality of MoS_2 as a lubricant (91), catalyst (92) and in nanotube form (93) have also been demonstrated but are beyond the scope of this work.

1.3.1 Structural properties of MoS_2

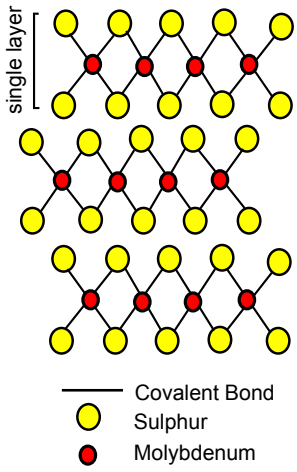

Figure 1.5: (a) A simplified diagram of the structure of MoS_2. Molybdenum atoms are sandwiched between a layer of Sulphur atoms which they are covalently bonded to. This forms a single layer as labelled. Each subsequent layer is then stacked and bonded by weak Van der Waal interactions.

MoS_2 is a dichalcogenide compound made from transition metal molybdenum (Mo) and chalcogen non-metal sulphur (S). A diagram of the lattice structure of MoS_2 is provided in figure 1.5. It can be seen here that Mo atom is covalently bonded to S forming a single layer where Mo sits in the centre and S at the edges (94). Each subsequent layer is only weakly bonded to surrounding layers by electrostatic dipole forces known as Van der Waals. Due to the weak bonds

between the layers, it is possible to reduce them down to 2D sheets featuring few to a single individual layer known as a monolayer (ML). Exfoliation of MoS_2 will be described in detail in Chapter 4, where we demonstrate the method developed for this project.

The MoS_2 used in this work was from a mineral source of unknown purity. Defects may act as sources of n or p charges within the samples. These impurities can therefore effect the electronic and PL properties. This is particularly important in our work, as we will discuss below, because we find that the spectrum of MoS_2 is dominated by a charged exciton peak.

1.3.2 Electronic properties of thin sheets of MoS_2

Transistors are very important in modern electronics for use in both logic circuits and as radio-frequency amplifiers (37). Metal-Oxide Semiconducting Field Effect Transistors (MOSFET) are currently the most widely used design (12). These feature a source (s) and drain (d) contact connected by a channel (c) where the current flows. The flow of electrons in the channel is controlled by a gate voltage (g) (95). A MOSFET has two modes of operation, on and off. Logic gates used in modern computing are constructed from a series of MOSFETs, which are usually produced on chip. These form the backbone of modern computing.

For good quality logic circuits FET devices require good conductivity (product of charge density and mobility) and high switching described by a good ON/OFF ratio between currents I_{ON} and I_{OFF} (80). A low current is especially desirable for the off state of FETs due to the power saving advantages. Semiconductor materials are highly desirable for use in FET transistors as they have good trans-

port for electrons and low off current due to the fact that electrons need to be promoted across a bandgap before a current can flow (96). The most commonly used semiconductor in modern MOSFET devices is Silicon (12).

A diagram of a typical n-type MoS_2 FET is given in figure 1.6. Here a ML of MoS_2 has been deposited on a p-doped silicon wafer. Au contacts are deposited by electron beam lithography (79). A high-k dielectric such as HfO_2 is deposited between the MoS_2 channel and gate contact to screen coulomb interactions which effect the carrier mobility (81). The width of the MoS_2 channel, where current is allowed to flow, is controlled by creating a capacitance between the gate and substrate, which causes bending of the valence and conduction levels (82). Introducing a sufficiently large positive gate voltage (with respect to the source) pushes the valence band away from the fermi level (driving holes away from the gate) and the conduction band closer populating the MoS_2 with electrons (95). This creates a conducting channel and a current can therefore flow when a voltage is applied between the source and drain (figure 1.6a). Applying a negative voltage has the opposite effect, effectively driving electrons from the semiconductor channel creating a depletion zone (figure 1.6b). In the ideal case no current will flow in this mode regardless of voltage between the source and drain.

With modern technology requiring increasing computing capabilities within smaller devices there is a current industrial drive for miniaturisation of FETs which MoS_2 may fulfil. In III-V materials and silicon reducing the height of the channel reaches a limit where rough interfaces and thickness variations related to growth become an issue; leading to reduced mobility and large threshold voltage variations (8). When reducing the length of a FET channel we therefore reach a limit where the channel length has the same order of magnitude of the

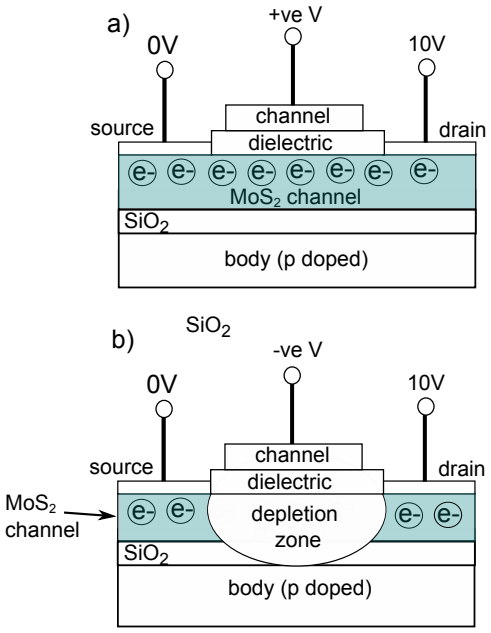

Figure 1.6: Diagrams demonstrating typical n-type MOSFET transistor operation for MoS_2. The MoS_2 channel is deposited on a p-doped substrate. Contacts source, drain and gate are attached. A dielectric material is typically placed between the MoS_2 channel and the gate contact to screen coloumb scattering.(a) Forward bias: a positive voltage is applied to the gate creating a capacitance across the channel. This pushes the valence band away from the fermi-level and the conduction band closer populating the MoS_2 with electrons. When a voltage is a applied between source and drain a current will flow. (b) Reverse bias: A negative voltage is applied to the gate driving electrons out of the MoS_2 channel creating a depletion zone. No current will now flow when a source-drain current is applied.

depletion width of the s-d channel, which creates adverse influences known as short-channel (3). 2D materials such as MoS_2 therefore offer a structural advantage over traditional transistor channel materials due to being near atomically thin and relatively defect free. This potentially allows further miniaturisation before the short channel limit is reached.

ML and bilayer MoS_2 transistors have exhibited excellent on/off ratios of

10^8 (79), with ratios above 10^4 (59, 90) being generally accepted as good for transistor switches. Mobilities in MoS_2 of 200 $cm^2V^{-1}s^{-1}$ (79, 97, 98) have been demonstrated with a limit calculated at 410 $cm^2V^{-1}s^{-1}$ (82). Direct comparisons with silicon transistors in the same dimensions have been performed by Alam *et al.* (82). Here they find a steeper sub-threshold slope (which characterises faster switching between on/off states), reduction in S-D leakage and shorter possible channel lengths in the case of MoS_2. This is, in part, related to the heavier effective mass and this work suggests that MoS_2 is a viable candidate for replacing silicon due to it's improved functionality in small dimensions (99).

1.3.3 Direct band-gap photoluminescence from thin sheets of MoS_2

A bright PL signal is found for thin films of MoS_2. This arises from a change in the material band-structure when compared to thicker sheets (above 10 layers) and bulk. Calculations of the band structure for MoS_2 (20, 100, 101, 102) have demonstrated a shift from an indirect optical bandgap (described in section 2.1) in bulk material to a direct bandgap for a single layer (100).

An example of calculated band structures for (a) bulk, (b) quadrilayer, (c) bilayer and (d) monolayer MoS_2 from the work of Splendiani *et al.* (20) is shown in figure 1.7. In MoS_2 the indirect band-gap in bulk material occurs at the Γ point of the valence band in k-space as can be seen in (a). States at the Γ point are a combination of antibonding p_z orbitals in the S atoms and d orbitals in Mo. In contrast states at the K point (where direct recombination occurs in MoS_2) occur only due to the d orbitals in Mo atoms (80).

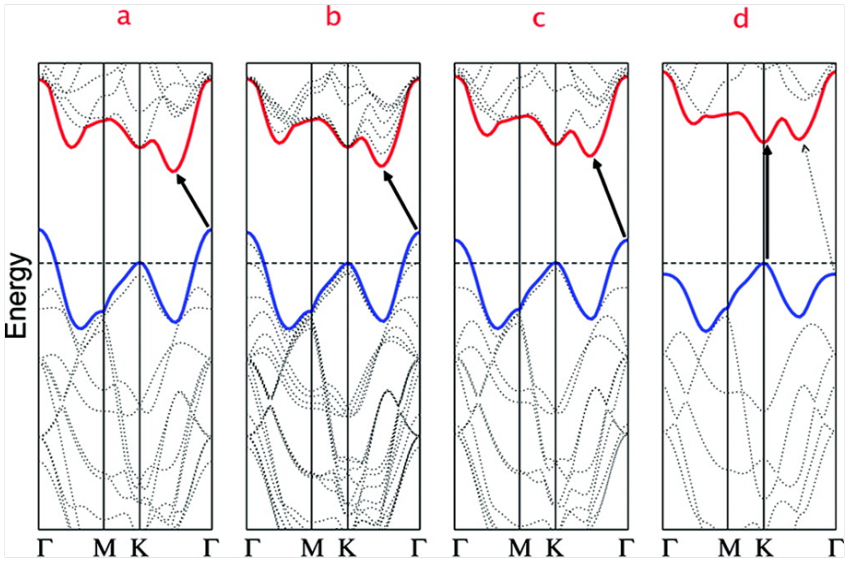

Figure 1.7: Calculated band structures of (a) bulk MoS_2, (b) quadrilayer MoS_2, (c) bilayer MoS_2 and (d) monolayer MoS2. The solid arrows indicate the lowest energy transitions. This work is taken from the paper "Emerging photoluminescence in monolayer MoS_2" by Splendiani *et al.* (20)

The diagram in figure 1.5a shows that the Mo atoms are fairly isolated from interlayer coupling as they are sandwiched in the middle of an S-Mo-S layer. As the K point is influenced only by d orbitals in Mo, it is unaffected by decreasing layer number. The Γ point, on the other hand, is influenced by p_z orbitals in S and is predicted theoretically (80, 94, 101) to increase in energy below the thickness of 10ML as can be seen in figure 1.7(a-d). This increase in energy causes the direct recombination path at the K point to become more energetically favourable and to eventually dominate for a single layer as can be seen in figure 1.7(d).

This means that direct recombination becomes detectable in samples between 1-10ML at the K-point where the minima of the conduction and valence band are in the same position in momentum space. Direct band-gap PL was demonstrated for the first time in these dimensions for MoS_2 by Mak *et. al.* (19) and

Splendiani *et. al* (20) in 2010. They found that with increasing thickness from a single layer the energy gap of the indirect path decreases on a layer-by-layer basis meaning that direct emission becomes less energetically favourable. This results in PL yield from direct recombination decreasing with increasing thickness from a single monolayer, which they measure to be nearly exponential. Subsequent time resolved measurements of emission from the direct band-gap of MoS_2 have shown recombination times of 5ps between 4.5-150K and 70 ps for room temperature (103).

1.3.4 Photoluminescence spectrum of thin sheets of MoS_2

Due to the relative infancy of this field, there are still very few reports focussing on PL from MoS_2 (19, 20, 85, 103, 104) which are always measured for samples deposited on SiO_2 capped Si substrates. A photoluminescence (PL) spectrum for MoS_2 measured in our work is provided in figure 1.8. Rather than a single peak, the spectrum of MoS_2 consists of two bands which are labelled as A and B in red. This is a consistent observation in the literature and it has been shown (101, 105) that these bands originate from emission from two distinct hole positions caused by a splitting of the valence due to spin-orbit coupling at the K-point. These two bands, A and B, are also detected in absorption spectra for bulk MoS_2 (106). The B peak has a much smaller intensity ($\sim$15%) compared to the A peak in PL.

Looking at the spectra in figure 1.8 it can be seen that the A band is formed from emission of different states labelled A^0, A^- and L on the diagram. The observation of A^0 and L varies significantly between publications and are often not observed. There is, in fact, only one other published spectrum where both states

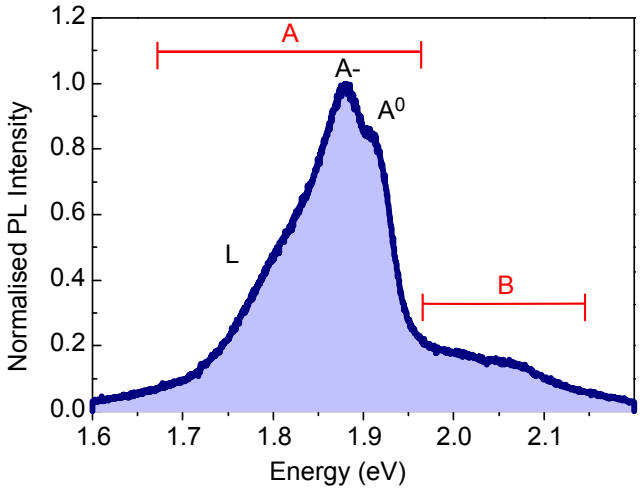

Figure 1.8: An example PL spectra for MoS_2 measured in our work. Emission bands A and B are labelled in red and these occur due to PL recombination from a split valence band. Individual spectral features A^0, A^- and L are labelled in black and discussed in more detail in the text. Our work is only the second publication to show an emission spectra where all these features are visible.

are observed simultaneously (107). Direct observation of A^0 has only previously been discussed by Mak *et. al* (85). By integrating MoS_2 into a FET, they showed that, by varying the bias across the device, the density of charge can be varied within the film. At a bias of -100eV, the situation where the system can be considered free of excess charges, the A^0 peak was only observed in PL spectra. For increasing bias (up to 80 V) charges are introduced and A^- appears while A^0 decreases in intensity. This suggests A^0 corresponds to recombination of a neutral exciton complex and A^- a negativity charged exciton complex.

Emission from low energy shoulder L (103, 108) is also not seen in many spectrum published and its origin is less understood than A^0. It was shown by Korn *et. al* (103) that the L shoulder can be suppressed when an additional material is capped on the MoS_2 surface and they suggest that it is therfore related to emis-

sion from surface states. Specifically they suggest that the L peak is emission related to surface bound impurities, which would cause a localized perturbation of the band-structure.

Polarization properties of PL emission from MoS_2 has also proven interesting. It has been shown experimentally that emission from MoS_2 has the same degree of circular polarization as the laser used for excitation, with results of up to 100% helicity in selected experiments (85, 85, 87, 88, 108). This is interpreted that the electrons in MoS_2 can be optically addressed at the same position in energy, but at different positions in k (momentum) space, known as valleys (85, 87, 88, 108). Optically addressing momentum space therefore may provide yet another degree of freedom for use in producing computational devices (86).

1.3.5 Our work on MoS_2

In our work we develop a method for mechanical exfoliation of MoS_2 onto Si/SiO_2 substrates and we demonstrate PL emission for MoS_2 sheets under 5ML in thickness produced using our method. We find that there is a large variation in the PL emission spectra shape between different samples, which can also be seen in the literature (19, 20, 85, 103) but has not previously been highlighted. In order to explain this we consider the effects of substrate interactions and also the physical processes which determine the relative intensity of the different PL emission features (A^0, A^-, L and B). Using atomic force microscopy (AFM), and a specialised adaptation known as ultrasonic force microscopy (UFM), we present unique images of defects which form in our MoS_2 sheets during exfoliation.

In Chapter 4 we show that competition between radiative and non-radiative

processes effect the behaviour of PL with both temperature and incident power dependence. We find further evidence to support previous results showing a low quantum efficiency in MoS_2 (80), finding that PL emission does not saturate at high pumping powers. Importantly, we find that the dominant effect which determines the variation in emission from states A^-, A^0 and L is the balance of negative charge in the film. We show that negative state, A^-, is dominant for all spectra between 6.5-300K and provide evidence that this is formed due to to charge capturing from the substrate. We find that electrons are thermally activated in the SiO_2 and show that, with increasing temperature, the relative emission intensity of A^0 and L decreases before disappearing.

In Chapter 5 we investigate how to control the charge balance in MoS_2 and therefore the PL line shape. Here we consider the effect of dielectric capping on the PL properties and investigate MoS_2 on substrates with different roughness. We find, using AFM and UFM, that the addition of a capping layer increases the mechanical bonding of the MoS_2 with the substrate, which we find helps to facilitate the charging process and creates a more stable charge balance in the film. This is shown to lead to a suppression of states A^0 and L. The effect of this is to increase the uniformity of PL lineshape, emission energy and linewidth between different samples and also to reduce linewidths. This work therefore provides important results about substrate interactions as well as offering a potential way to improve uniformity of electronic and optical properties of thin MoS_2 sheets.

Chapter 2

Experimental Techniques

In the previous chapter we showed that integration of III-V semiconductor materials with Si electronics may be possible to achieve by growing NWs directly on Si. In this thesis the electronic (optical) and structural properties of a novel system of GaAs and GaAs/GaAsP NWs grown by catalyst free MBE are related for the first time using complimentary techniques of continuous wave photoluminescence (CW-PL), time resolved photoluminescence (TR-PL), scanning electron microscopy (SEM) and transmission electron microscopy (TEM). We also introduced MoS_2, one of a new class of 2D materials which can be prepared similarly to graphene. It has a bright PL spectra and can be used to make transistors. In order to relate the electronic (optical) and structural properties of MoS_2 the complimentary techniques of CW-PL, atomic force microscopy (AFM) and ultrasonic force microscopy (UFM) are undertaken. In this chapter we introduce these techniques individually and also give an introduction to photoluminescence.

2.1 An introduction to the principle of photoluminescence

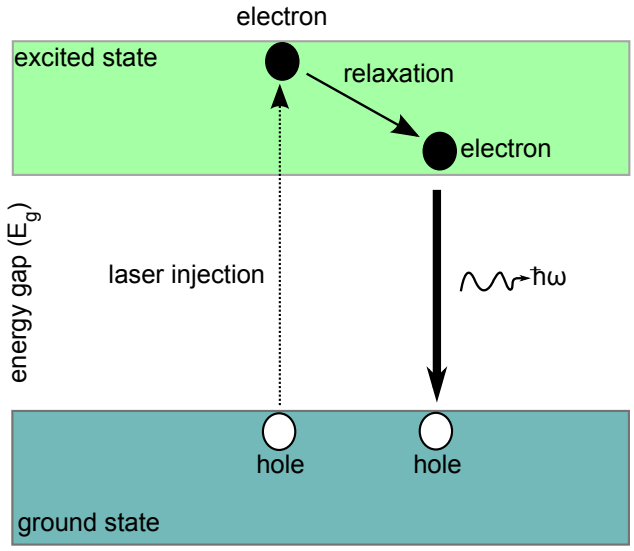

Figure 2.1: Diagram of electron recombination demonstrating laser injection of an electron-hole pair, relaxation of the electron to the minima of the conduction band and recombination resulting in the release of a photon of light.

Photoluminescence (PL) is a photon emission process due to the recombination of an optically created electron hole pair. For PL to occur in a semiconductor the absorption of a laser photon must promote an electron from the valence band to the conduction band (27). For electron promotion to occur the laser photon energy must be the same or higher than the material band-gap. All experiments in this thesis were carried out using non-resonant above band-gap excitation. The radiative recombination of the electron-hole pair may be preceded by a non-radiative relaxation mechanism which leads to the emission of phonons.

Competition between non-radiative and radiative processes is important for both our work on NWs and on MoS_2.

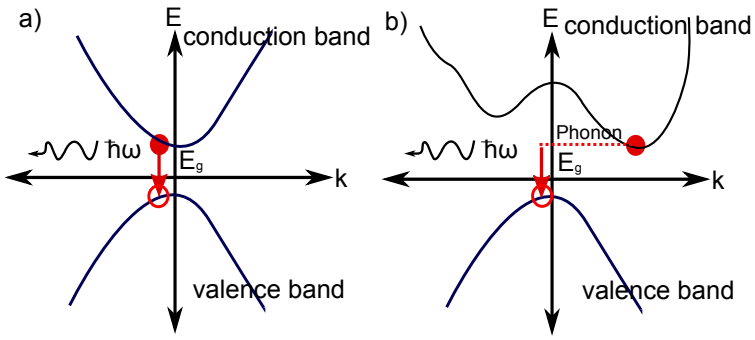

Figure 2.2: Diagrams showing the position of the conduction and valence band minima in momentum space for direct and indirect band-gaps. In this case E is the position in energy and k is the wavevector of the particle. (a) direct band-gap recombination where the electron and hole have the same wavevector. (b) indirect band-gap recombination where the electron and hole have different wavevectors and therefore require addition emission of a phonon before recombining.

Photo-excited electrons (holes) relax to the bottom of the conduction (valence) band by emitting phonons (25). Optical recombination of electon-hole pairs occurs at the energies close to the edge of the band-gap (12). If these band edges occur at the same position of the Brillouin zone in momentum space (ie. have the same wavevector) emission of a photon occurs with conservation of energy and momentum without need for additional processes such as emission of phonons. If they occur at different positions (ie. have different wavevectors), then emission of a particle becomes a second order process and requires additional emission of phonon in order to conserve momentum (26). This is therefore a slower process and produces a lower emission rate of photons. The first order process is characteristic to direct band-gap semiconductors and is found in the case of nanowires and thin sheets of MoS_2 studied in this thesis. Both processes are illustrated in

figure 2.2.

In an atom electrons sit in discrete energy levels and therefore produce a discrete florescence emission spectra with line widths determined by the uncertainty principle (109). In semiconductors the electrons and holes relax into the bottom of the valence and conduction band respectively, forming a thermal distribution before recombining (27). The line width of emission is related to this thermal distribution K_BT, where T is temperature and K_B is the Boltzmann constant, along with the density of states, carrier density and inhomogeneity of the crystal.

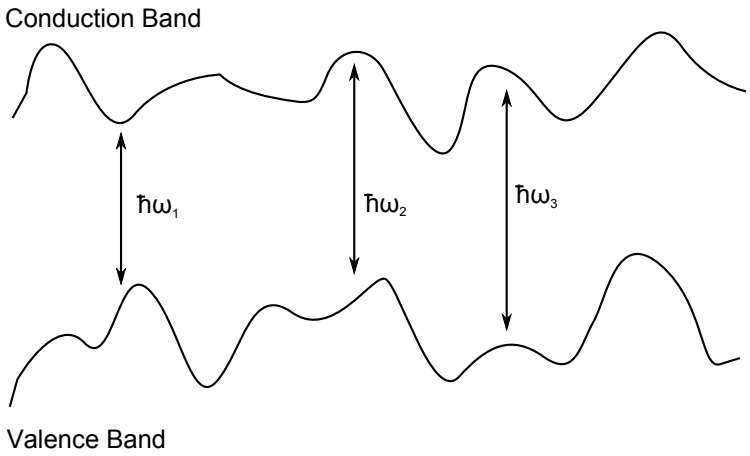

Figure 2.3: A diagram showing disorder in a bandgap created by localised strain on the relative position of atoms in a semiconductor. Arrowed lines in this case respond to radiative recombination of an electron-hole pair and it can be seen that different values of E_g will lead to a broadening of the spectra.

If confinement becomes great enough quantum effects can occur. In the case of quantum wells and 2D materials such as MoS_2, the electron is unrestricted in movement in two directions, and confined in the third. This modifies the density of states to a step like structure with each step corresponding to a confined energy state (25). In the case of quantum wires, such as GaAs NWs, electrons

are confined in 2 directions. We find that the linewidth of emission from the materials studied in this report are dominated by inhomogeneous broadening due to structural disorder in our nanostructures. Localised strain on the atoms in a crystal lattice effects their relative positions leading to a disordered band-edge as demonstrated in figure 2.3. Radiative recombination of electron-hole pairs (marked with arrows) will therefore have a slightly different energy at different positions in the crystal.

2.1.1 Continuous wave photoluminescence

In our studies we focus on low temperature PL spectroscopy. A sample is placed in vacuum on a cold finger in a He continuous flow cryostat as depicted in Figure 2.4b. Liquid He is pumped from a dewar into a series of copper tubes thermally connected to the cold finger, causing the sample temperature to drop to 10K. This system also allows temperature dependences to be measured.

Above band-gap excitation is achieved with the application of collimated laser focused by a series of lenses as depicted in Figure 2.4a. The laser is focused onto the sample using a microscope objective with a numerical aperture of 0.5 and working distance of 13.6mm, a spot size of around 1.5μm is typically achieved. These experiments can therefore be considered as micro-photoluminescence. In order to prevent any broadband emission of the laser affecting the results, a narrow pass filter is placed before the sample. A variable density filter can also be used to control the incident laser power.

PL emission from the sample is collected through a series of lenses which focus the signal on the entrance of the slit of a spectrometer. A long-pass filter placed

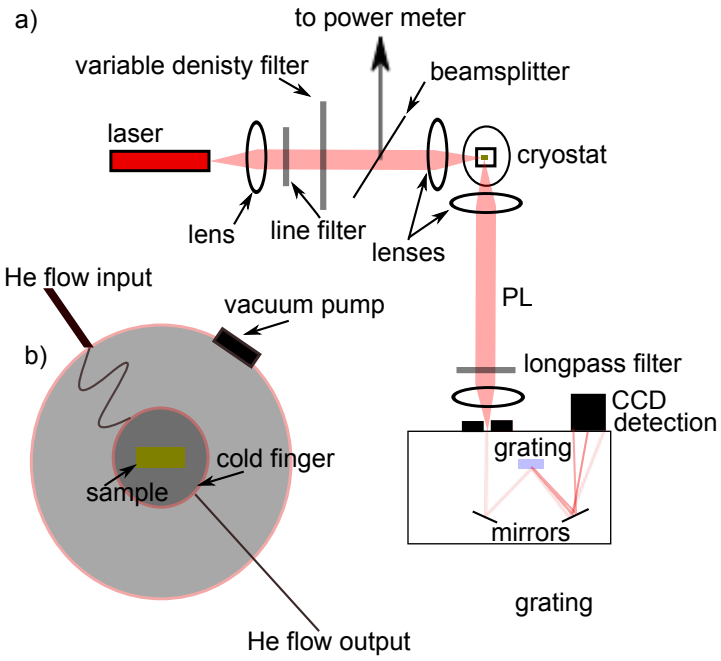

Figure 2.4: (a) A diagram showing the experimental setup for a standard PL experiment where a focused laser beam is directed at a sample in a cryostat and PL emission is collected using a spectrometer and CCD. Here a neutral density filter is used to control the incident power of the laser and this is measured using a power meter by splitting the beam. A line filter is used to remove broadband emission from the laser and a long-pass filter placed before the spectrometer stops reflected laser light hitting the CCD. (b) A diagram of continuous flow He cryostat. This is pumped so that the sample is in vacuum. A flow of liquid He passes through a series of copper pipes attached to a cold finger where the sample is attached. This allows temperatures of 10K to be achieved.

in this path removes any reflected light from the incident laser. A diffraction grating inside a spectrometer separates the incident PL by wavelength, which is collected on a liquid nitrogen cooled charged coupled device (CCD) chip.

2.1.2 Time resolved photoluminescence

Time resolved PL is used to measure the temporal characteristics of light emission as a result of sample excitation with a pulsed laser. Typically, the PL decays in the nanosecond range in structures where the electron-hole pairs are tightly bound (58). Instead of a continuous beam of photons, the sample is excited by very short laser pulses, which are 2ps in the case of this work. The PL spectrum is then recorded as a function of time from the arrival of the excitation pulse. Resolution of the detector plays an important role in these experiments. We use an avalanche photon detector (APD) in the case of samples with low photon emission (uncapped GaAs NWs) and this had a 8meV spectral range (as determined by the slit width) and temporal resolution of 350ps. For samples with a higher photon yield and shorter lifetimes (capped GaAs/GaAsP NWs) we used a streak camera that has an improved resolution of <5ps. This collects emission in a single channel and therefore has a much lower sensitivity so could not be used in the case of the uncapped GaAs sample.

2.2 Microscopy techniques used in this work

The optical properties of materials are heavily effected by their physical structure which can be studied using various microscopy techniques. In this thesis atomic force and ultrasonic force microscopy is used to image 2D sheets of MoS_2 and scanning electron and transmission electron microscopy is used to image nanowires.

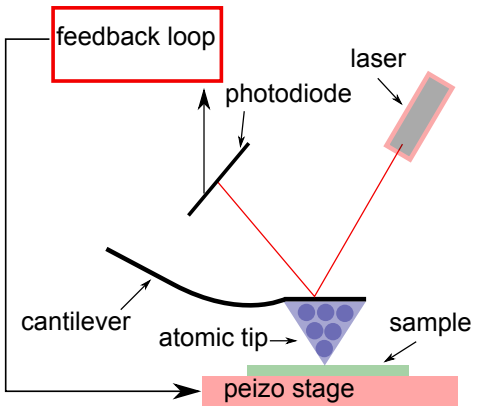

Figure 2.5: A diagram demonstrating basic AFM operation. A near atomic sharp tip attached to a cantilever is deflected by coulomb forces between it and a sample surface. This deflection is detected by a laser which is reflected off of the cantilever surface and a electronic feedback system repositions the sample using a piezo-system to maintain a constant height between the tip and surface. The vertical height of the peizo-system in z is recorded, as the sample moves in the directions x and y, and is converted into a 3D image of the sample height.

2.2.1 Atomic force microscopy

The atomic force microscope (AFM) was developed by Binning et. al. in 1986 (110), for which he received the Nobel Prize. This technique can be used to resolve down to the atomic level. Atomic force microscopy (AFM) uses a sharp tip with

a radius of nanometre magnitude, which is attached to a cantilever. When the tip is brought close to the sample surface, in the case of this work sheets of MoS_2, electrostatic forces act on the tip, which makes the cantilever bend according to Hookes law. This force is detected by deflection of a laser against the cantilever, into a photodiode detector. An electronic feedback detection system repositions a piezo stage where the sample is held, which moves the sample up and down keeping the tip at a constant height above the surface. This scheme is described in figure 2.5 and was used in this work to measure the thickness of MoS_2 samples. An example image of an MoS_2 sheet on a Si substrate is given in figure 2.6a.

2.2.2 Ultrasonic force microscopy

Ultrasonic force microscopy was developed by Yamanaka et. al. in 1994 (111). This adaptation of AFM can be used to measure stiffness of material (for example mechanical coupling to the substrate) on the nanometer scale (112). For this technique the sample is vibrated at small vibrational amplitude (0.5-2 nm) and high frequency (2-10 MHz), much higher than the resonance frequencies of the AFM cantilever. The restoring force of the sample is then modified by the stiffness of the material, and this can be used to detect below-surface features such as cavities, subsurface interfaces and sample-substrate interfaces. UFM can be measured concurrently with AFM, detected on a separate channel where ultrasonic vibration at the tip-sample junction is converted into an image by nonlinear rectification.

In this work UFM is used to detect nanometer scale resolution of stiffness of 2D structures of few atomic monolayer MoS_2. An example UFM image of MoS_2 is

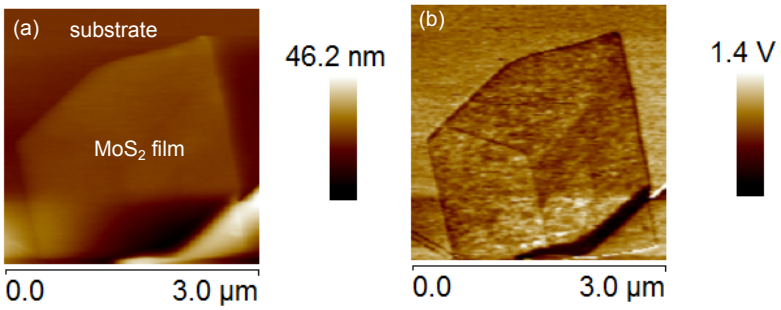

Figure 2.6: (a) An example of an AFM image showing a sheet of MoS_2 on a silicon substrate. The relative thickness of the MoS_2 can be calculated from this image. (b) A UFM image of a MoS_2 sheet on a Si substrate. The relative dark contrast compared with the substrate denotes that is relatively soft and therefore there is weak mechanical bonding between the two.

given in figure 2.6b. In this case bright (dark) colours correspond to higher(lower) sample stiffness. This is used to detect below surface defects, regions of suspension and measure mechanical coupling of 2D materials with the substrate. In particular, we use this technique to show weak mechanical bonding between the substrate and MoS_2 for free standing sheets and strong mechanical bonding when a dielectric capping layer is added. Measurements of graphene using UFM have been presented elsewhere (113).

2.2.3 Electron microscopy techniques

Diffraction limits the resolution of an optical microscope to around 1 μm. Electrons have a small de Broglie wavelength, and therefore higher spatial resolution can be achieved. There are two electron microscopy methods used in this thesis: scanning electron microscope (SEM) and transmission electron microscopy (TEM).

2.2.3.1 Scanning electron microscopy

A sample is prepared using conductive glue to bridge between the sample and sample holder, before being placed in a vacuum chamber. A focused beam of electrons is produced thermoionically in a tungsten cathode and raster scanned across the surface of the sample. Secondary electrons are emitted from the sample due to inelastic scattering within a few nanometers of the surface (114). As the angle of surface relative to the detector increases, the escape area of these secondary electrons decreases and therefore the intensity drops. Electrons are collected by a scintillator grid, which converts the intensity into an image. The resolution of SEM is <1nm (115). In this work SEM is used to measure the dimensions and density of GaAs NWs. An example SEM image is given in figure 2.7a.

2.2.3.2 Transmission electron microscope

Unlike SEM, where secondary electrons are emitted from the sample surface, electrons in TEM are transmitted through the entire sample; usually after the sample has been thinned to nm thickness. In experiments presented in this thesis, the energy of electrons was set to 200kV. The electrons interact with atoms during transmission and scattering can be used to produce an image (116). TEM has a higher resolution compared to SEM as electrons are transmitted through the crystal lattice, but requires samples to be extremely thin (<200nm) which is a disadvantage for many systems (115). In the case of the NWs sample studied here, the structure is already thin enough to be measured without any etching. In order to isolate NWs for TEM measurements, a sample of wafer is cleaved,

submerged in isopropanol and placed in a sonic bath for 1 minute. This causes NWs to disassociate from the surface, onto a copper metal grid used during the measurement process. An example TEM image for a GaAs/GaAsP NWs is given in figure 2.7b.

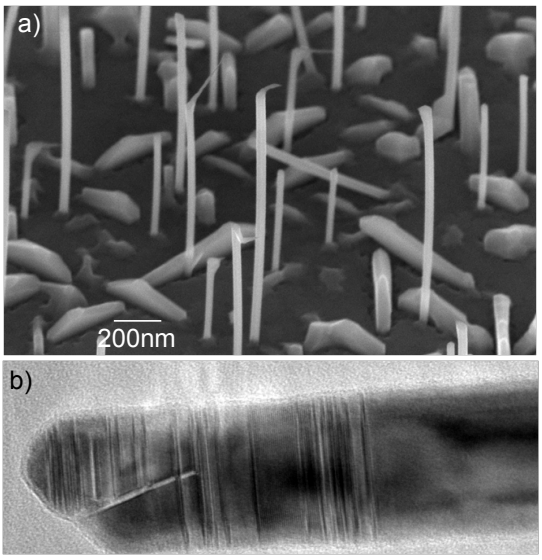

Figure 2.7: (a) An example of an SEM image of GaAs NWs on a Si surface which can be used to determine the density of NWs and their dimensions. (b) A TEM image of a GaAs/GaAsP NW showing defects in the NW which are stacking faults.

2.3 Conclusion and remarks

Here we presented a selection of high resolution spectral, spatial and temporal methods that were essential for this study. We performed CW-PL, TW-PL and SEM at the University of Sheffield, UK. We performed AFM an UFM in collaboration with O. Kolosov and B. J. Robinson at the University of Lancaster, UK. TEM measurements were performed for us by L. Otubo at the Instituto de Pesquisas Energticas e Nucleares IPEN, Sao Paulo, Brazil

Chapter 3

Effect of GaAsP Shell on the Optical Properties of Self-Catalyzed GaAs Nanowires Grown on Silicon

3.1 Introduction & Motivation

In section 1.2 we suggested that growth of nanowires (NW) may be the next step in the integration of optical active III-V semiconductor materials with cheaper Si electronics. In particular we highlighted addressing the specific need for cost effective and efficient photovoltaics (43, 44, 44, 45, 46). Here we discuss NWs grown on Si by a relatively new method which uses molecular beam epitaxy (MBE), a method that is particularly advantageous as it is catalyst free, produces a high crystalline quality and the density of crystal polytypes can be controlled

by varying the growth temperature (55, 56, 61).

III-V semiconductor NWs can be grown directly on Si as their narrow diameter allows radial variations which relieve strain between the different material structures without forming dislocations (22). By controlling the crystal phase (wurtzite (WZ) or zinc-blende (ZB)), or creating hetrostructure quantum dots by varying growth elements, electronic and optical properties can be controlled by confinement (60, 61, 62, 117). Optical absorption of the solar spectrum, and therefore efficiency of photovoltaic elements, can be maximised by accurately controlling the NW width (45).

There are various effects which lead to broad photoluminescence (PL) emission spectra in NWs which need to be considered in the case of our work. These include crystal defects (stacking faults), inhomogeneity of the NW radius (118, 119) and variations in strain within the capping layer in core-shell structures (58). Narrow line-widths can be achieved by creating a heterostructure where an optically active quantum dot (QD) is embedded in the NW length (36, 120, 121, 122). Embedding QDs in a NW has the particular advantage that the QD dimensions can be accurately controlled by both the NW diameter and the ability to create sharp interfaces during growth (123). QDs embedded in NWs has particular use in photonics, specifically in creating LEDs (22, 30, 31).

In our work we consider the effect of surface state recombination by comparing capped and uncapped structures for the first time in NWs grown with this method. Non-radiative exciton recombination on the surface of a semiconductor material (63) reduces optical efficiency and this is particularly dominant for NWs due to the large surface-to-volume ratio. The density of surface charge traps can be greatly reduced by addition of a capping layer after growth of the NW, creating

a core-shell structure (65). The addition of a capping layer is often found to enhance optical emission yield (67) and its suggested that this is because it reduces the density of non-radiative charge traps which exist on the NW surface (65). Typical core-shell structures include catalyst free MBE grown GaAs/AlGaAs NWs (65), catalyst free metal organic vapour phase epitaxy (MOVPE) grown GaAs/GaP NWs (66) and gold catalyst seeded MBE grown GaAs/GaAsP NWs (67).

3.1.1 Our work

Despite reports on their high crystal quality, few reports exist on the optical properties of catalyst free MBE grown GaAs NW structures on Si, an issue we address in this chapter. In particular we show the first ever measurements of GaAs/GaAsP core-shell structures grown by this method. Growing NWs on Si significantly reduces substrate costs and this catalyst free method avoids Au contamination which may effect the efficiency of electron transport in photovoltaic elements. In this work we consider photoluminescence (PL) from single NWs to avoid the issue of inhomogeneities present in assembles, which allows clear information on their properties to be gained. Optical measurements of single self-catalysed NWs on Si are important for in-depth understanding and design of electronic properties.

In particular we demonstrate that an improvement of optical properties of these NWs can be achieved by addition of an MBE grown capping shell of GaAsP. This leads to a dramatic increase in PL yeild of up to 2000x. So far no reports have been published on MBE passivation of catalyst free NWs with GaAsP and

this may prove superior to materials such as AlGaAs (124) which are more prone to oxidation and non-radiative surface states (66). By investigating thermal activation we are able to determine the main carrier escape mechanisms that lead to PL quenching in the uncapped GaAs NWs. We show that a GaAsP capping layer reduces the efficiency of comparable thermally activated non-radiative processes in uncapped samples by 8 times. For this reason we find that GaAs NWs are quenched at 60K but GaAs/GaAsP samples emit up to room temperature. We link this quenching process to non-radiative recombination on the NW surface and show that GaAs PL yield degrades significantly over time due to oxidation of the surface. We find a second high energy PL quenching process for the GaAs/GaAsP sample which we relate to electrons escaping from the GaAs core into the GaAsP shell.

Considering TEM measurements we find that our GaAs/GaAsP core-shell NWs have a high crystal quality which is dominated by the GaAs zinc-blende phase. By linking the crystal structure to observations of PL, we find type-II quantum confinement in the case of our uncapped GaAs NWs which were grown at a lower temperature. In this case electrons and holes are spatially separated in different crystal phase poltypes. We show that holes are confined in wurtzite segments and electrons in zinc-blende segments. We also suggest that the band-gap of emission can be strain-tuned in our NWs by alternating the nominal concentration of P in a GaAsP capping shell.

We therefore demonstrate that GaAs NWs grown on Si using the catalyst free MBE technique are a high quality material with robust optical properties for potential use in highly efficient photovoltaic elements. We show that the optical and electronic properties can be effected by selective control of structural

properties during growth.

3.2 Growth of nanowires and sample details

In this work two different nanowire (NW) samples were grown catalyst free on Si(111) wafers using molecular beam epitaxy (MBE) (58). MBE is a growth mechanism used in semiconductor manufacturing which is performed at a slow rate (<3000nm per hour) in order to grow layers epitaxially with low defects (125, 126). A simplified diagram to illustrate this process is given in figure 3.1. A target substrate is firstly placed in a ultra high vacuum (UHV) chamber, which is pumped to a pressure of typically 10^{-10}mbar. Effusion cells, containing the elements to be deposited, are heated causing evaporation and a shutter on each cell allows a beam of these atoms to be directed onto the substrate. Due to the slow deposition rate atoms combine on the substrate and grow epitaxially atomic layer by atomic layer. As the shutter speed is much faster than the deposition rate, very thin layers with sharp interfaces can be produced

A description of catalyst free MBE NW growth is given in section 1.2.2. In our case a high temperatures of 1000^{o}C was initially used to remove SiO_2 in situ before deposition. For the first NW sample Ga and As were combined to produce a large number of randomly positioned self catalysed GaAs nanowires on a silicon substrate, with a substrate temperature of 635^{o}C. The second sample was produced in the same way, but at a higher temperature (640^{o}C). After NW growth in the second sample the substrate was cooled to 500^{o}C and coated with a layer having nominal composition of $GaAs_{0.85}P_{0.15}$. This produced a core-shell GaAs/GaAsP nanowire structure. From here in the thesis the uncapped GaAs sample will be called sample 1 and the core-shell GaAs/GaAsP sample 2.

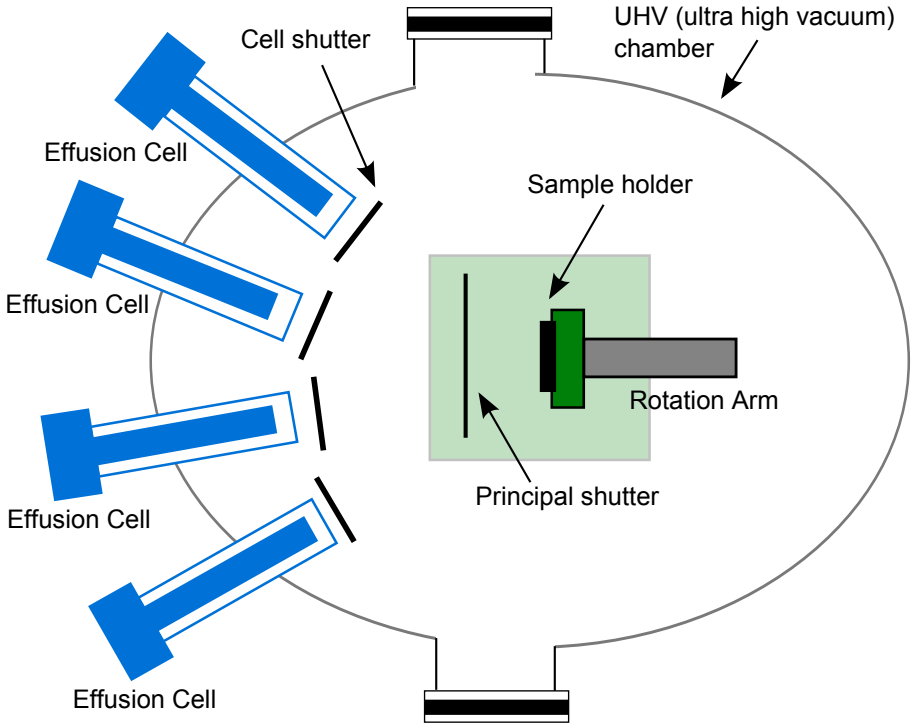

Figure 3.1: Simplified diagram showing an MBE chamber. The sample is placed in an ultra high vacuum chamber, typically 10^{-10}mbar. Effusion cells are heated to vaporise constituent elements which are directed onto the sample. A slow rate of deposition allows sharp interfaces to be achieved by using the cell shutters.

3.3 Microscopy characterization

In this section measurements using Scanning Electron Microscopy (SEM) and Transition Electron Microscopy (TEM) are presented to describe the structural properties of the NW samples. We therefore demonstrate that we have high quality crystalline samples, similar in quality to those previously reported (55, 56). In order to isolate NWs for TEM measurements, a sample of wafer is cleaved, submerged in isopropanol and placed in a sonic bath for 1 minute. This causes NWs to disassociate from the surface, onto a copper metal grid used during the measurement process. TEM measurements were not performed for the uncapped Sample 1 as it was found that when trying to remove NWs they collapsed and stuck strongly to the substrate. A complex structure of WZ/ZB phase defects can be detected in PL measurements presented in this chapter.

3.3.1 GaAs NWs (Sample 1)

An SEM image of GaAs NWs is given in figure 3.2. It is found that by varying the position across the growth wafer from the centre to the edge, the density of NWs decreased outwards. The density at the centre of the sample is $\sim$ 10NW/μm^2 and the edge <0.5NW/μm^2. The SEM image provided is from a relatively high density part of the sample. It can be seen that NWs are well isolated and vertically standing on the surface. These NWs are between 1-3 μm in height and 30-80 nm in width. In order to carry out μ-PL measurements a position on the sample is chosen with a low enough density to successfully isolate a single NW.

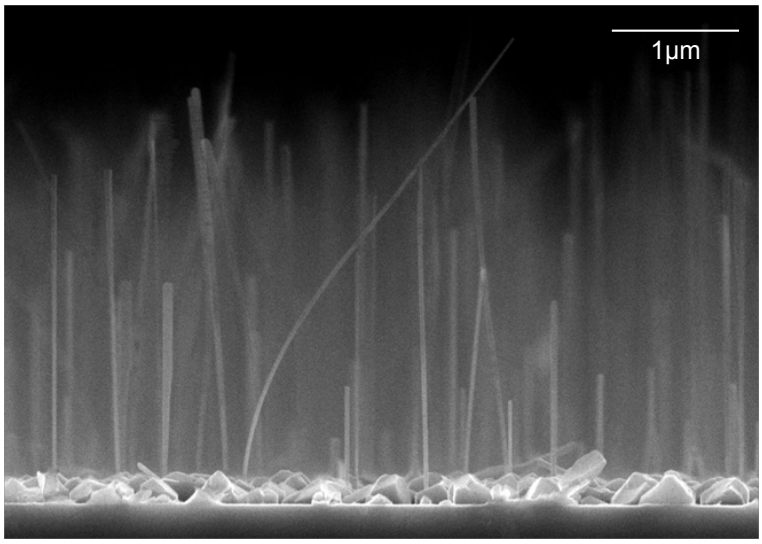

Figure 3.2: An SEM image of uncapped GaAs NWs (sample 1) grown by catalyst free MBE on a silicon substrate. It can be seen that NWs are between 1-3 μm in height with a 30-80 nm diameter

3.3.2 GaAs/GaAsP NWs (Sample2)

An SEM image of the GaAS/GaAsP sample is provided in figure 3.3a. NWs are again found to be well isolated and decreasing in density from centre to wafer edge, although the higher density section of the wafer is of a lower density than the previous sample ($\sim$1.5 μm^2). The height of NWs on this sample is again found to be between 1-3 μm. The diameters are found to be greater than the previous sample (between 50-120 nm), which is expected due to the additional capping layer. To measure the crystal structure and nominal thickness of the GaAsP layer we carried out TEM measurements.

TEM images of these GaAs/GaAsP NWs were possible to measure as we were able to remove NWs from the substrate in this sample. Using image contrast in figure 3.3b it is possible to measure the width of the GaAs core to be 30nm (upto

70nm in other samples), similar to the width of the uncapped NWs. The diameter of the NW is shown to be very uniform along its length. The nominal thickness of GaAsP layer is found to be 10nm.

As described in section 1.2.3 both wurtzite (WZ) and zinc-blend (ZB) polytype lattice structures are possible in NWs. An electron diffraction spot pattern for the GaAs/GaAsP NWs is given in figure 3.3d. This was collected in addition to TEM by detecting Bragg scattered electrons, which were detected in the back-focal plane (rather than the standard focal plane used for imaging). This exploits diffraction effects of electrons and each diffraction spot denotes a plane of atoms within the atomic crystal. In order to analyse this image detailed fast Fourier transform analysis were carried out for us which utilised the interpretation of Sarney *et. al* (127). This diffraction measurement confirms that these NWs are ZB in structure. We found that all NWs in this sample were in fact ZB.

Defects at the tip of the GaAs/GaAsP NWs can be seen in figure 3.3c. It is possible to identify some of these as twinning of the ZB crystal plane (128). This is shown in more detail in figure 3.4b and this occurs due to stacking faults. The stacking order of ZB is ABCABC and these stacking faults occur in the form of a ABCACBA sequence (22). In rarer cases a NW where a wurtzite (WZ) stacked GaAs region interjects between ZB stacked layers was found (60) as demonstrated in figure 3.4a. This defect was only observed in a small number of NWs. All defects found were small and isolated in the NWs tip, therefore the GaAs/GaAsP NWs presented in this report can be considered as high quality ZB structures.

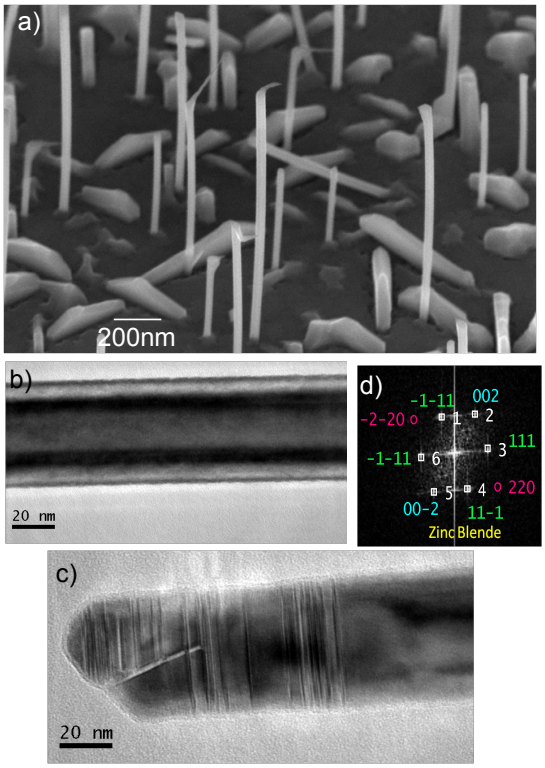

Figure 3.3: (a)An SEM image of capped GaAs/GaAsP NWs grown by catalyst free MBE on a Si substrate. The height of NWs on this sample can be seen to be between 1-3 μm and diameters between 50-120 nm. (b) A TEM image of a GaAs/GaAsP NW. The image contrast between the NW and capping layer is clearly visible and it is possible to measure the capping layer at 10nm and the core at 30nm (d) An electron diffraction pattern showing that this NW is ZB in structure. (c) A TEM image demonstrating defects in the tip of the NW as discussed in the text.

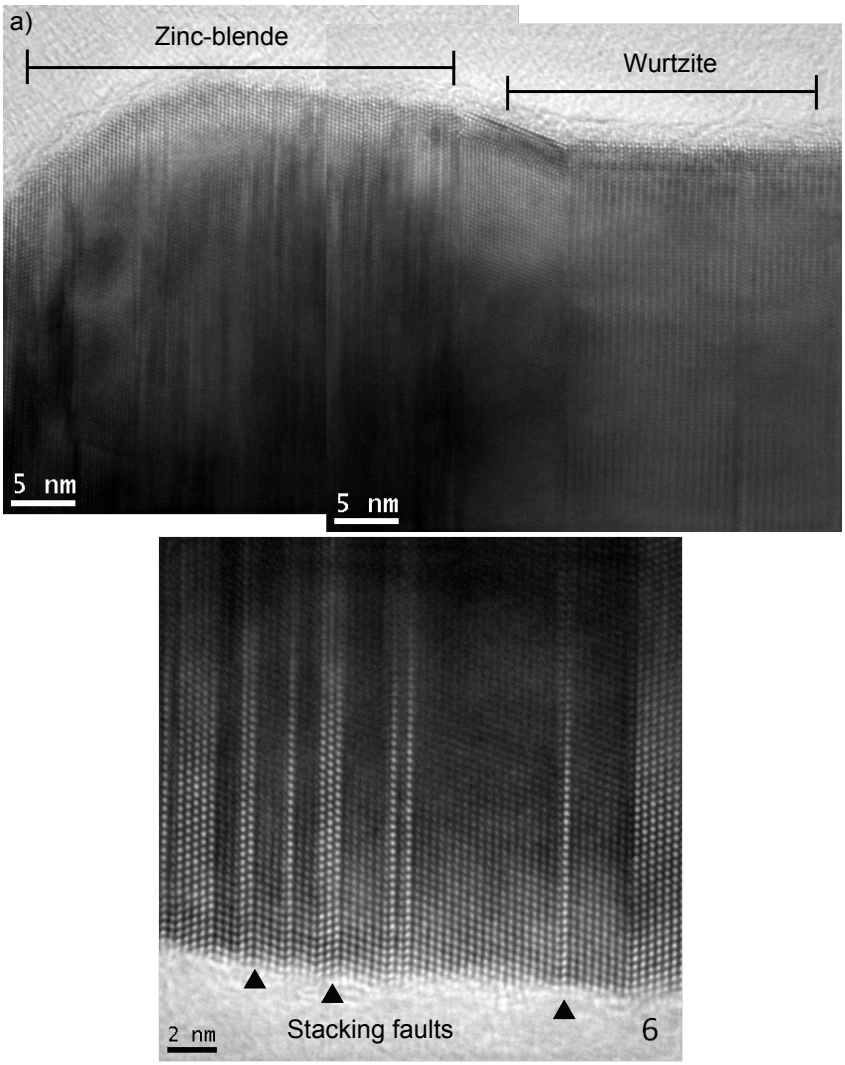

Figure 3.4: (a) A TEM image showing the rare case where a section of WZ stacked GaAs crystal interjects into the NW at the tip forming WZ/ZB stacking sections. (b) A TEM image showing defects due to stacking sequence faults in the ZB cyrstal at the tip of a GaAs/GaAsP NW as described in the text.

3.4 Optical PL measurements

Continuous wave (cw) optical measurements of NWs are carried out with a 1.893 eV diode laser focused on the sample with a 1.5μm sized region. The sample was placed in a vacuum cryostat with variable temperature. PL measurements were collected from above the NWs with a spot size of 1.5μm . A single spectrometer was used for all measurements as high resolution was not required.

Further to CW-PL measurements, time resolved PL spectra are also collected. For the uncapped GaAs NWs the data was collected using an avalanche photodiode (APD) with a resolution of 350ps and data for the GaAs/GaAsP NWs collected using a streak camera with a resolution of 5ps. For these measurements excitation was achieved using a Ti-sapphire laser producing a series of 2ps pulses. The laser excitation for uncapped samples was 1.595eV and for GaAs/GaAsP samples 1.71eV. All measurements were performed at 10K temperatures.

3.4.1 GaAs NWs (Sample 1)

3.4.1.1 Continuous wave PL measurements

A selection of PL spectra for the uncapped GaAs NW sample is presented in figure 3.5. These spectra are collected with an excitation power of 100μW and a collection time of 10s. It can be seen that emission from this sample has a relatively narrow linewidth (between 5-20meV) and a very large emission range of 100meV, with emission visible below the band-gap of GaAs (1.52eV (59)). By moving the laser focus on a single NW different positions along the length could be excited. It was found that, for different positions along the NW length, emission was detected at different energies. Multiple NWs were considered to

achieve the total range in figure 3.5

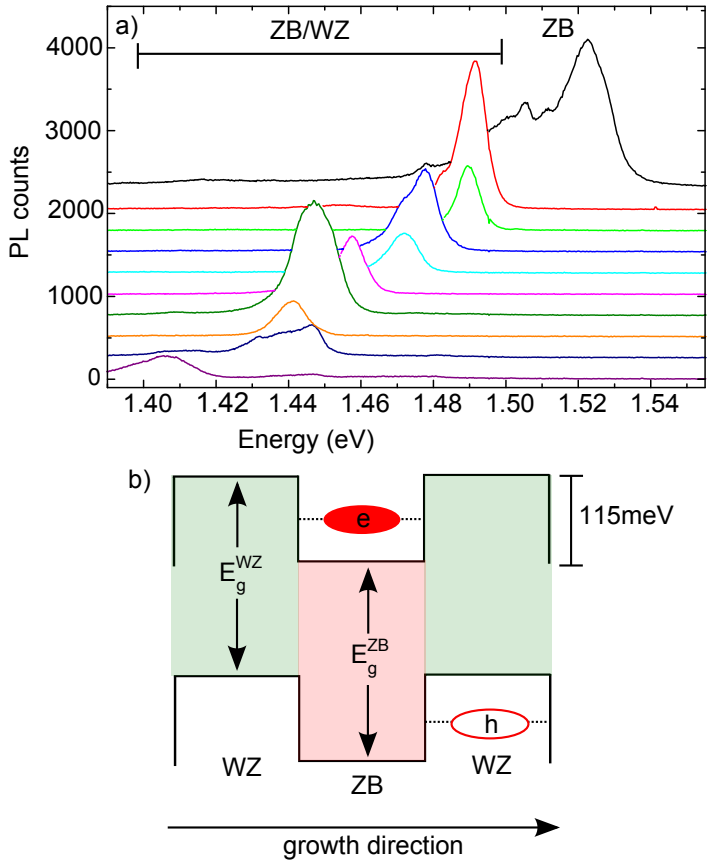

Figure 3.5: (a)A PL spectrum of various GaAs NWs measured at $100\mu W$ with a collection time of 10s. This demonstrates PL emission for the whole range detected, with both type II (emission confined between ZB and WZ layers) and type I emission (from ZB) sections labelled. (b) A diagram demonstrating quantum confinement of electrons and holes in the NW growth direction which leads to type II spatial confinement.

In order to explain below the band-gap emission energies, the structure of the NW must be taken into account. The bandgap of ZB is E_g^{ZB}=1.515 (59) and the bandgap of WZ has been measured between E_g^{WZ}=1.5 - 1.58eV (129). The fact that emission is found below this, up to ∼1.405eV, suggests an effect of crystal phase electron confinement between the two crystal types. This has previously

been observed in III-V NWs grown by different methods (61, 62, 64, 117, 128). In this case holes are expected to be confined in the maxima of the valence band of WZ segments and electrons confined in the conduction band of the ZB segments. This special case of confinement, described as type II, is presented diagrammatically in figure 3.5b.

The lowest emission measured, 1.405eV, reflects a valence band offset between ZB and WZ structures of 115meV; which agrees well with previously calculated results (47, 60). This is expected to arise from e-h recombination, as demonstrated in figure 3.5b, at the boundary between large ZB and WZ segments and has the largest confinement. The wide range of emission energies observed in our studies arises from variation of the thicknesses of the WZ and ZB segments, leading to variation of the carrier confinement. As the confinement becomes weaker emission energy increases. Emission at 1.514eV, the highest energy measured, is expected to be type I emission from single phase WZ GaAs.

3.4.1.2 Time-resolved PL measurements

This conclusion is further supported by time resolved PL measurements performed on different GaAs NWs emitting across the whole range of emission energies, and at different points along a NW spectrum. In Figure 3.6a a PL spectra for a single NW which is expected to have type II confinement is presented. In figure 3.6b decay curves of relative emission intensity with time, collected using an APD, are presented for the different positions marked on the above diagram. To find the decay constant τ, the decay of emission energy was fit to a single exponential function in equation 3.1.

$$I = I_0 e^{-\frac{t}{\tau}} \tag{3.1}$$

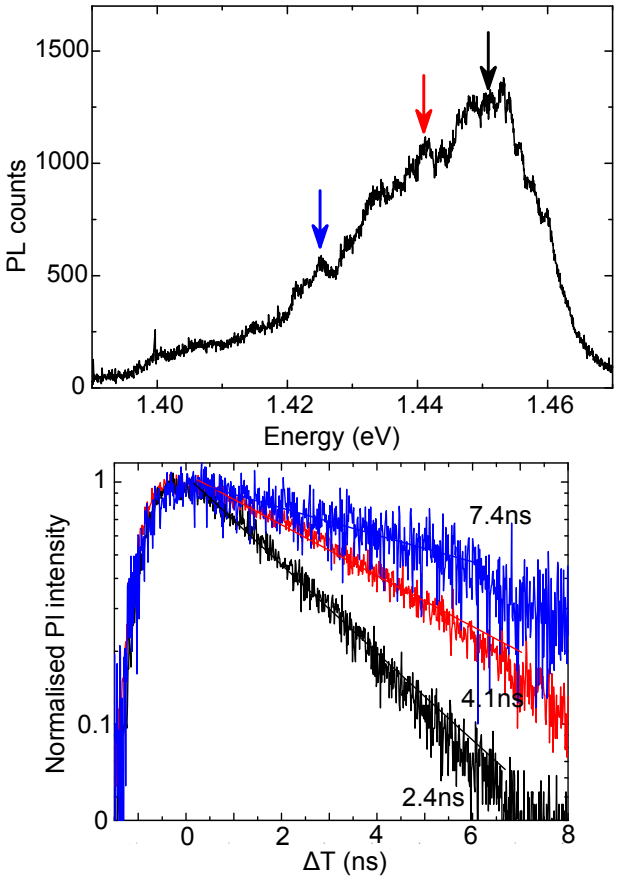

Figure 3.6: (a) A PL spectrum of the single GaAs NW emitting below the bandgap of ZB GaAs. The position in energy considered for time resolved analysis is marked with arrows. (b) Time response measured using a APD at $P_{ex} = 20$ W for a single NW in the positions indicated by arrows in the spectrum in part (a).

A value of τ=7.4 ns is measured for NWs emitting at lower energies of 1.425eV. This long lifetime is characteristic of indirect exciton recombination (type II) due to the relatively large spacial separation between electrons and holes localised in regions with different crystal phases. A shortening of the lifetime for emission

is observed when we compare NWs emitting at higher energies. This shortening of the lifetime (with increasing energy) reflects stronger overlap between electron and hole. This is due to the carrier confinement becoming weaker as the size of relative WZ segments are reduced. For the highest emission energy detected (1.52ev) the lifetime is only 0.3ns (the resolution of the experiment) and this corresponds to type-I alignment (emission of a pure ZB phase) (130). Additional lifetime shortening (as observed directly in the figure 3.8) may be related to contribution of carrier escape to faster non-radiative surface states.

3.4.2 GaAs/GaAsP NWs (sample 2)

3.4.2.1 Continuous wave PL measurements

Figure 3.7 shows emission spectra from individual core-shell GaAs/GaAsP NWs. This was collected with an excitation power of 100 nW and collection time of 5s. Unlike uncapped GaAs NWs, there is no local variation in the observed peak position. The lack of variation can be compared with observations of crystal structure detailed in section 3.3. Using TEM we found that the crystal structure of the NW is purely ZB, with few defects, and therefore type II confinement can not occur. The emission is therefore from direct (type I) recombination of the bandgap of ZB GaAs, as depicted in figure 3.7b. Type-II confinement is also not observed between the NW core and shell. This is because the excitons are largely confined in the NW core as is described in the next section.

The emission energy of these samples, 1.57eV, is much higher than the ZB band-gap of 1.52eV. This blue shift is the result of strain imparted on the NWs by the capping layer due to lattice mismatch. In this case the band-gap is changed

by pushing atoms closer together. The addition of 15% P concentration in GaAsP (as used in these samples) has been predicted in other work (69) to lead to a blue shift of 50meV, which is consistent with our work.

Due to the process of MBE deposition, there is expected to be a small variation in thickness of capping layer and concentration of P over the sample. While this effect is reduced by rotating the sample during growth, a small variation is still expected which explains a slight variation in emission energy over the sample surface. The linewidth of emission is 50meV, much larger than the previous sample. This will be considered in the next section.

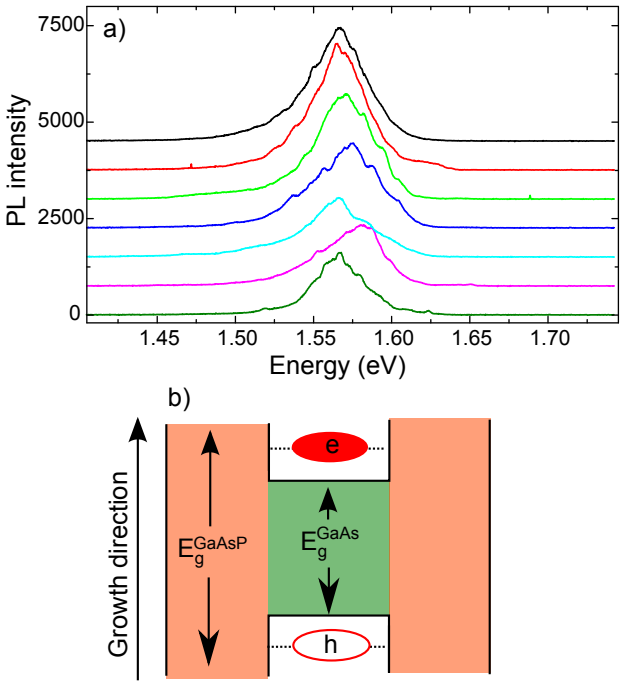

Figure 3.7: (a) PL spectrum of various GaAsP/GaAs NWs which show only a small variation in the emission energy and a linewidth of 50meV. (b) A diagram demonstrating type I confinement where an exciton recombines down the NW length.

3.4.2.2 Time-resolved PL measurements

Figure 3.8 demonstrates a PL spectrum (insert) and decay curve collected using a streak camera (a) for a single core-shell GaAs/GaAsP NW. Carrier lifetimes in this case are measured to be around 1.43ns, which is similar to lifetimes of type-I self assembled quantum dots where the excitons are typically localised on the length scales smaller than the Bohr radii in bulk material (4, 58). This implies that the PL signal detected originates from excitons which are tightly bound within the NW.

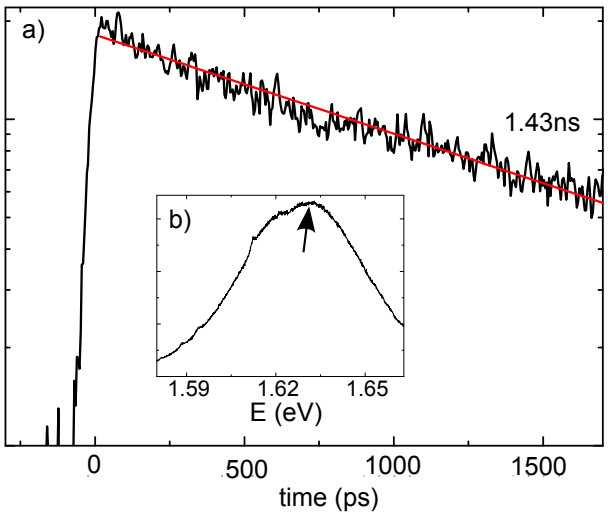

Figure 3.8: PL time evolution for a single GaAs/GaAsP NW evaluated at the energy of 1.6295 eV (solid line corresponds to exponential decay fit). The inset shows the PL intensity accumulated over a time window of 1.7 ns after pulsed laser excitation at time 0.

3.4.3 Comparison of emission spectra GaAs and GaAs/GaAsP NWs

An illustrative comparison of optical properties of GaAs and GaAs/GaAsP NWs is given in figure 3.9. The line-width of the PL emission from GaAs/GaAsP is found to be between 20 and 50meV - much larger than the emission of uncapped GaAs NWs which was between 5-20meV. Despite this, even the largest linewidth is still much smaller than the overall spread of PL peaks in the uncapped sample, which is 100meV due to type II confinement. The larger linewidth for individual peaks of GaAs/GaAsP NWs is likely related to the radial confinement potential variations which appear due to strain inhomogeneities in the capping layer.

An impressive increase in emission yield when comparing with the GaAs and GaAs/GaAsP samples can be seen in figure 3.9. The enhancement is on average ∼2000x, with increases up to 20000x being observed when comparing the weakest emission of uncapped NWs and the brightest emission of GaAs/GaAsP NWs. This is a much higher increase than in previously measured core-shell NW systems (54, 67).

This enhancement of PL emission can be related to the passivation of the outer layer by the addition of GaAsP capping. NWs naturally have a large surface to volume ratio, and therefore surface states play an import role in determining emission properties as they can act as paths for non-radiative recombination. The intensity of PL is therefore partially determined by competition between these surface states and radiative emission.

Work on temperature dependence presented below demonstrates that in capped structures the electrons are strongly confined within the core and therefore will

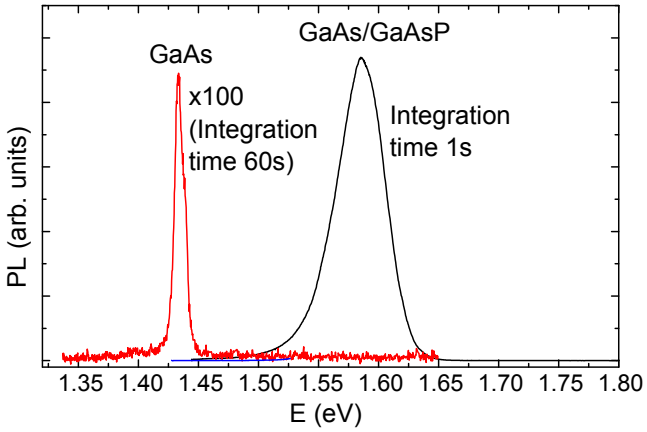

Figure 3.9: Comparison of emission intensity and linewidth between uncapped GaAs structures on sample 1 and GaAs/GaAsP core-shell NWs on sample 2. It can be seen that the GaAs/GaAsP core-shell structure has an enhanced PL yield as well as a much broader linewidth - 50meV compared to 10meV.

be isolated from the surface. This is further confirmed as we do not observe PL corresponding the the GaAsP shell. An increased isolation of electrons from the surface due to increased confinement is therefore likely to be the dominant effect in reducing the effect of surface states and enhancing emission yield for capped structures. Additionally, the capping layer may also act to suppress charge traps at the surface (54, 65, 67). This is the first time that PL enhancement has been measured for GaAsP capping on NWs grown by catalyst free MBE. GaAsP in this case was chosen as it is less prone to oxidation (124) than AlGaAs (64, 65).

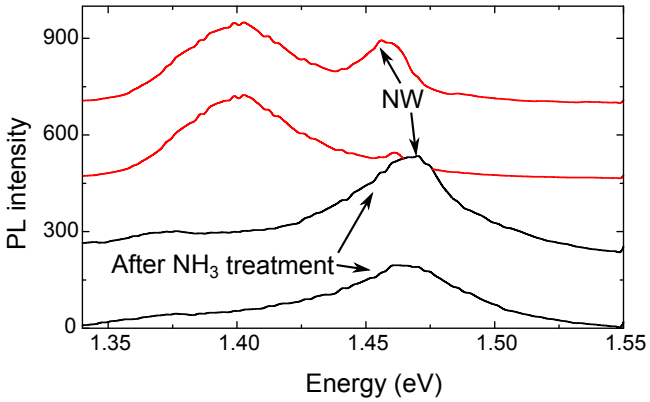

Figure 3.10: PL spectra demonstrating a uncapped GaAs NW (sample 1) which has been allowed to oxidise naturally over time (in red). It can be seen that additionally to NW emission at 1.47 a broader lower energy shoulder has appeared which we attribute to oxygen impurities. We also demonstrate (in black) that the PL yield of NWs can be enhanced, and simultaneous the low energy peak removed, by washing the sample in NH_3.

3.4.4 The effect of oxidization on surface states of uncapped GaAs NWs

Further confirmation of the effect of surface states in uncapped NWs is provided by measuring how the PL intensity of this sample degrades over time. The addition of a capping layer acts to protect the NWs from interactions with their environment. For an uncapped sample which was stored in air, a reduction of PL intensity is found to be dramatic over a time scale of weeks and simultaneously to this a second and much broader (70-130meV) peak appears at 1.4 eV (figure 3.10). As NWs have a large surface to volume ratio, oxidation of the outer layers will effect its properties and oxidation has previously been observed on the surface of bulk GaAs (131). We therefore ascribe this low energy peak to oxygen impurities and this oxidation process creates additional surface traps.

The oxidation process is found to increase in speed when the sample is thermo-cycled during measurements and can occur on a timescale of hours. Conversely core-shell GaAs/GaAsP NWs do not degrade noticeably over time.

Surprisingly it was found that this degradation process can be reversed by washing the sample in ammonia (NH_3) dissolved in water and we must assume the acid dissolves and washes away these impurities from the NW surface. The result of this is given in figure 3.10 and it can be seen that by removing oxide surface states the NW emission becomes brighter. Both these observations highlight the detrimental effect surface states play on the intensity of PL and support the suggestion that enhancement of PL by capping is due to the suppression of (non-radiative) surface states.

3.5 PL power dependence of GaAs and GaAs/GaAsP NWs

In order to see how the optical properties of the NW samples changes with incident photon intensity, PL power dependence was studied. Figure 3.11a shows PL spectra measured at a series of incident power (P_{ex}) between 5μW and 200μW for uncapped GaAs NWs. At very low values of P_{ex}, only two peaks (labelled E_1 and E_2) are detected at 1.4625 and 1.4677 eV respectively. As P_{ex} increases the intensity of E_2 becomes higher than E_1 which quickly saturates with increasing power. At the same time, new peaks (E_3 and E_4) appear on the higher energy side of E_2, eventually becoming brighter than the latter with further increases in P_{ex}. All 4 peaks blue shift with power as a consequence of band bending effects at the type-II WZ/ZB interface (67).

The power dependence shown in figure 3.11a is, therefore, a clear signature of the state filling effect on a single GaAs NW. By fitting the spectra collected at 50μW with 3 Lorentzian curves, the splittings between adjacent states are ΔE_{21}=E_2-E_1=5.2 meV and ΔE_{32}=4.5 meV. This is related to the localisation length of electrons. For example we can use the energy level solution for an infinite square well potential (25):

$$E_n = \frac{n^2 h^2}{8\mu L^2} \tag{3.2}$$

Where E is energy, h planks constant, μ the effective mass, L the confinement length and n=1,2,3,4. We use the simplification that the nanowire length is infinite and the effective mass for GaAs used is 0.067m_e (26). Considering a value

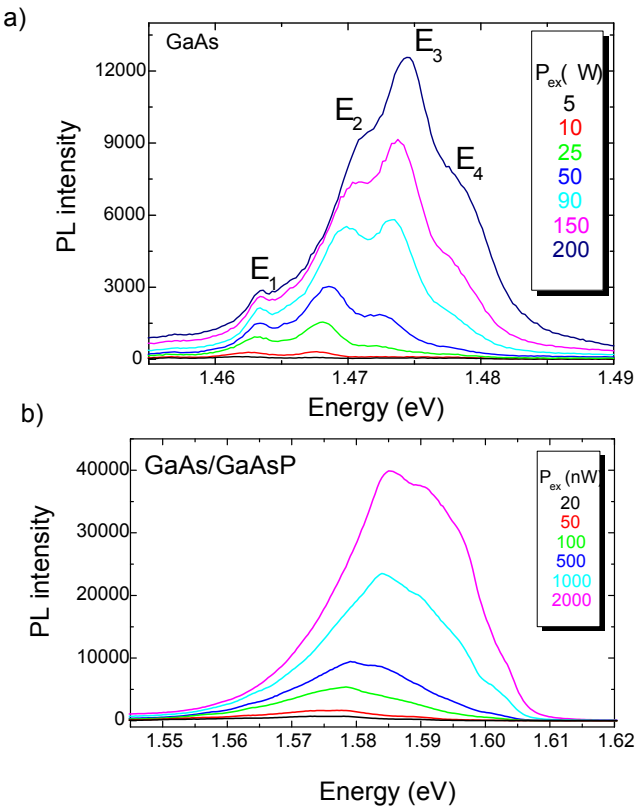

Figure 3.11: (a) Emission uncapped GaAs NWs (sample 1) with varied incident power. It can be seen that with increasing energy, additional states are filled which have been labelled E_1-E_4 (b) Emission from capped GaAs/GaAsP NWs (sample 2) with varied incident power. State filling can be similarly observed but the linewidth of individual states are much larger.

of E_{21}=5.2meV we calculate a confinement length of 57nm. This is consistent with the NW radius measured in SEM and we therefore attribute the splitting of the emission band into 4 well-defined peaks to radial confinement associated with the NW width.

Figure 3.11b shows a power dependence from a single GaAs/GaAsP NW. As for uncapped NWs, we observe the state filling effect. In this case the spectra is much broader and individual states are approximately twice larger than what

we have presented in figure 3.11a for an uncapped NW. This broadening is again likely to be related to inhomogeneity in strain related to the GaAsP capping layer.

3.6 PL temperature dependence of GaAs and GaAs/GaAsP NWs

In the above work it was observed that the addition of a GaAsP capping layer to the GaAs NWs leads to a large enhancement of the PL yield. As discussed, similar results have been published for different NWs and capping materials and it is often explained that the capping layer acts to suppress non-radiative recombination paths at the NW surface. In order to understand in more detail the effect of PL quenching mechanisms comparing capped and uncapped NW samples, a series of detailed temperature dependent measurements are collected. These were performed between 10K and room temperature (300K).

A comparison of relative PL intensity as a function of temperature for both GaAs/GaAsP NWs and GaAs NWs is given in figure 3.12. The intensity of GaAs NWs is found to drop quickly with temperature, where as GaAs/GaAsP NWs are still visible at room temperature. These results are modelled using the dual activation equation (132) for capped GaAs/GaAsP NWs:

$$\frac{I_{PL}(T)}{I_0} = \frac{1}{1 + A_1 \exp(-E_1/K_B T) + A_2 \exp(-E_2/K_B T)} \tag{3.3}$$

and a single activation for uncapped GaAs NWs:

$$\frac{I_{PL}(T)}{I_{02}} = \frac{1}{1 + A_{12}\exp(-E_{12}/K_B T)} \tag{3.4}$$

Where I_{01} and I_{02} are the normalization constants, E_1 (E_{12}) and E_2 are the activation energies of PL quenching processes as describe below, A_1 (A_{12}) and A_2 characterize the efficiencies of non-radiative processes (as related to E_1 (E_{12}) and E_2) and K_B is the Boltzmann constant. A simplified equation for uncapped GaAs NWs was chosen due to the limited temperature range of emission.

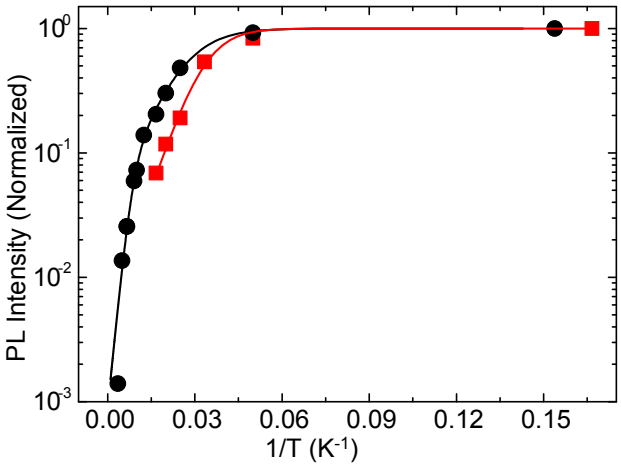

Figure 3.12: Temperature dependence of normalized PL for GaAs (squares) and GaAs/GaAsP (circles) single NWs. Lines represent fit to data as explained in the text.

Values of extracted parameters are given in table 3.1. The process E_1 (E_{12}) is likely associated with the activation of non-radiative recombination centres at the GaAs surface. While activation energy E_1 (E_{12}) is similar for both GaAs and GaAs/GaAsP NWs, the value of A_{12} is approximately 8 times smaller for the passivated GaAs/GaAsP NWs than A_1 for the uncapped GaAs NWs; showing that the efficiency of this process is reduced by capping. We therefore suggest

that the enhanced PL in the case of core-shell structures is due to a favourable change in the balance of efficiencies between radiative and non-radiative processes. This is most likely a consequence of stronger confinement of electrons in the core of GaAs due to the GaAsP shell compared to GaAs with an open surface (65, 66, 67, 67). We can estimate this strong confinement in core shell structures by considering the PL quenching mechanism E_2 below.

In the case of the capped GaAs/GaAsP NWs PL is observed up to room temperature. The intensity of PL emission for these capped structures is in fact brighter at 300K than the uncapped GaAs NWs at 6k. A second PL quenching mechanism, where E_2=48meV, is seen in this sample and found to have a large efficiency at high temperature. It is possible to associate this process with carrier escape from the GaAs NW core to the GaAsP barrier. This occurs when electrons confined in the core are thermally activated and able to escape over the energy barrier. The conduction and valence band confinement potentials for the GaAs/$GaAs_{0.85}P_{0.15}$ structure can be estimated using the calculations by Montazeri *et al* (69) in order to verify this.

These calculations were carried out for a core-shell system of GaAs/GaAsP. To estimate the barrier offset we assume a linear decrease in the barrier height as the P concentration decreases to 15%. Doing this we can estimate the conduction band and valence band offset as E_{CB} ≈75 meV and E_{VB} ≈45 meV. These are therefore roughly the escape barriers for electrons and holes respectively. Although this is a rather crude estimation, it allows us to attribute the value of E_2 to the escape of holes from the core to the shell of the GaAs/GaAsP NWs.

Table 3.1: Table 1: Thermal activation energies (E_1 and E_2) and efficiency of these processes (A_1 and A_2) obtained from the fittings in Figure 3.12 for single NWs from sample 1 and 2.

NW	$E_1(E_{12})$meV	$A_1(A_{12})$	E_2(meV)	A_2
GaAsP/GaAs	11±1	26.4	48±4	1107.1
GaAs	14±3	203.4	–	–

3.6.1 Summary of results

In this chapter structural and optical properties of core-shell GaAs/GaAsP and uncapped GaAs nanowires grown on Si substrates, using a catalyst-free MBE technique, are studied in detail. We find that while our uncapped GaAs NWs have a relatively small PL yield which is quenched with increasing temperature, the core-shell GaAs/GaAsP NWs have a PL yield exceeding 2000x the uncapped NWs and also emit brightly up to room temperature. We attribute this enhancement to the effect of the NW surface, specifically the competition between optical recombination in the NW length and non-radiative surface states. We suggest that the capping layer reduces the efficiency of non-radiative surface paths and we show that the thermalisation efficiency for non-radiative paths is approximately 8 times less in the GaAs/GaAsP sample. We find that additional surface states, further quenching PL, form on uncapped NWs which are exposed to air and we attribute these to oxidation of the surface. This process can be reversed by washing the samples in NH_3.

We demonstrate a second PL quenching mechanism at high temperature in capped NWs which we attribute to electrons escaping from the GaAs core into the GaAsP shell. The addition of GaAsP is shown to result in strain imparted on the core NW, which is evident due to a blue shift of PL above the band gap of zinc blende GaAs as well as a relatively broad distribution due to inhomogeneous strain. The ability to tune the absorption energy of NWs by capping has potential application in photovoltaics.

Additionally, to surface effects and strain, we find that crystalline structure of the NWs also play an important role in determining optical properties. In

particular we demonstrate type II spacial confinement of electrons and holes between different crystal polytypes of WZ and ZB. This is concluded from relatively long lifetimes measured and also a shift in emission energy below the value for GaAs ZB, which reflects a previously accepted 115meV band offset between GaAs WZ and ZB. The PL lifetime measured is 7.4ns for type-II confinement in uncapped GaAs NWs and 1.45ns for type-I recombination in the high quality pure ZB GaAs/GaAsP NWs.

Chapter 4

Exfoliation, characterisation and optical measurements of MoS_2

4.1 Introduction & motivation

In section 1.3 we introduced recent activity on 2D MoS_2 which has developed since the discovery of bright photo-luminescence (PL) detected for samples under 10 monolayers (ML) in thickness (19, 20). By considering the current research outcomes, we demonstrated potential applications such as in field effect transistors (79, 80, 81, 82, 83), flexible electronics (90) and optically pumped valleytronic devices (85, 86, 87, 88).

Although there is no published description of the technique specifically for MoS_2, the most common way of exfoliating 2D sheets is by the scotch-tape method (84). After exfoliation, graphene and MoS_2 are commonly deposited on silicon substrates which have been capped with SiO_2 (133). Graphene is found to have weak mechanical bonding with substrates, that leads to defects such as bubbles

(134) and ripples (135) in its morphology. MoS_2 has been measured to have similar weak mechanical bonding (136), but so far no detailed imaging of defects has been performed (137, 138). Additionally, a detailed understanding of the effect of substrate interactions on optical properties is required for MoS_2 (90).

At the time of starting the project there were very few examples of optical studies of 2D MoS_2 sheets and these primarily focused on very basic PL (19, 20, 103, 139). The direct band-gap PL spectra of MoS_2 are found to be composed of two emission bands, A and B, due to a splitting of the valence band. During our work a new paper was published, by Mak *et al.* (85), showing that, in field effect structures, the character of the emission of the A band can be changed from PL of a neutral exciton A^0 to PL of a negative charged exciton A^-. A further low energy shoulder L is found in the work of Korn *et al.* (103), which may be related to emission from states bound to surface impurities.

Despite the origin of A^0 and L being previously discussed, their behaviour is less well understood. We find that there is wide variation in spectral shape between different samples, which is related to the relative brightness of A^0, A^- and L. This can be seen when comparing different works in the literature but has not yet been highlighted in any publications. Prior to work presented in this thesis features A^0, A^- and L were only presented simultaneously in PL of a MoS_2 film by Mak *et. al* (107) and this was not the focus of their work. To explain this large variation it is therefore necessary to understand the processes which lead to formation and radiative recombination of these states.

4.1.1 Our work

Within this chapter we provide a detailed description of the method for mechanical exfoliating MoS_2 which was developed for this project at the University of Sheffield. This procedure has since been adapted for the exfoliation of GaSe, GaS, GaTe and $MoSe_2$ opening a new field of nano-physics in 2D materials. Using atomic force and ultrasonic force microscopy, in collaboration with O. Kolosov from the University of Lancaster, we investigate detailed morphology of MoS_2 sheets which are deposited on silicon substrates. We provide unique new images of defects; which include protrusions, bubbles and ripples. Although similar features have been found in graphene (134), this is the first time they have been imaged in detail for MoS_2.

Considering a large number of samples, we find a previously un-discussed variation in spectral shape between different MoS_2 sheets, something which is also reflected by variations between publications. We provide evidence that non-radiative processes are dominant in the recombination of electron-hole pairs in MoS_2. We find that competition between radiative and non-radiative processes affect the behaviour of PL when varying temperature and incident power. We find further evidence to support previous results showing a low quantum efficiency in MoS_2 (80), finding that PL emission does not saturate at high pumping powers.

Further to this, we demonstrate that PL emission is always dominated by the charged trion state, A^-, in a temperature range of 6.5-300K and suggest that this occurs partially due to capture of charges from the SiO_2 surface. We provide evidence showing that the large variation in PL line-shape is in fact most affected by the charge balance in the MoS_2 film. We find that, as electrons are

thermally activated in SiO_2 with increasing temperature, the relative intensity of both neutral exciton A^0 and low energy shoulder L drops and becomes undetected above 150K. We continue this work in Chapter 5 and investigate a way to control charge balance and therefore increase uniformity of PL properties.

4.2 Exfoliation techniques and sample details for MoS_2

The MoS_2 sheets produced in this work are created by the mechanical exfoliation (scotch-tape) technique which has commonly been used in the production of graphene sheets (84). Although similar, exfoliation of MoS_2 sheets differs significantly from graphene as the Van der Waal forces are much higher (140), meaning that a larger force is required to separate the layers. Although other single layer production methods have been demonstrated for MoS_2, including chemical vapour deposition (141), sonication (142), chalking and lithium intercalation (139), mechanical cleavage was chosen due to its simplicity. As the MoS_2 used in this report is from a natural mineral source and of an unknown purity, the number of intrinsic defects are unknown. Despite this, previously reports have suggested defects are lower in natural MoS_2 than MoS_2 grown by MBE (141). In this section the development of mechanical cleavage at the University of Sheffield is discussed and details are published for the first time.

4.2.1 Exfoliation by mechanical cleavage

Due to the weak forces between layers it is possible to separate planes of atoms in MoS_2 and eventually form a single layer consisting of a layer of Mo sandwiched between two layers of S, known as a monolayer (ML), as depicted in figure 4.2. Firstly, a crystal of MoS_2 is scratched against a piece of tape leaving behind a large amount of bulk material attached to the glue. The tape is then folded over and repeatedly pulled apart leaving a fine powder (between 5-500μm^2) of material

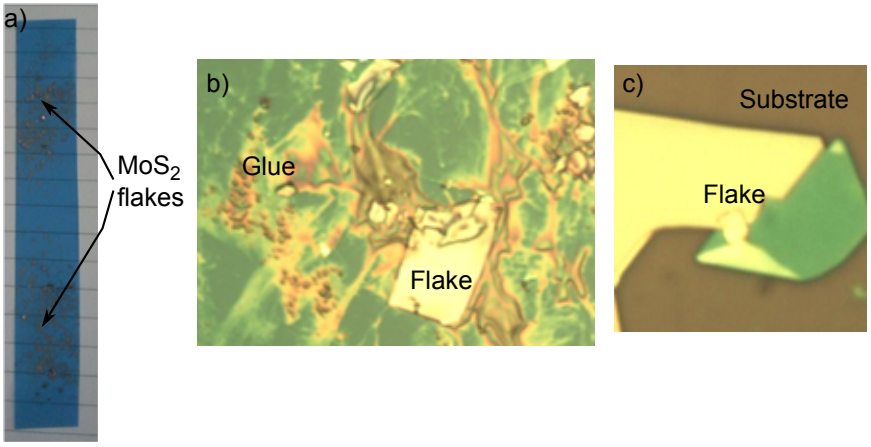

Figure 4.1: (a) A photograph of blue tacky-tape used in the exfoliation process where exfoliated MoS_2 can be seen on the surface. This has been exfoliated by folding the tape closed and pulling apart a number of times. (b) A microscope image of an MoS_2 sheet deposited on silicon using a tape type that contaminates the surface with glue. (c) A microscope image of an MoS_2 sheet deposited on silicon using blue tacky tape. Significantly reduced glue contamination can be seen.

as depicted in figure 4.1a. Although largely bulk material, there are enough MoS_2 sheets below 5ML left behind on the tape needed for experiments.

Substrates used for deposition were SiO_2 capped silicon wafers. These wafers are firstly cleaned using the solvents n-Butyl acetate, isopropanol alcohol (IPA) and acetone in order to remove any containments from the surface. In order to transfer MoS_2 from the sticky-tape to the substrate, the tape is placed on the surface and pressure applied. This is found to leave a large amount of the MoS_2 material behind which was previously attached to the tape. No further cleaning of the substrates was performed after deposition.

Initial results revealed a large amount of contamination from the glue as depicted in figure 4.1b. In order to reduce this, different tape types were investigated; each with different types and tackiness of glue. Wafer dicing tape, also

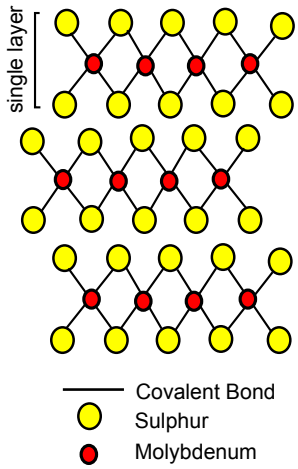

Figure 4.2: (a) A simplified diagram showing the atomic structure of bulk MoS_2. A layer of molybdenum atoms are sandwiched between two layers sulphur atoms, held together by covalent bonds. Subsequent layers are only weakly bound together by Van der Waals forces.

known as *blue-tacky tape* [EPAK Electronics, Medium Tack, Blue], with a medium tack was found to provide the best results - leaving behind a high yield of 2D sheets and almost no glue contamination, as depicted for comparison in figure 4.1c. As MoS_2 layers in contact between the substrate and the tape naturally split, it is reasonable to assume that no glue contamination exists on the MoS_2 film surface. By eliminating contamination from the surrounding substrates we assume that glue will cause no experimental issues, as proven by our PL studies.

4.2.2 Exfoliation by chalking and sonication

In the development of this project two other methods of deposition were trialled to investigate if better quality sheets could be produced by other methods. The first of these tried was chalking, where a bulk MoS_2 crystal is rubbed directly

against a substrate leaving a trail of broken off sheets similar to chalk on a blackboard. This method has previously been shown to successfully produce single layers of graphene from bulk graphite (84), but proved ineffective in MoS_2 with only thick bulk sheets being produced.

Sonication was the second method attempted. In this case a bulk crystal of MoS_2 was placed into a small volume of IPA in a sonic bath [Grant Ultrasonic bath XUBA1]. A high frequency ultrasound (100 kHz) wave was applied, which we hoped would provide energy to break the Van der Waal forces between layers. In order to remove solvents, the liquid/MoS_2 mix was pipetted onto a substrate and placed on a hotplate. Unfortunately, by increasing the duration of sonication for MoS_2 between 1-60 seconds, rather than decreasing the thickness, the sheets of MoS_2 were shattered into a thin powder, under 1μm in size, which was not suitable for measurements.

4.2.3 Dielectric capping of MoS_2

To investigate the properties of MoS_2 with a capping layer we prepared a number of samples which we then capped with a 100nm dielectric layer grown by plasma-enhanced chemical vapour deposition (PECVD). A diagram demonstrating the structure of the samples produced is given in figure 4.3.

PECVD deposition was done with a sample temperature of 300^{o}C. For SiO_2 deposition the reaction gasses used were SiH_4 and N_2O. For PECVD deposition these gasses are slowly released between two electrodes which are allowed to discharge producing a plasma of ions that is directed at the sample. These react on the surface to form a capping layer. The following reaction takes place during

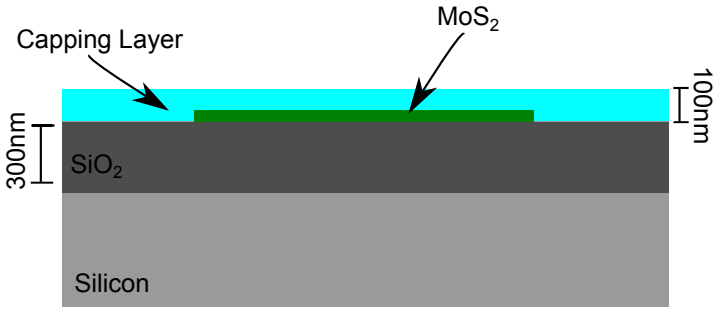

Figure 4.3: A cross section showing the layout of a MoS_2 sample which is capped. A 300nm layer of SiO_2 sits on the Si substrate surface and that MoS_2 is deposited onto this. An additional capping layer covers the MoS_2 and surrounding dielectric.

this process:

$$3SiH_4 + 6N_2O \rightarrow 3SiO_2 + 4NH_3 + 4N_2 \tag{4.1}$$

For deposition of Si_3N_4 the same process was used with the reactants SiH_4 and NH_3 leading to the reaction:

$$3SiH_4 + 4NH_3 \rightarrow Si_3N_4 + 24H_2 \tag{4.2}$$

The deposition times used in our work were 40nm per second for SiO_2 and 10nm per second for Si_3N_4 deposition.

4.2.4 Optical micrsocope images and visibility of monolayers

Despite being mostly transparent, thin sheets of MoS_2 are found to have a weak contrast when viewed on a Si/SiO_2 substrate. A common way of increasing this contrast is to use a specific thickness of SiO_2 capping on top of the Si substrate

which enhances the visibility of the sheets by constructive interference of light (133). This can be achieved for the green spectrum with a 300nm thick layer (as depicted in figure 4.3) and the colour green is chosen as this is the most sensitive wavelength region found in silicon CCD cameras commonly attached to laboratory microscopes.

In figure 4.4 we present a selection of MoS_2 sheets which are deposited on substrates prepared by this method. For bulk MoS_2, over 10ML in thickness, the contrast is metallic yellow and for sheets under 5 ML thickness the contrast is transparent green. In the literature this contrast is often used to estimate the thickness of MoS_2 with single monolayer accuracy (19, 20, 133). This has been replicated in figure 4.4 and the thickness of MoS_2 has been labelled between 1-5 ML.

A single ML of MoS_2 is measured to have a height of 0.6nm using AFM and subsequent layers increase the thickness by 1nm, giving thicknesses: 2ML=1.6nm, 3ML=2.6nm etc. (20). The increased thickness for bilayer MoS_2, compared to two single ML sheets, is due to the interlayer crystal spacing (143). By comparing the thickness measured in AFM with contrast in the optical microscope, we were able to confirm the accuracy of using this optical contrast method. All MoS_2 sheets measured in this report were found to be between 2-5ML(1.6-4.6nm) in thickness.

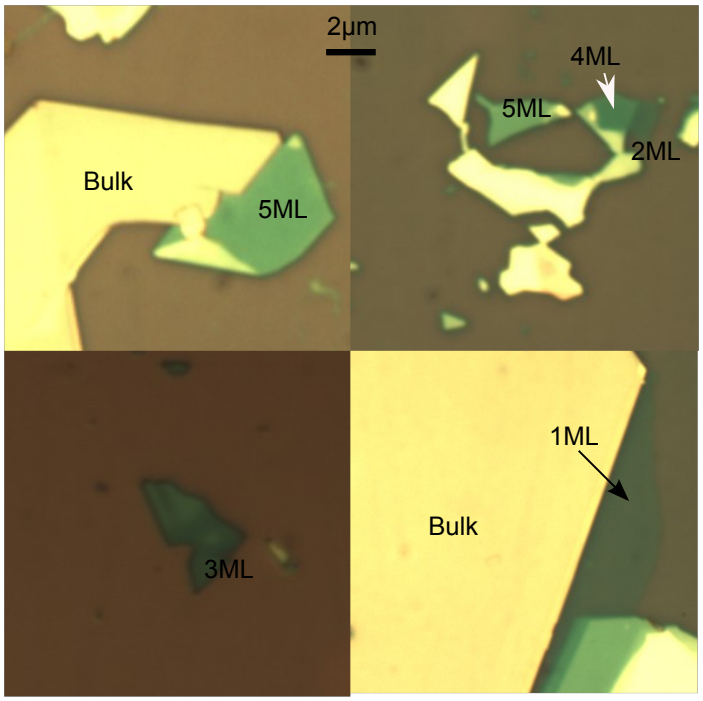

Figure 4.4: A selection of photos of sheets between 1-5ML in thickness. Bulk regions of MoS_2 are found to be opaque yellow where as thin MoS_2 sheets appear transparent green. Different green contrasts can be used to identify the MoS_2 thickness on a layer-by-layer basis and sheets of different thickness have been labelled.

4.3 UFM & AFM measurements of the morphology of MoS_2 on Si/SiO_2 substrates

MoS_2 sheets are found to be weakly bound to substrates (137) which is likely to lead to crumples and distortions in the morphology of the 2D sheet similar to those found in graphene (113, 134, 135, 136). The morphology of MoS_2 sheets deposited on a Si/SiO_2 substrate was investigated in collaboration with O. Kolosov at the University of Lancaster using both atomic force microscopy (AFM) and ultrasonic force microscopy (UFM). A description of these techniques is provided in section

2.2.

In these initial experiments the substrate was prepared by growing a SiO_2 layer by plasma-enhanced chemical vapour deposition (PECVD) and it had root mean squared roughness of 2nm and a maximum peak height of 15nm and therefore can be considered a relatively rough surface. In the UFM images shown the darker (lighter) regions correspond to softer (harder) parts of the MoS_2 sheet. In this case the softer (darker image) regions of Mo_2 correspond to weak contact with the substrate and highlight regions where the sheet is suspended.

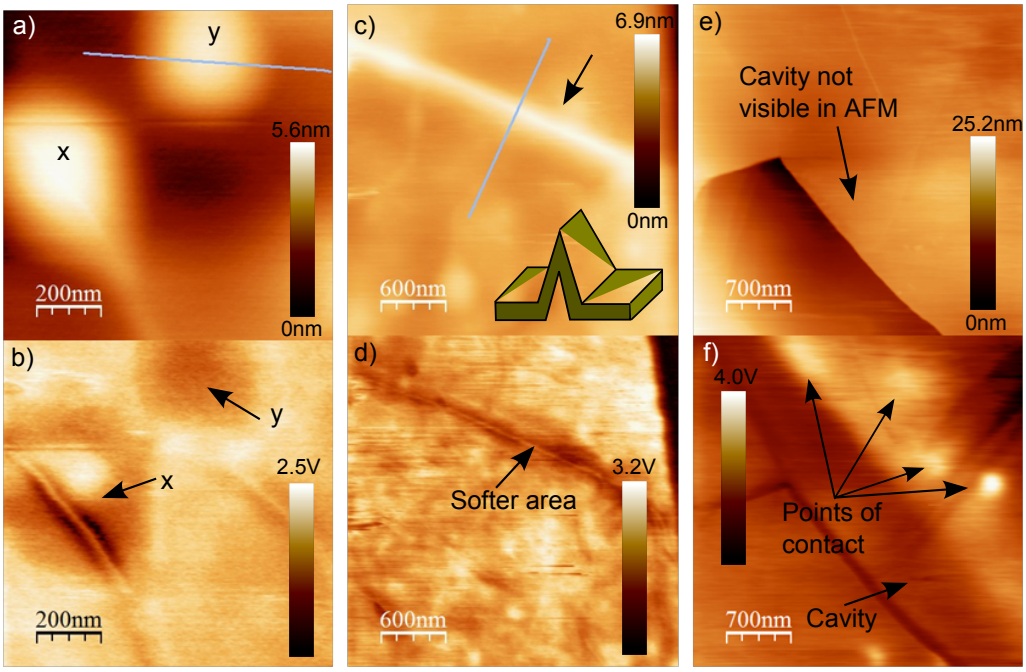

Figure 4.5: (a) An AFM image of bulges, labelled x and y, in an MoS_2 sheet. (b) A UFM image demonstrating that bulge x is formed by pressure underneath the MoS_2 and bulge y is a completely suspended bubble. (c) An AFM image and (d) UFM image demonstrating a ridge in the MoS_2 sheet as described by the insert. (e) An AFM image demonstrating that the cavity in figure (f) is only visible in UFM. (f) A UFM image demonstrating a cavity underneath a bulk region of AFM which is suspended on point contacts as labelled.

In figure 4.5 (a-b) we demonstrate a free standing bubble formed in the MoS_2 sheet, labelled y. We can see that this is a free standing bubble by comparing the AFM image in figure (a) with the UFM image in figure (b). In AFM it can be seen that this region bulges from the surrounding MoS_2 material and in UFM we can see that it is darker in contrast than the surrounding MoS_2 material. This dark contrast demonstrates that this region is much softer and we therefore expect it is suspended above the substrate. Free standing bubbles such as these may form in MoS_2 due to gasses trapped in a layer between the 2D sheet and the substrate as has been previously shown in graphene (134). This defect forms during the exfoliation process and occurs commonly even on relatively flat substrates.

Considering now the feature labelled x in the same figures (a-b) we can see that, while this appears to be similar the feature y in the AFM image (a), the centre of this feature has a much lighter contrast in UFM suggesting that it has strong contact with material beneath. This protrusion therefore forms due to contact with a defect on the substrate which pushes it upwards from the surrounding material. It can be seen further in the UFM image (b) that around the centre of this protrusion the MoS_2 is suspended, effectively hanging down around the defect forming a tent of material.

In the AMF image of figure 4.5(b) we highlight another common defect, a fold in the MoS_2 sheet, which is in this case approximately 150nm wide and 7μm in length. This can be interpreted from AFM and UFM measurements and we observed that this ridge runs edge-to-edge across a large area of MoS_2. We can interpret this as a fold by comparing contrast in the UFM image of figure 4.5(b) and it can be clearly seen that this region is suspended above the substrate. A small diagram of this defect is provided in the insert and we expect defects of

this sort to form due to the rather rough method of deposition used.

In the AFM image in figure 4.5 (e) we show what appears to be a flat region of MoS_2 which is free of defects. Considering the UFM image of this region, (f), we can see that there are in fact a large number of sub-surface defects not visible in AFM. It can be seen that a large portion of this region, which we assume to be much thinner than surrounding material, is completely suspended (denoted by the darker contrast) and rests on small point contacts as labelled. We expect that defects of this sort form during the mechanical exfoliation process. When the MoS_2 is attached to the tape, it is pulled apart a number of times producing regions of thin layers and relatively thicker layers. When deposited on the substrate thicker layers are sometimes found in contact with the substrate while the thin layers are deposited on top of these thicker regions. In this case a thin MoS_2 region effectively hangs on pedestals produced from thicker regions of MoS_2.

In figure 4.6 we show a thin layer of MoS_2 which rests on a thicker region at one edge and drapes over onto the substrate at the other. This can be seen, once again, but comparing AFM (a) and UFM (b) images. In the AFM image the contrast between the thick region (light) and thin region (dark) is clear. In UFM it can be seen that the thinner MoS_2 material in the region draped over thicker material is very soft (dark) and therefore we expect it to be suspended. More complicated defects form in this region due to the rough underlying substrate and in order to illustrate these we provide a drawing in figure 4.6(c).

The defects described in this section may introduce strain in the films (135) and are therefore expected to effect electronic and optical properties (143, 144, 145). Direct measurements for graphene which has been deposited on boron ni-

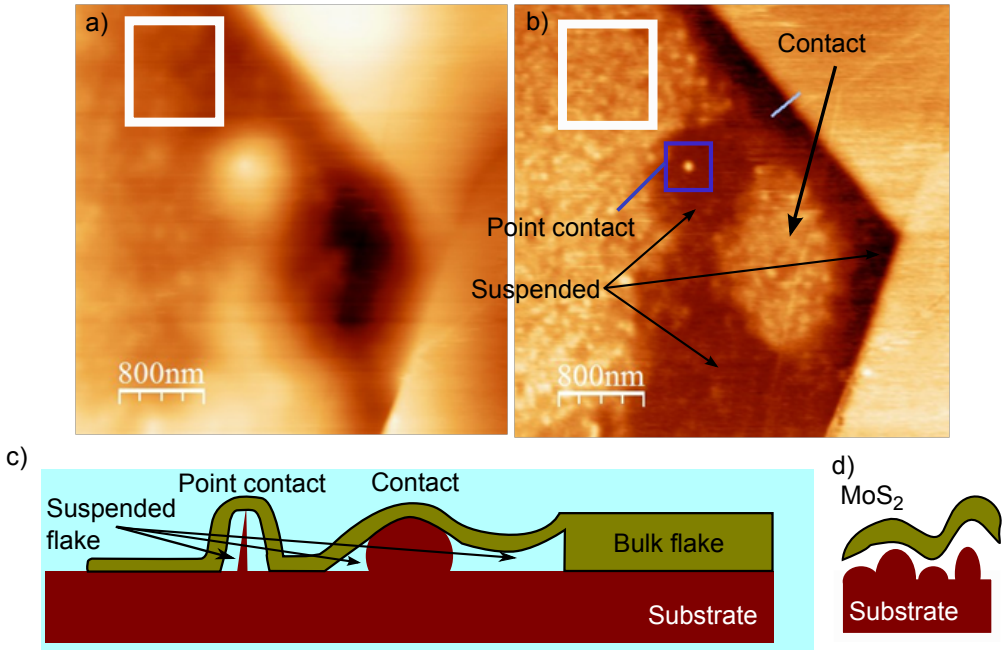

Figure 4.6: (a) An AFM image of a thin 2D sheet of MoS_2 which hangs down from a thicker region. (b) A UFM image of the same region which makes clear the cavities (dark contrast) also regions distorted by contact (light contrast) with the substrate. A region of large and a single pin-like point contact are labelled. An area, marked with a white square, is chosen to demonstrate how the roughness of the substrate also effects morphology. (c) A diagram showing how we expect this MoS_2 sheet to look interpreted from these AFM and UFM images. (d) A digram demonstrating poor mechanical contact and distortion of the MoS_2 sheet by the substrate roughness, for the region marked in white in figures (a) & (b).

tride substrates, in order to minimise similar defects, show a 3 order of magnitude increase in mobility compared with SiO_2 substrates (146). By considering the defects described above it is clear that some of these defects occur due to the MoS_2 being deposited on a rough substrate. In order to minimise the effect of the uneven substrate on optical properties, MoS_2 sheets considered for the remainder of this chapter are deposited on bought Si substrates which have been thermally capped by SiO_2. The root mean squared (RMS) of these substrates is 0.09nm

and the maximum height is 0.68nm thus providing significantly flatter surfaces than PECVD grown SiO_2.

In Chapter 5 we compare PL from rough PEVCD oxide and atomically flat thermal oxide substrates in detail. Here we find that the number of defects are significantly reduced by using the more atomically flat substrates and that mechanical substrate affect heavily PL properties. In order to explain the mechanical effect of our PECVD grown substrates on MoS_2 sheets we have highlighted a small region with a white square in figure 4.6 (a-b). This is a relatively flat region of 3ML thick MoS_2 sheet which is free from the large scale defects described above. It can be seen in the AFM image of this region that the MoS_2 sheet is rough and largely follows the underlying roughness of the PECVD deposited SiO_2. This can be further concluded by measuring the RMS of the MoS_2, which is 1.7 nm with a maximum height of 11 nm which is similar to the substrate. In the UFM image (b) we can see than this region, despite being defect free, still has relatively poor mechanical contact with the substrate, as described in the diagram in figure 4.6(d). It therefore appears to be resting on protrusions from the substrate and effectively hangs between these, forming quasi-suspended sections. In Chapter 5 we find that, despite having a much reduced RMS, that MoS_2 deposited on atomically flat substrates also have poor mechanical contact, although there is no suspension.

4.4 Optical PL measurements

PL emission from MoS_2 sheets was excited with a green diode laser ($\lambda = 532$nm) and collected with a single spectrometer and liquid nitrogen cooled CCD. The spectra presented here are measured with an incident power of 1mW and an integration time of 5 seconds.

4.4.1 Room temperature PL measurements

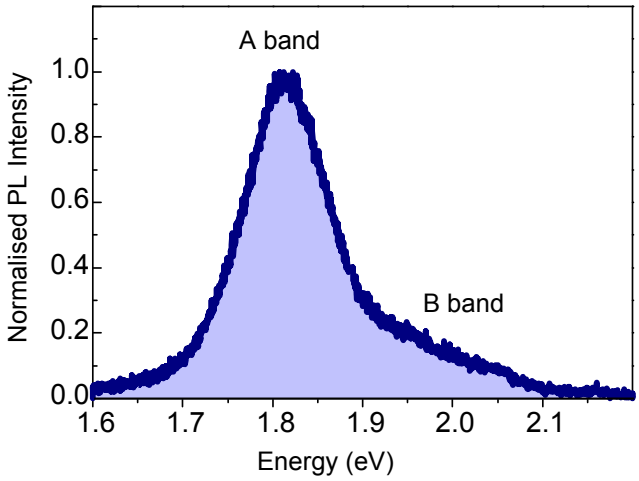

Figure 4.7: A photoluminescence spectrum collected for a single 3ML sheet of MoS_2 at room temperature. Both the A and B bands are labelled.

Considering more than 50 MoS_2 sheets under 5ML in thickness deposited directly onto Si/SiO_2 substrates we found a bright direct band-gap PL emission in each case. In sheets above 5ML thickness the PL spectra became too weak to detect in agreement with the previously reported exponential drop of PL intensity with increasing layer thickness (19). The signal we found at room temperature is formed by two bands, A and B, where A emits at 1.8eV and B at 2eV as

depicted in figure 4.7(a). These bands occur due to emission from split valence bands as previously reported (101, 105). In the case of this experiment we found the splitting between the centre of emission peak A and B to be 150meV which agrees well with theoretical calculations for the valence band (94, 108). For this work we focused only on the emission of the direct band-gap.

4.4.2 Position dependence PL measurements

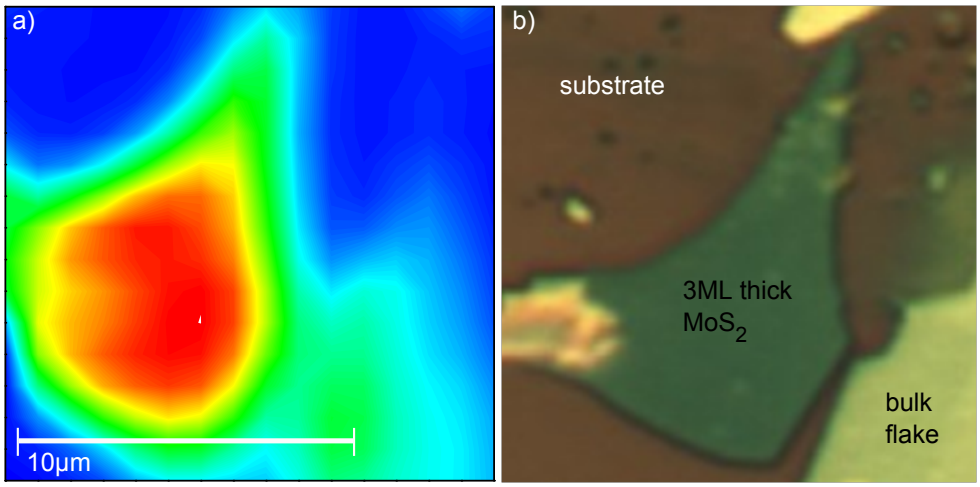

Figure 4.8: (a) A PL intensity map which can be compared to the photograph (b) showing a 3ML thin sheet of MoS_2. The PL intensity was collected at intervals of 0.5μm where red represents high signal and blue low signal.

In order to confirm that PL emission does not arise from either the substrate, scotch-tape glue or bulk sheets, position dependence measurements were carried out. For these measurements a PL spectra is collected at 0.5μm intervals by moving the sample and keeping the laser position fixed. The power of the laser is kept constant at 2mW with a collection time of 5 seconds for each position. A large power is used in order to maximise sheet emission and increase the contrast

of the image. It can be confirmed in figure 4.8 that a 2D sheet of MoS_2 (green contrast) produces a bright PL spectra, while the substrate and bulk do not.

4.4.3 Low temperature PL measurements

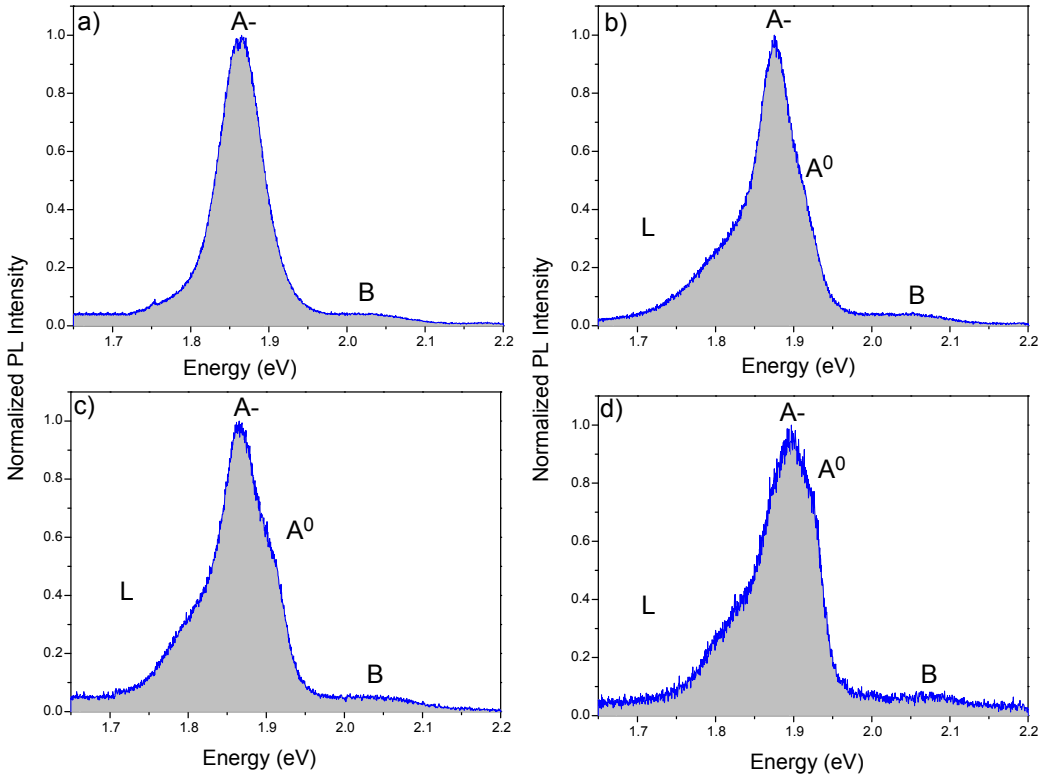

Figure 4.9: (a) A low temperature PL spectrum for a single MoS_2 sheet showing strong contribution of features A^- and B. (b)-(c) A selection of low temperature spectra for different MoS_2 sheets showing more pronounced emission from states A^0 and L as well as A^- and B.

After experiments at room temperature the sample was transported to a liquid helium continuous flow cryostat and cooled to 10K in order to collect low temperature PL. A selection of PL spectra collected in these conditions for different MoS_2 sheets is given in figure 4.9. It becomes clear here that upto 4 distinctive

features are clearly visible in the spectra. In the spectrum in figure 4.9(a) we can see a strong contribution of A− and B, similar to in shape to the spectra measured at room temperature. In the spectra in figure 4.9 (b-d) additional features A^0 and L are visible. Observations of A^0 and L are uncommon in the literature and this work is only the second (107) to publish a spectrum where all of these features are visible together.

We identify emission from A^0 and A^- as neutral and charged excitons, which is in agreement with experiments on charge-tunable devices where the concentration of electrons in the sheet could be varied in a large range by varying voltage (85). The energy splitting between A^0 and A^-, measured at 45meV, also agrees well with this result. The origin of L has previously been attributed to emission from excitons bound to surface impurities (103), although there is little theoretical or experimental evidence to support this assumption. It can be seen by comparing the spectra for different MoS_2 sheets in figure 4.9 that there is a variation in the lineshape related to these states which we found when considering large numbers of samples. Before this variation can be explored in Chapter 5, a new understanding of what factors affect the relative intensity of these states must be studied. This will be the focus of the remainder of this chapter.

4.5 PL temperature dependence of MoS_2

In the above discussion it is clear that emission from the neutral exciton state A^0 and the states related to the low energy shoulder L become more dominant in the PL spectra of MoS_2 at low temperature. In order to gain a greater understanding of the thermal processes which govern the relative intensity of optical emission from these states we collected a series of PL spectra at different temperatures. We used a laser power of 0.5mW and integration time of 10 seconds. The sample was placed in a continuous flow He cryostat and the temperature varied using a heater.

A plot of PL spectra of a single 3ML thick MoS_2 sheet collected at different temperatures is given in figure 4.10. It can be seen here that there is shift in the PL emission energy with with increasing temperature, which we will discuss later. A PL intensity drop with a factor of 5 is observed between 6.5-300K. This intensity drop is considerably smaller than, for example, the intensity drop for GaAs/GaAsP NWs in chapter 3 which was found to exceed a factor of 50.

Such weak variation of PL yield with temperature can occur for a number of reasons. For example, if the binding energies for excitons are very high they will not dissociate at high temperatures. Another explanation is related to competition between radiative and non-radiative processes in the film. Previous results have shown a dramatic increase in the PL yield for suspended MoS_2 (20) at low temperature, which suggests that non-radiative processes are strong in samples deposited on SiO_2 substrates. The quantum efficiency of MoS_2 (85) is also very low which may be related to a large number of fast non-radiative processes. If these non-radiative processes are sufficiently dominant at low temperature, ther-

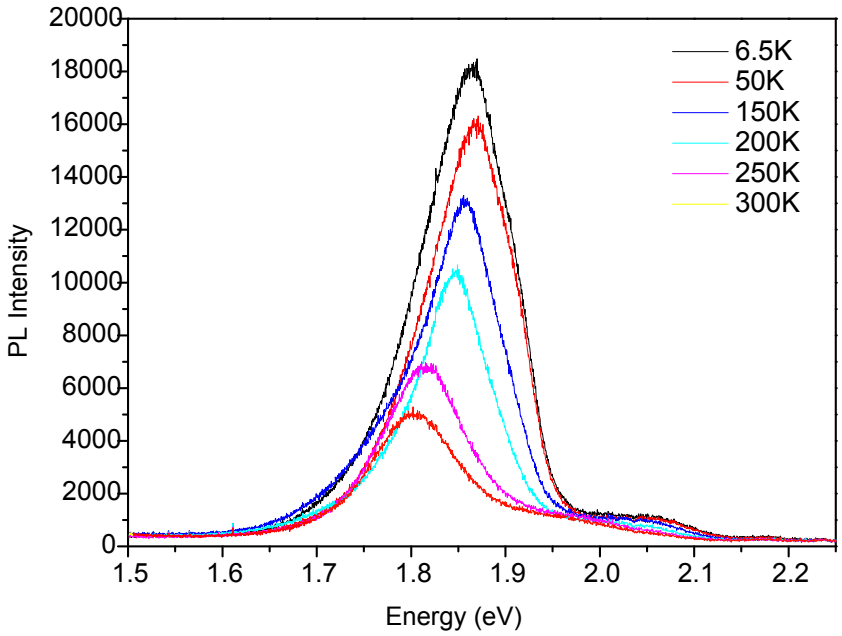

Figure 4.10: A PL spectra of a single sheet of 2D 3 layer thick MoS_2 measured at different temperature intervals between 6.5K and 300K.

mally activated processes will not be efficient enough to significantly alter the balance between existing non-radiative and radiative recombination. As well as this, because the samples considered in this work are 2-5 ML in thickness, recombination at the indirect band-gap will also act as an additional competitive path.

4.5.1 Dependence of the band-gap of MoS_2 on temperature

In figure 4.11(a) we show a graph demonstrating the dependence of the maximum emission energy for the A band with temperature for a large number of MoS_2 sheets. As the temperature drops it can be seen that the emission shifts to higher

energy. It can also be seen that at low energy there is a large variation of 40meV in position in energy of the A-band between the different MoS_2 sheets.

The behaviour of band-gap with temperature can be empirically modelled using the Varshni equation (26) where the bandgap ($E_g(T)$) dependence on energy is:

$$E_g(T) = E_g(0) - \frac{\alpha_E T^2}{T + \beta_E} \tag{4.3}$$

where T is temperature, $E_g(0)$ is the energy gap at absolute zero and α_E, β_E are constants specific to the material. These empirical fits can be used to predict emission energy and therefore used as a model to tune the position of the band-gap. Extracted fit values for this data are provided in table 4.1 and it can be seen here that the temperature dependence for these films shows somewhat different behaviour leading to a scatter in the fitting parameters. This scatter is particularly prominent for parameter α_E.

We repeated this investigation for MoS_2 sheets on the same SiO_2 substrates with an additional capping layer of SiO_2 as described in section 4.3. A graph showing temperature dependence for the emission energy maxima of the A peak between different capped MoS_2 sheets is given in figure 4.11(b). It can be seen in this case that the variation for emission energy at low temperature has reduced by a factor of 2 to 19meV, compared to the data for the uncapped films. The results of Varshni fittings are shown in table 4.2. Comparing these extracted values with the values for uncapped MoS_2 in table 4.1, it can be seen that the scattering in fitting parameters has been dramatically reduced. In fact the behaviour with temperature is now the same for all 5 MoS_2 films.

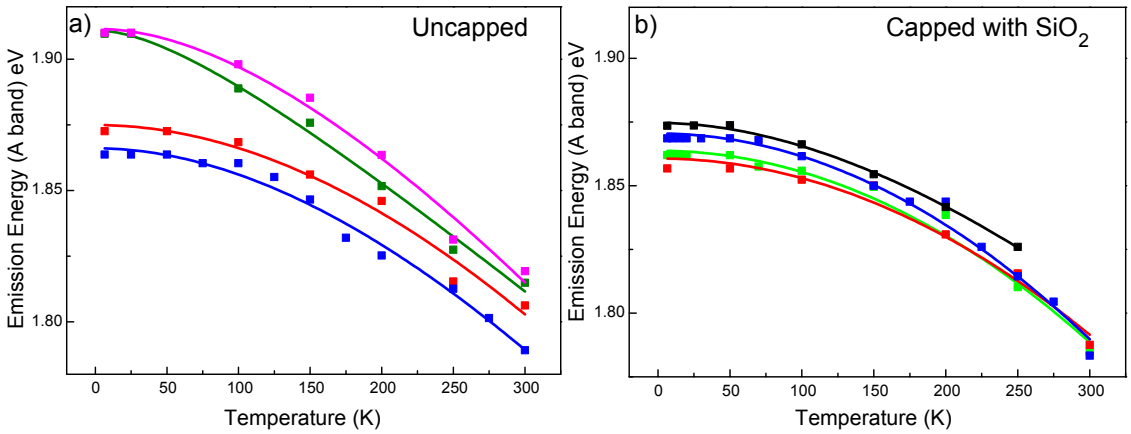

Figure 4.11: (a) Graph demonstrating for various uncapped films of MoS_2 the A band position shift with temperature. (b) A graph demonstrating the same information for films capped with SiO_2. The fitting for these vales is a varshni dependency as described in the text.

We therefore demonstrate that for uncapped films the behaviour with temperature is less regular than for films capped with an additional material. The parameter β_E is often linked to the Debye temperature, which relates the phonon contribution to the specific heat capacity and α_E is related to the shift in badgap E_g with temperature in units of eV/K (147). The shifting band-gap is related to the relative positions of the valence and conduction band and therefore the relative positions of atoms in the lattice. It can therefore also be related to strain.

As the temperature of the sample is reduced the SiO_2 substrate lattice is likely to contract at a different rate to the MoS_2 lattice which will introduce strain into the film. In section 4.5 we show that, for uncapped films, the mechanical contact between MoS_2 and substrate is weak and none uniform which we suggest accounts for a non-uniformity in strain leading to a scattering in the coefficient α_E between samples. In chapter 5 we find that the addition of a capping layer forces the mechanical coupling between the MoS_2 sheet and substrate to increase. By in-

creasing the coupling to surrounding layers we expect the strain to increase which is reflected by a larger contribution of α_E for capped samples. In Chapter 5 we show that, by increasing mechanical bonding with the substrate, non-uniformities in mechanical properties of MoS_2 are reduced. This is clearly reflected here by a reduction in the scattering of parameters α_E and β_E. Further to this, in chapter 5, we also demonstrate a narrower linewidth for capped structures which may reflect reduced inhomogeneous broadening which would be related to a reduced variation in strain. This is difficult to quantify as, in this case, the line widths are also heavily dominated by charging.

Table 4.1: Extracted results of Varshni equation fitting for uncapped films.

Flake Number	α_E (ev/K)	β_E (K)	$E_g(0)$ (eV)
1	$6\pm3\text{x}10^{-4}$	400±50	1.87±0.003
2	$3\pm0.7\text{x}10^{-4}$	100±50	1.91± 0.003
3	$6\pm1\text{x}10^{-4}$	300±50	1.91± 0.003
4	$5\pm0.4\text{x}10^{-4}$	300±50	1.87± 0.003
5	$4\pm0.5\text{x}10^{-4}$	300±50	1.87± 0.003

Table 4.2: Extracted results of Varshni equation fitting for capped films.

Flake Number	α_E (ev/K)	β_E (K)	$E_g(0)$ (eV)
6	$6\pm0.5\text{x}10^{-4}$	400±50	1.87±0.003
7	$6\pm0.5\text{x}10^{-4}$	400±50	1.87± 0.003
8	$6\pm0.5\text{x}10^{-4}$	400±50	1.87± 0.003
9	$5\pm0.5\text{x}10^{-4}$	400±50	1.87± 0.003
10	$6\pm0.5\text{x}10^{-4}$	400±50	1.87± 0.003

4.5.2 Behaviour of individual states of MoS_2 with temperature

Comparing temperature dependence of emission from the individual states A^-, A^0 and L separately is difficult due to the overlapping features and large variation in linewidth and fitting the spectra with Gaussian peaks proved inconsistent. For this reason a more intuitive fitting method was devised in order to extract information. In figure 4.12 we demonstrate this fitting procedure on a typical PL spectrum, which is given in black. Firstly the central (and strongest) peak of A is fitted to a Gaussian function with a fixed amplitude and peak energy around the PL signal, as marked in green. By subtracting the intensity of this fitting to the PL peak we are left with the blue trace in figure 4.12. This blue trace highlights PL emission from features L and A^0 making them easier to evaluate, which we use to provide useful information about their behaviour.

This is a very rough method of fitting. For example we assume that A^- is much stronger than other features and that states giving rise to A^0 and L are isolated and do not have any intensity around the energy corresponding to the PL maximum. Also, only a very limited portion of the spectrum is actually used in the fitting. Despite the inaccuracy of this fitting method, it is still possible to extract useful qualitative understanding of the behaviour of these features.

Figure 4.13(a) shows 4 spectra collected from the same MoS_2 sheet at different temperatures and fitted using the method described here. It can be seen clearly that trion state A^- is the dominant emission state throughout the temperature range used in this experiment, which suggests that MoS_2 sheets are charged. Both n-type and p-type behaviour has been detected for MoS_2 (99, 148) which is

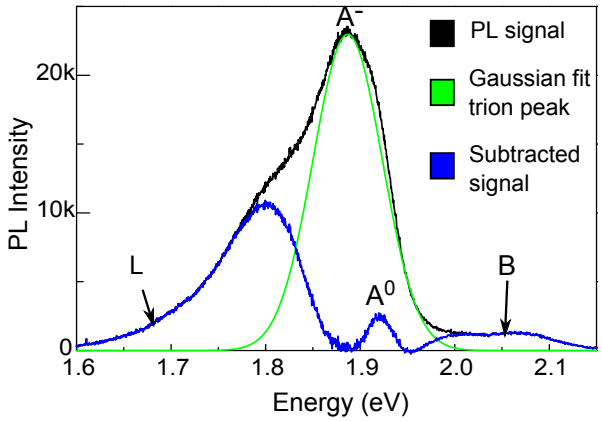

Figure 4.12: A diagram demonstrating a fitting method used for qualitative analysis of individual spectral features in the PL spectrum of MoS_2. The black trace represents a PL spectrum for a single MoS_2 sheet. The green trace represents a Gaussian fit of the signal maximum (A^-) and the blue trace represents this fitting subtracted from spectrum. This is a very rough fitting mechanism and the limitations are described in the text.

expected to be related to complex charge interaction at the MoS_2/SiO_2 interface (149). Alternatively, charges could originate from impurities in the MoS_2 film itself, which would exhibit similar transistor and PL behaviour. To understand the origin of charges in MoS_2 we provide further evidence in Chapter 5, by comparing PL spectra with substrate interactions, to show that emission from A^- is strongly related to electron capture from the substrate, although intrinsic impurities may also still effect.

In figure 4.13 we observe a much weaker contribution of A^0 as temperature is increased and the eventual disappearance of A^0 above 200k. By increasing the temperature, the probability of electron activation in the substrate (or intrinsic defects) is increased and we attribute this observation to increase charging of the MoS_2 sheet. Further to this, considering A^0 and L in figure 4.13, it can be seen that they have a correlation for intensity behaviour. To provide further evidence

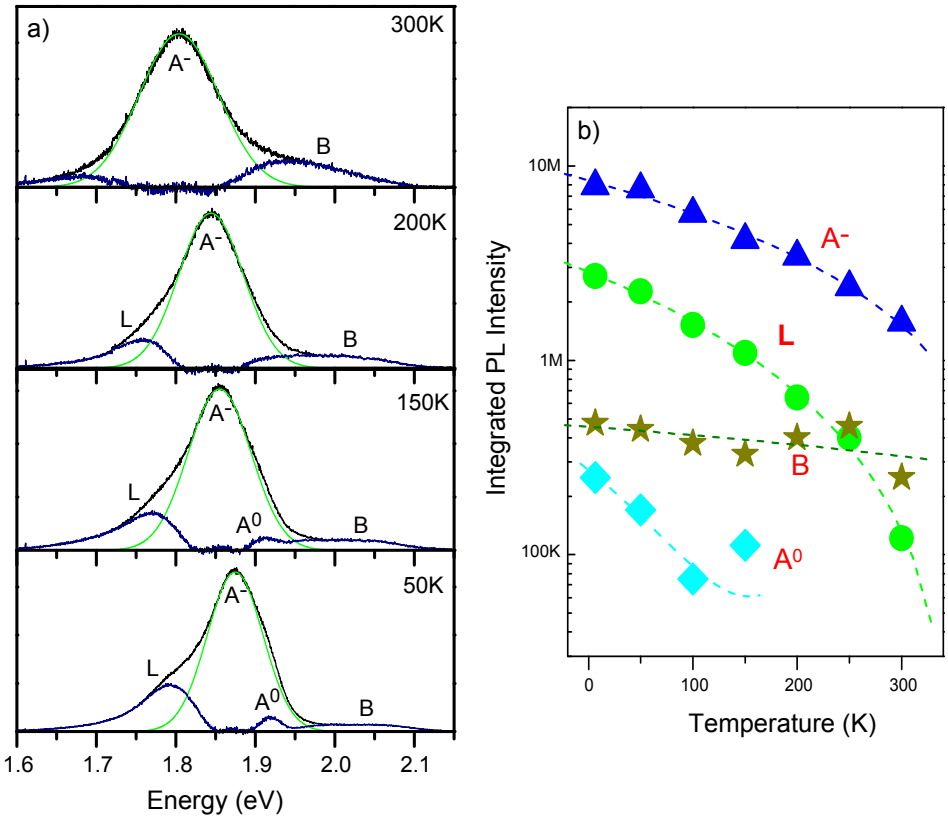

Figure 4.13: (a) A diagram demonstrating PL Spectra at different temperatures between 50-300K. The fitting method described in figure 4.12 is used here to highlight the changing shape of emission at different temperatures. Here the black trace is a PL signal, green is Gaussian fit and blue is the Gaussian peak subtracted from the PL spectrum. It can be seen that for the temperature range considered A^- is the dominant dominant feature and that at higher temperatures above 150K emission from A^0 and L disappears. (b) Graph of integrated PL intensity for spectral features at different temperature as estimated by the fitting method described in the text. In this case the fitted lines are only provided as a guide.

of a link between L and A^0 we compare different MoS_2 sheets in Chapter 5 and find that for MoS_2 sheets where A^0 is bright, there is a large contribution of L, and for sheets where A^0 is low the L peak is weak or not detected. This therefore

suggests that surface bound impurity states which contribute to this L band are similarly suppressed by negative charging. Alternatively, the states giving rise to the L band may be depleted due to thermal activation of trapped carriers from these states.

Another interesting new observation, which is clear in the spectra even without fitting individual peaks, is that the relative intensity of recombination of excitons contributing to the B peak is much less dependent on temperature than the intensity A^-, A^0 and L. In figure 4.13(b) we provide a diagram showing the behaviour of signal intensity against temperature for each of the spectral features. This is again a result of a rather rough fit and cannot be used to extract any quantitative information, but rather demonstrate trends. The lines provided on the diagram are only to aid the eye. This diagram is though very useful to compare the states bound to the A band and those to the B band. It can be seen that while the intensity of brightest state A^- drops by approximately a factor of 5, the decrease in B is only a factor of 1.5. One possible explanation for this is hole thermalisation which would lead to a higher hole population in the B band at higher temperature. Previous work has shown that valley polarization is less efficient at room temperature (108) which may be accounted for by this transfer of holes between the two bands.

4.6 PL power dependence in MoS_2

To understand better the optical processes in MoS_2, a PL signal was collected for a single 3ML sheet for a series of different incident laser powers and at low temperature (10K) with an integration time of 10 seconds. These collected PL

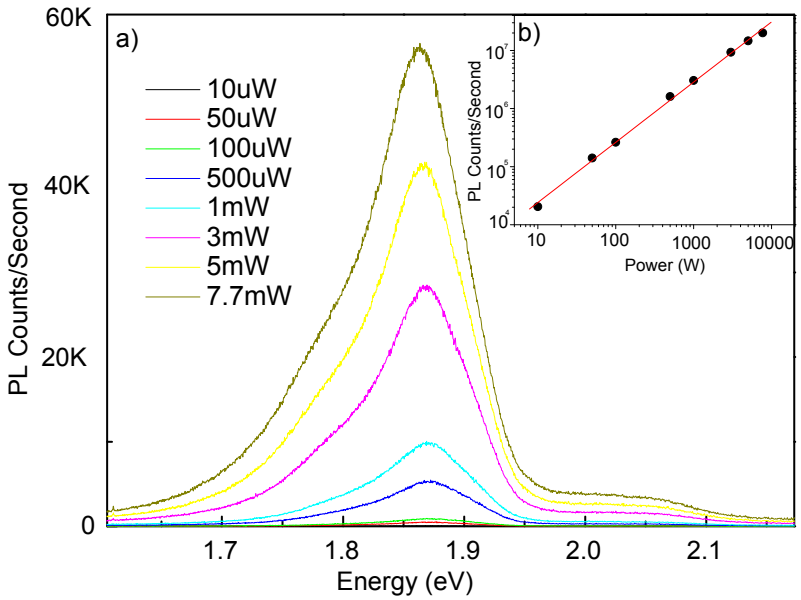

Figure 4.14: (a) A series of PL spectra collected for the same MoS_2 sheet at different incident powers. (b) A plot of incident power against intensity of PL signal for the same sample. It can be seen that no saturation occurs in the range of powers between 0-7.7mW.

spectra are presented in figure 4.14(a) and it can be seen clearly that by increasing the excitation density, the intensity of PL signal increases. In figure 4.14(b) we plot the total integrated intensity for each of these spectra as a function of power. It can be seen here that the PL yield increases linearly over the entire range. In fact, on all spectra measured we found a linear increase of integrated PL yield with increasing laser power between 0-7.7mW without saturation.

The absence of saturation at these high pumping powers could suggest low absorption efficiency for the laser photons into MoS_2. This observation could also be related to a low quantum efficiency of MoS_2 which is previously measured at 10^{-6} (80) compared to near unity values in other direct band-gap semiconductors. Additionally, as we are considering samples with thickness between 2-5ML, the

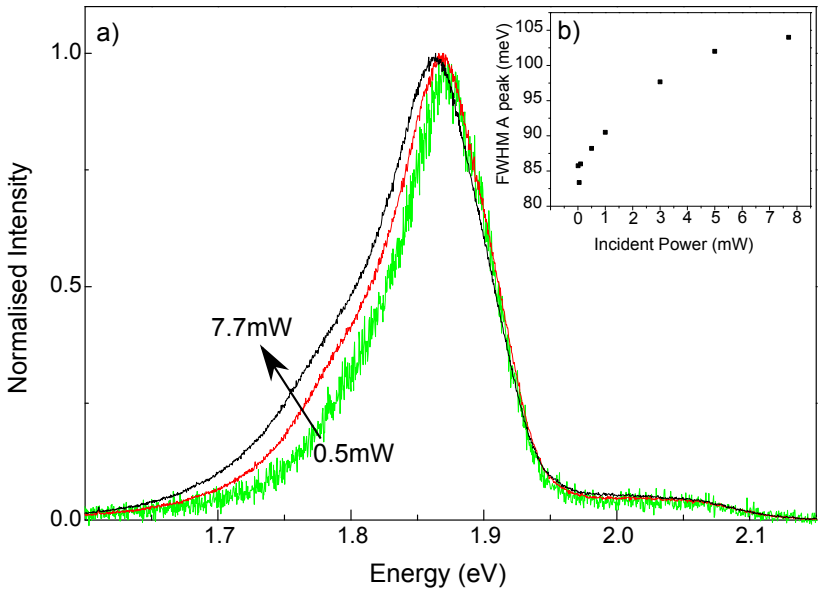

Figure 4.15: (a) A plot showing how the full width of half maxima (FWHM) of the PL signal increases with incident power for the MoS_2 sheet in figure 4.14. (b) A plot of normalized intensity for the PL signal at 0.5mW, 3mW and 7.7mW showing the change in signal shape. It can be clearly observed that the increase in linewidth is related to enhancement of state L with excitation density.

indirect bandgap will also act as a competitive path against direct band-gap recombination. As indirect recombination may be strong and the generation of electron-hole pairs will be weak it would be naturally expected that saturation of excitons at the K-point would be difficult to achieve, even at high pumping powers.

When comparing the spectral shape collected from this MoS_2 sheet at different pumping powers, we observed a broadening of the signal. In order to investigate this we measured the full width at half maximum (FWHM) for each of the spectra and a plot of this against pumping power is given in figure 4.15(b). It can be seen that as the power is increased from 1 to 7.7mW the FWHM increases significantly by 20meV. In order to investigate this further, we normalized the PL spectra for

MoS_2 at a power of 0.5mW, 3mW and 7.7mW and plotted them together in figure 4.15(a). It can be seen that this increase in the FWHM is due to a relatively fast increase of the L peak with excitation density.

At higher pumping powers the radiative recombination of electron-hole pairs therefore becomes more favourable for states giving rise to the L-band at a faster rate. This may reflect further complex competition between radiative and non-radiative paths in the MoS_2 sheet. In this case this could be because the non-radiative processes in the L peak saturate at high densities allowing the radiative paths to become more favourable.

4.7 Summary of results

In this chapter development of fabrication procedures for thin sheets of MoS_2 is presented, which has since been adapted for exfoliation of GaSe, GaS, GaTe and $MoSe_2$ opening a new field of 2D materials. We investigate in detail the morphology of MoS_2 sheets produced this way which we deposited on Si/SiO_2 substrates and we show detailed images of typical defects which break the periodicity of the lattice, which are likely to affect mobilities and optical properties of thin sheets.

We find that MoS_2 sheets under 5 monolayer in thickness produced by our method are bright emitters of light. The signal is composed of peaks A and B originating from a split valence band. The A band is composed of recombination of a neutral and a charged exciton, A^0 and A^-, and a shoulder L which may be related to surface bound impurities. We find that the relative intensity of these states varies between different MoS_2 sheets.

Although we do not measure non-radiative processes directly, we find indirect evidence that they are significant in determining the optical behaviour of MoS_2. We find that temperature dependence of the PL yield is weak. We suggest that this is due to the dominance of non-radiative and indirect processes at low temperatures which means that thermally activated non-radiative paths have less noticeable effect. We also find that, with increasing laser pumping power, the relative intensity of the L band changes. This is also likely related to competition between non-radiative and radiative recombination. A low quantum efficiency of MoS_2 means that non-radiative processes have a high rate, which is reflected by the intensity of PL not saturating with laser pumping power, even at high powers.

We also provide preliminary evidence of the effects of charge transfer between MoS_2 and the SiO_2 substrate, an effect we investigate in greater detail in Chapter 5. We show that the MoS_2 spectrum is dominated by emission from a negative exciton, A^-. We find that, with increasing temperature, the relative intensity of PL emission from neutral exciton A^0 reduces and eventually disappears. We suggest that this is due to the MoS_2 film capturing charges which can thermally activated in the SiO_2 substrate or the MoS_2. We find that the emission of L is also similarly effected by temperature and we suggest that these states are also sensitive to charge.

We also find that the addition of a capping layer reduces scattering in the fitting parameters for the Varshni dependency of the bandgap with increasing temperature, between different MoS_2 samples. In Chapter 5 we continue work on capped MoS_2 and also MoS_2 on substrates with different roughness. We find that the effects of charging and also strain, as introduced in this chapter, heavily influence optical properties through contact with the substrate. Here we demonstrate that the addition of a capping layer can increases the uniformity of emission properties between different MoS_2 sheets due to increased mechanical bonding with the substrate.

Chapter 5

Optical investigation of the natural charging of a few monolayer MoS_2 films deposited on dielectric substrates

5.1 Introduction & Motivation

It has previously been noted (80) that we currently have a poor understanding of substrate interactions on the optical properties of MoS_2. This is a particularly timely subject as one current research goal is based on creating hetrostructures out of stacks of 2D materials, including MoS_2 (75, 76), and therefore environment interactions will play a large part.

Due to the maturity of the field, substrate interactions with 2D materials have been investigated in much greater detail for grapehene layers. In this case sub-

strate interactions are found to greatly influence their properties, for example the mobilities found for suspended graphene are $7x10^6 cm^2V^{-1}s^{-1}$ (150) compared to a value of $1x10^4 cm^2V^{-1}s^{-1}$ for graphene on Si substrates (8). One suggested mechanism for this reduction in mobility is electron scattering from acoustic phonon modes which originate in the substrate (151). Another cause is the introduction of disorder into the 2D sheet. This can be seen in the example of graphene deposited on boron nitride substrates, which has a similar lattice structure to graphene, which show an enhancement of mobility of up to 3 times compared to disorder introduced by SiO_2 substrates (146).

A similar effect is expected for transport in MoS_2 transistors. Measurements of MoS_2 on SiO_2 show mobility values of $200 cm^2V^{-1}s^{-1}$ (80) while theoretical calculations for suspended sheets suggest a value of 400 $cm^2V^{-1}s^{-1}$ (97). Surface interactions are still not completely understood and more insight is required. PL is a good method for exploring MoS_2-substrate interactions, as measurements will be sensitive to local strain, defects and charging. A reduction in PL yield has previously been shown when comparing suspended MoS_2 with sheets deposited on a SiO_2 substrate, which they attribute to substrate-phonon interactions (19). In this work we present, for the first time, PL measurements of MoS_2 on substrates of different roughness to gain a greater understanding of substrate effects on 2D sheets.

5.1.1 Capping influences

We introduced capping of MoS_2 and other 2D materials in section 4.3. Previous studies of the influence of a capping layer on the surface of MoS_2 and graphene

have focused on high-k dielectrics such as Al_20_3 and HfO_2. These materials are used to influence mobilities in transistors by screening Coulomb interactions from the MoS_2 or graphene channel which reduce mobility by scattering electrons. Capping with these materials is commonly used in engineering of transistors, including both MoS_2 (79, 97, 98) and graphene (8, 59, 152). Optical properties of MoS_2 capped with Al_20_3 and HfO_2 have been studied in a recent work (153). The authors emphasised the influence of strain, due to a lattice mismatch between capping material and substrate, which is shown to cause a shift in the band-gap of PL. However, no detailed and systematic study of the PL lineshape has been done which, as we show here, sheds new light on interactions of thin films of MoS_2 with its environment.

5.1.2 Our Work

In this chapter we focus on interaction of MoS_2 films with SiO_2 and Si_xN_y commonly used in photonic devices and report low temperature PL measurements on over a 100 thin films, enabling detailed insight in interactions of MoS_2 with its dielectric surrounding. We study mechanically exfoliated MoS_2 films deposited on silicon substrates finished with either nearly atomically flat thermally grown SiO_2 or relatively rough SiO_2 grown by plasma-enhanced chemical vapor deposition (PECVD). In our study we use a combination of low temperature microphotoluminescence (PL), atomic force microscopy (AFM) and ultrasonic force microscopy (UFM). We find marked variety of the PL spectral lineshapes and peak energies in the large number of few monolayer MoS_2 films compared, which nonetheless show trends that we are able to relate to electrostatic and mechanical

interaction of thin films with the surrounding dielectrics.

We find that high mechanical coupling between a MoS_2 film and the surrounding layers is only possible for capped films on thermally grown SiO_2, whereas more complex morphology and poorer contact with the surrounding layers is observed for uncapped films, the effect further exacerbated for films on PECVD substrates. Following this observation, we show a direct correlation between the enhanced mechanical coupling of MoS_2 with the surrounding dielectric layers and increased negative charging of the films, directly affecting spectral characteristics of PL due to the presence of the pronounced PL peak of a negatively charged trion. Importantly we find that this process leads to more reproducible PL properties, including linewidth, lineshape and emission energy.

5.2 Sample details

Samples were produced using the same method described in Chapter 4. Further MoS_2 samples were produced using the same technique, but deposited on Si substrates covered with 300 nm PECVD grown SiO_2 (as described below). The root mean square (rms) roughness, R_{rms}, of the PECVD grown SiO_2 is found to be 2 nm with a maximum peak height of 15 nm, whereas R_{rms} of the thermally grown SiO_2 is 0.09 nm with a maximum height of 0.68 nm. The thin MoS_2 films had optical contrasts corresponding to thicknesses of 2-5 MLs, confirmed by AFM on thermal oxide substrates. The additional capping of the $MoS_2/SiO_2/Si$ samples with Si_xN_y and SiO_2 was carried out using the same PECVD techniques. The complete $SiO_2/MoS_2/SiO_2/Si$ or $Si_xN_y/MoS_2/SiO_2/Si$ samples had the top Si_xN_y and SiO_2 layers with thicknesses of 100 nm for PL and 15 nm for AFM/UFM measurements.

5.3 Optical PL measurements

In this section comparisons of PL emission from MoS_2 are discussed. This provides important observations of how different spectral features A^-, A^0 and L behave. In the previous section we discussed that A^- is emission from a negative exciton, A^0 from a neutral exciton and we also demonstrated that L is sensitive to charge. The origin of L is so far not fully understood but may be related to surface states (103). These spectra are collected at 10K using continuous wave above bandgap excitation (532nm) as described previously (section 4.4.1).

5.3.1 Analysis of spectral lineshape

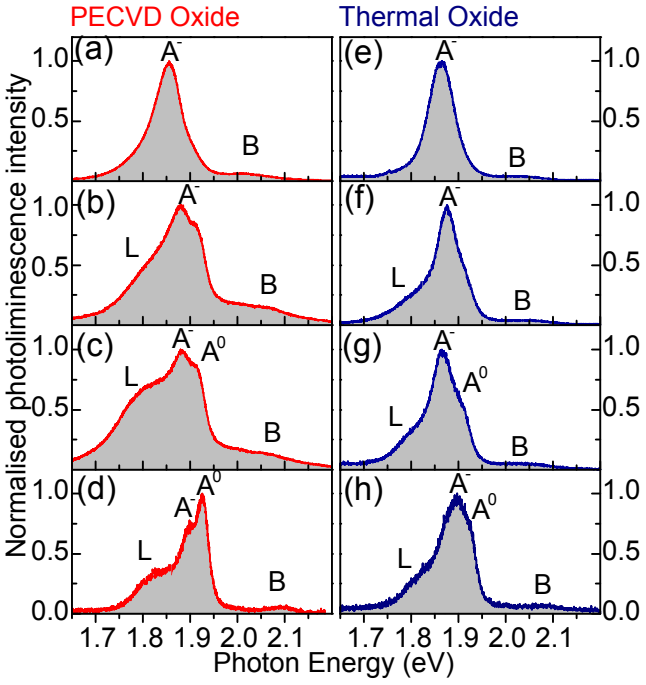

Figure 5.1: PL spectra measured at 10K for individual mechanically exfoliated MoS_2 uncapped films deposited on a 300 nm SiO_2 layer grown by either PECVD (a-d) or thermal oxidation (e-h) on a silicon substrate.

Fig. 5.1(a) shows a selection of PL spectra measured for a few monolayer (ML) uncapped MoS_2 films deposited on Si substrates with either PECVD (a-d) or thermal oxidation (e-h). In all spectra exciton complexes A and B are clearly visible (20), although there is a large variation in PL lineshapes for different films. The A complex is composed of a trion PL peak A^- and a high energy shoulder A^0 corresponding to neutral exciton PL (85). A low energy shoulder L is also observed in some spectra, though spectra showing weak or no contributions of L and A^0 states were observed on both PECVD (a) and thermal oxide (e) substrates. A relatively large contribution of L and A^0 was found in many films deposited on PECVD substrates (b, c) and in some cases the neutral exciton was found to have brighter emission than the trion [as in (d)]. For films deposited on thermal oxide substrates, there is a less significant variation in the lineshape (e-h) and L and A^0 features are, in general, less pronounced relative to A^- than in films deposited on PECVD grown SiO_2.

The effect of additional capping of MoS_2 films with dielectric layers is demonstrated in Fig.5.2. A 100 nm thick layer of either SiO_2 or Si_xN_y is deposited using PECVD on top of the $MoS_2/SiO_2/Si$ samples for both PECVD and thermal SiO_2/Si substrates. Here we observe even less variation in lineshapes between the films. A further suppression of the low energy shoulder L and neutral exciton peak A^0 is found for films capped with Si_xN_y (a,b,e,f) on both types of substrates and with SiO_2 on thermally grown substrates. In contrast, L and A^0 peaks are pronounced when capping with SiO_2 is used for MoS_2 films on PECVD substrates. Further to this, from comparison of spectra in (a,b,c,d) and (e,f,g,h), we find that the PL linewidths of films deposited on the PECVD oxide are notably broader than for those on the thermal oxide substrates.

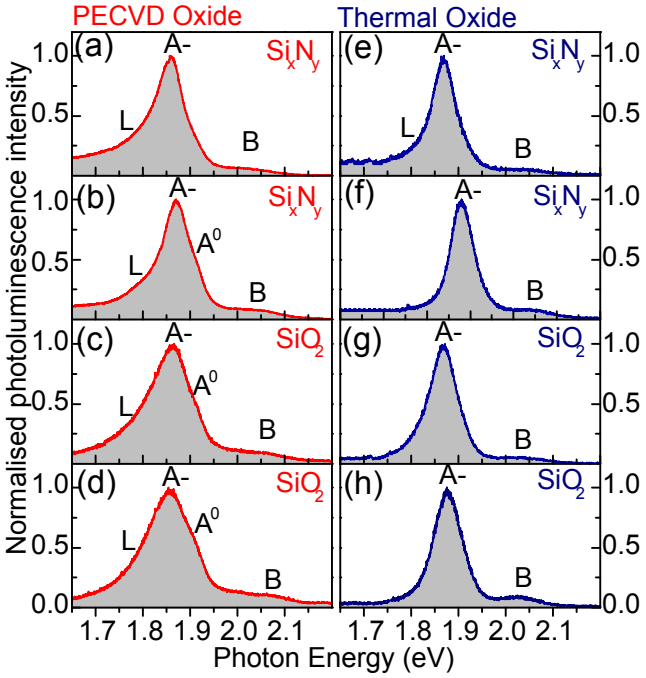

Figure 5.2: PL spectra measured for individual mechanically exfoliated MoS_2 films capped by a 100 nm PECVD layer of dielectric material. The effect of capping is shown for films deposited on PECVD grown SiO_2 substrates for SiN (a, b) and SiO_2 (c, d) capping layers, and also for films deposited on thermally grown SiO_2 and capped with SiN (e, f) and SiO_2 (g, h).

An interesting trend in all spectra presented in Figs.5.1 and 5.2 is a correlation between the intensities of the features L and A^0: the two peaks are either both rather pronounced or suppressed in any given spectrum relative to the trion peak A^-. This may imply that peak L becomes suppressed when the film captures an excess of negative charge, similar to the observations of the previous chapter.

5.3.2 Analysis of emission energy

A statistical analysis of PL peak energies for films deposited on the two types of substrates is presented in Fig.5.3. Fig.5.3(a,b) show that the average values for the PL peak energies, E^{av}_{max}, for uncapped films are E^{av}_{max} = 1.88 eV for the PECVD substrates and E^{av}_{max} = 1.88 eV for thermal oxide substrates, with an almost two times larger standard deviation, σ_{Emax} for the former (18 versus 11 meV). The data collected for the capped films (shaded for Si_xN_y and hatched for SiO_2) are presented in Fig.5.3(c) and (d) for the thermal and PECVD oxide substrates respectively. Significant narrowing of the peak energy distribution is found in all cases: σ_{Emax} ≈6 meV has been found. The average peak energies are very similar for both SiO_2 and Si_xN_y capping on the thermal oxide substrates (E^{av}_{max}=1.874 eV), but differ for PECVD substrates: E^{av}_{max}=1.862 and 1.870 eV for SiO_2 and Si_xN_y capping respectively.

From previous reports (19), for films with thicknesses in the range 2 to 5 MLs, one can expect the PL peak shift on the order of 20 meV. In addition, PL yield was reported to be about 10 times higher for 2 ML films compared with 4 ML and for 3 ML compared with 5 ML (19). In our study, the integrated PL signal shows a large variation within about one order of magnitude between the films. The dependence of the PL yield on the type of the substrate and capping is not very pronounced. While our data for PL intensities is consistent with that reported in the literature for the range of thicknesses which we studied, the PL peak energy distribution shows the unexpected broadening for uncapped samples: for example, deviations from E^{av}_{max} by ±20-30 meV are evident in Fig.5.3(a,b). For the capped samples, new trends are observed: the significant narrowing and

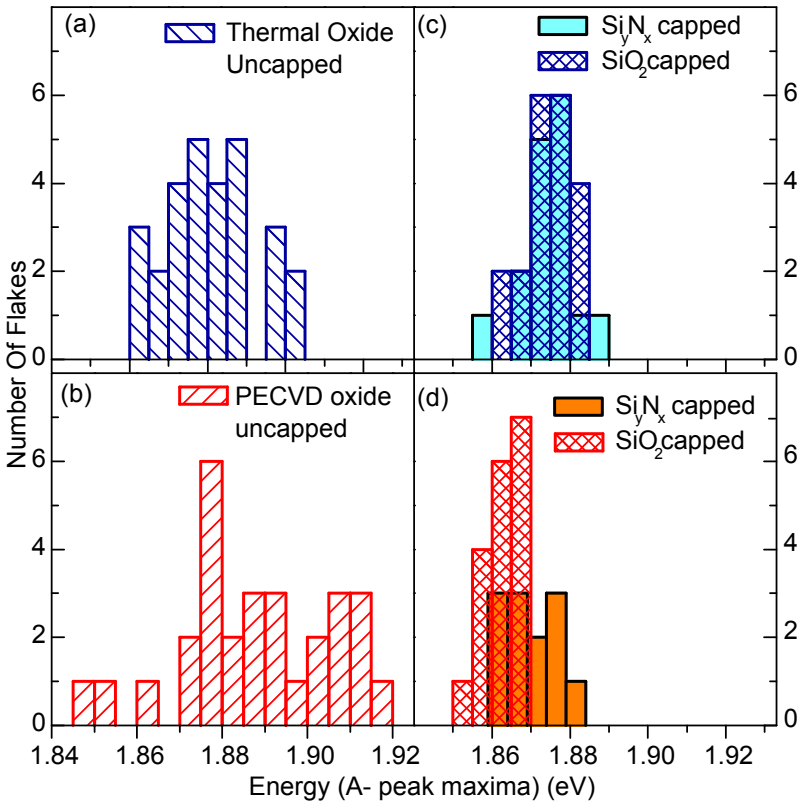

Figure 5.3: (a-d) PL peak energies for A exciton complex in MoS_2 thin films. Data for films deposited on thermally (PECVD) grown SiO_2 substrates are shown in top (bottom) panels. Panels (a)-(b) and (c)-(d) show PL peak positions for uncapped and capped films, respectively.

red-shift of E_{max} distributions. As shown below, these effects reflect changes in the PL lineshapes between the capped and uncapped samples, which in their turn reflect changes in the relative intensities of the A^-, A^0 and L peaks.

A box-plot diagram summarising the above histogram plots is presented in figure 5.4. In this case the centre of the box represents the mean, the box represents the spread of standard deviation and the whiskers represent the true spread of the data. By presenting the data in this way the improved reproducibility

of capped MoS_2 samples becomes clear. It can be seen that the addition of a capping layer also causes a red shift of 10/20 meV.

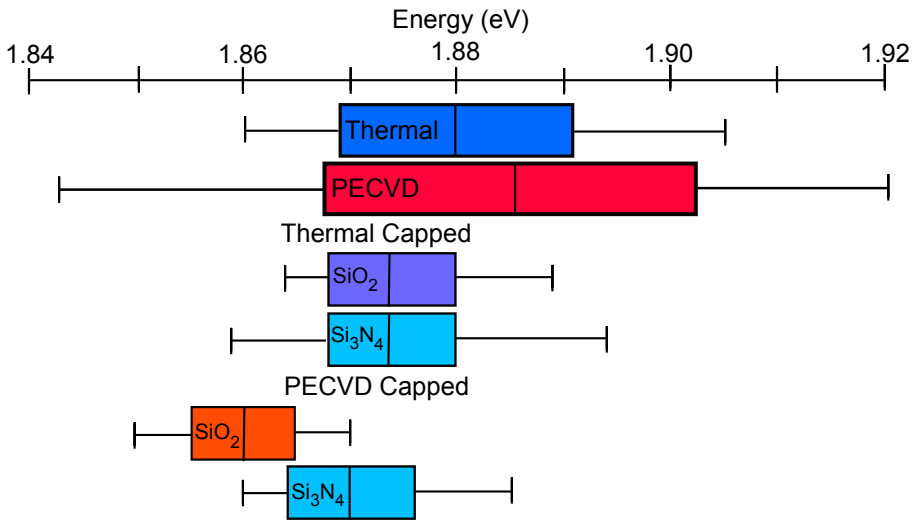

Figure 5.4: A box-plot diagram describing the central A peak emission energy for both capped and uncapped films on PECVD and thermal oxide substrates (as labelled). The central box represents the spread of standard deviation and the extended line and whiskers the true spread of data.

5.3.3 Analysis of spectral linewidth

In this section we will present the linewith analysis for the A exciton PL based on the measurement of full width at half maximum (FWHM) in each PL spectrum. This approach enables us to account for contributions of the three PL features, L, A^0 and A^-. The data are summarized in Fig.5.5 and Tables 5.1.

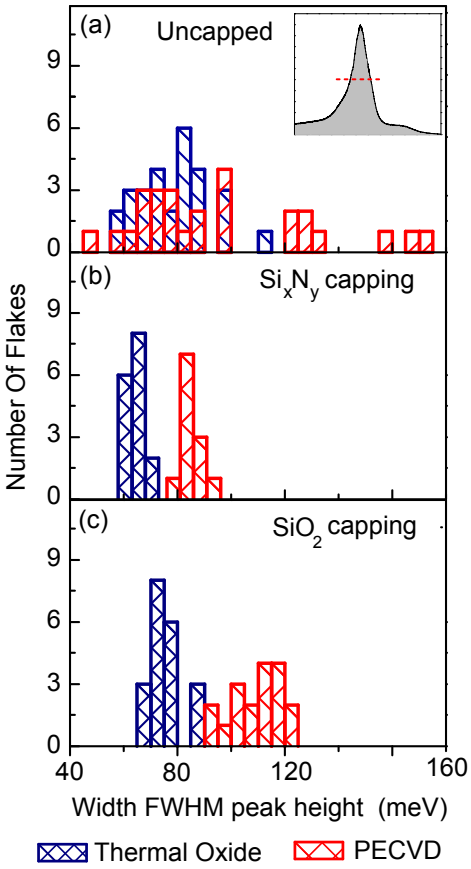

Figure 5.5: PL FWHM of exciton complex A in thin MoS_2 films. Data for MoS_2 films deposited on thermally and PECVD grown SiO_2 substrates is shown with blue and red, respectively. (a) PL FWHM of uncapped MoS_2 films. (b) PL FWHM of Si_xN_y capped MoS_2 films. (c) PL FWHM of SiO_2 capped MoS_2 films.

PECVD grown SiO_2 substrates. These data are presented in Fig.5.5 in red. Data for uncapped films are shown in Fig.5.5(a), from where it is evident that the lineshapes vary dramatically from film to film within a range from 50 to 170 meV. FWHM for uncapped films on PECVD grown substrates is on average ΔE^{av}_{FWHM}=96 with a large standard deviation σ_{FWHM}=33 meV. This gives a rather high coefficient of variation $\sigma_{FWHM}/\Delta E^{av}_{FWHM}$=0.34 showing normalized dispersion of the distribution of the PL FWHM.

The non-uniformity of lineshapes of the PL spectra is significantly suppressed by capping the films with Si_xN_y and SiO_2 (shown with red in Fig.5.5(b) and (c) respectively). This is evidenced from the reduction of the coefficient of variation in the FWHM values by a factor of 4 in capped films compared with the uncapped samples (in Table 5.1). Despite the narrowed spread of ΔE_{FWHM} values, the average FWHM in SiO_2 capped films is rather high, 109 meV, which reflects a relatively strong contribution of L and A^0 PL features. Contributions of A^-, L and A^0 features vary very considerably in the uncapped samples, leading to on average smaller linewidths but a very considerable spread in FWHM values. In contrast, in Si_xN_y capped films, A^- peak dominates and both L and A^0 features are relatively weak, which effectively results in narrowing of PL.

Thermally grown SiO_2 substrates. These data are presented in Fig.5.5 in blue. It can be seen that uncapped films deposited on the flatter thermal oxide substrates appear to have significantly narrower distributions of linewidths compared to uncapped films on PECVD substrates: coefficient of variation of ΔE_{FWHM} is by a factor of 2 smaller for films on the thermally grown substrates [see Fig.5.5(a) and Table 5.1]. In addition, compared with the films deposited on PECVD grown SiO_2, FWHM is also reduced by about 20% to 79 meV. Such

Table 5.1: Mean values, standard deviations and coefficients of variation for full width at half maximum of PL spectra measured for thin MoS_2 films.

Substrate/Capping	Mean value	Standard deviation	Coefficient of variation
PECVD/uncapped	96 meV	33 meV	0.34
PECVD/SiO_2	109 meV	9 meV	0.08
PECVD/Si_xN_y	84 meV	7 meV	0.08
Thermal/uncapped	79 meV	12 meV	0.15
Thermal/SiO_2	76 meV	7 meV	0.09
Thermal/Si_xN_y	64 meV	4 meV	0.06

narrowing reflects weaker contribution of L and A^0 peaks in PL spectra.

The non-uniformity of the PL spectra still present in uncapped films deposited on thermally grown SiO_2 is further suppressed by capping the films with Si_xN_y and SiO_2 [shown with blue in Fig.5.5(b) and (c) respectively]. In general, the coefficients of variation for FWHM of the capped films are rather similar for both substrates and are in the range of 0.06-0.09, showing significant improvement of the reproducibility of PL features compared with the uncapped samples (see Table 5.1). For Si_xN_y capped films on thermally grown SiO_2, we also observe narrowing of PL emission to ΔE^{av}_{FWHM}=64 meV. This reflects further suppression of L and A^0 peaks relative to A^-, the effect less pronounced in SiO_2 capped films.

5.4 UFM & AFM measurements of the mechanical coupling of MoS_2 to Si/SiO_2 substrates

To further understand the interactions between MoS_2 films and the substrate/capping materials, we carried out detailed AFM and UFM measurements of our samples

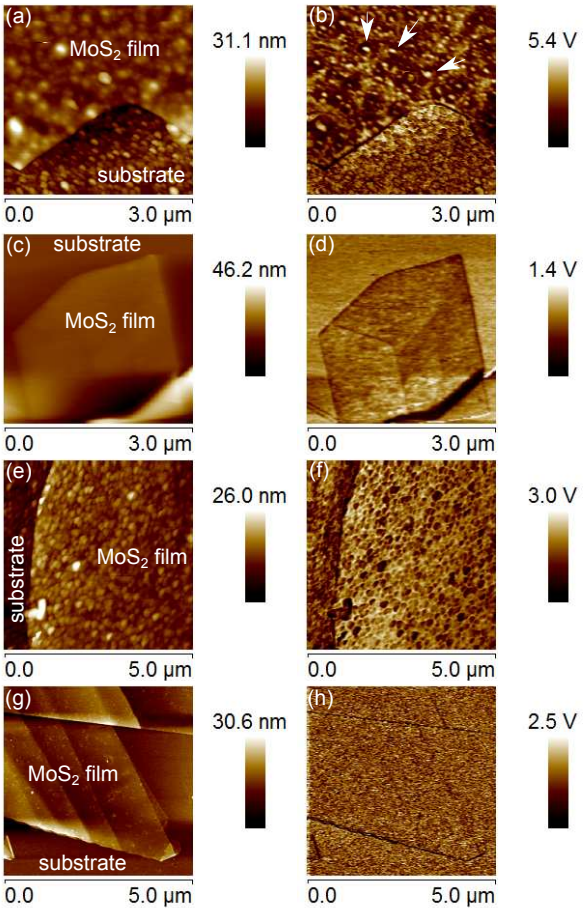

Figure 5.6: AFM (left column) and UFM (right column) images for MoS_2 thin films deposited on PECVD and thermally grown SiO2 substrates. (a,b) PECVD substrate, uncapped MoS_2 film; (c,d) thermally grown substrate, uncapped MoS_2 film; (e,f) PECVD substrate, MoS_2 film capped with 15 nm of SiO_2 grown by PECVD; (g,h) thermally grown substrate, MoS_2 film capped with 15 nm of SiO_2 grown by PECVD.

(Fig.5.6). AFM measurements of films deposited on PECVD grown substrates Fig.5.6(a) show that the film is distorted in shape and follows the morphology of the underlying substrate. The R_{rms} of these films is 1.7 nm with a maximum height R_{max}=11 nm, similar to the parameters of the substrate, R_{rms}=2 nm and R_{max}=15 nm. Such R_{max} is greater than the thickness of films (<3 nm), lead-

ing to significant film distortions. UFM measurements of these films [Fig.5.6(b)] show small areas of higher stiffness (light colour, marked with arrows) and much larger areas of low stiffness (i.e. no contact with the substrate) shown with a dark colour. This shows that the film is largely suspended above the substrate on point contacts.

AFM measurements of films deposited on thermally grown SiO_2 substrates [Fig.5.6(c)] show a much more uniform film surface due to the less rough underlying substrate. This is reflected in a significantly improved R_{rms} = 0.3 nm and R_{max}=1.8 nm. These values are still higher than those for the bare substrate with R_{rms} = 0.09 nm and R_{max}=0.68 nm. A more uniform stiffness distribution is observed for these films in UFM [Fig.5.6(d)], although the darker colour of the film demonstrates that it is much softer than the surrounding substrate and thus still has relatively poor contact with the substrate. A darker shading at film edges demonstrates that they have poorer contact than the film center and effectively curl away from the substrate.

AFM and UFM data for films capped with 15 nm SiO_2 after deposition on PECVD and thermally grown SiO_2 are given in Fig.5.6(e, f) and (g, h) respectively. For the PECVD substrate, the roughness of the MoS_2 film is similar to that in the uncapped sample in Fig.5.6(a): R_{rms}=1.68 nm and R_{max}=10.2 nm. From the UFM data in Fig.5.6(f), it is evident that although the contact of the MoS_2 film with the surrounding SiO_2 is greatly improved compared with the uncapped films, a large degree of non-uniformity is still present, as concluded from many dark spots on the UFM image. In great contrast to that, the capped MoS_2 film on thermally grown SiO_2 is flatter [Fig.5.6(g, h)], R_{rms}=0.42 nm and R_{max}=6.1 nm, with the roughness most likely originating from the PECVD grown SiO_2 capping

layer. The UFM image in Fig.5.6(h) shows remarkable uniformity of the stiffness of the film similar to that of the capped substrate, demonstrating uniform and firm contact (i.e. improved mechanical coupling) between the MoS_2 film and the surrounding dielectrics.

5.5 Discussion & Interpretation

There is a marked correlation between the PL properties of the MoS_2 films and film stiffness measured by UFM. The stiffness reflects the strength of the mechanical coupling between the adjacent monolayers of the MoS_2 film and the surrounding dielectrics. The increased bonding and its uniformity for films deposited on less rough thermally grown SiO_2 substrates and for capped MoS_2 films manifests in the more reproducible PL characteristics, leading to reduced standard deviations of the peak positions and linewidths. These spectral characteristics are influenced by the relative intensities of the three dominating PL features, trion A^-, neutral exciton A^0 and low energy L peak, which are influenced by the charge balance in the MoS_2 films sensitive to the dielectric environment. The efficiency of charging can be qualitatively estimated from the relative intensities of A^- and A^0 peaks. In the vast majority of the films, A^- dominates. As noted above, the intensity of A^0 directly correlates (qualitatively) with that of the relatively broad low energy PL shoulder L (see Fig.5.1 and 5.2), previously ascribed to emission from surface states. The lineshape analysis presented in Fig.5.5 and Table 5.1 is particularly sensitive to the contribution of peak L.

The PL lineshape analysis and comparison with the UFM data lead to the conclusion that negative charging of the MoS_2 films is relatively inefficient for partly suspended uncapped films on rough PECVD substrates. Both in SiO_2 and Si_xN_y capped films on PECVD substrates, the charging effects are more pronounced. However, both A^0 and L features still have rather high intensities. The relatively low charging efficiency is most likely related to a non-uniform bonding between the MoS_2 films and the surrounding dielectric layers as concluded from

the UFM data [see Fig.5.6(f)]. The charging is more pronounced for uncapped MoS_2 films on thermal oxide substrates, and is enhanced significantly more for capped films: for Si_xN_y capping A^0 and L peaks only appear as weak shoulders in PL spectra.

It is clear from this analysis that the charge balance in the MoS_2 films is altered strongly when the films are brought in close and uniform contact with the surrounding dielectrics, enabling efficient transfer of charge in a monolithic hybrid heterostructure. Both n-type(19, 79, 149) and p-type (148, 149) conductivities have been reported in thin MoS_2 films deposited on SiO_2. It is thus possible that the sign and density of charges in exfoliated MoS_2 films may be strongly affected by the properties of PECVD grown SiO_2 and Si_xN_y, where the electronic properties may vary depending on the growth conditions (154, 155). It is notable, however, that for a large variety of samples studied in this work, the negative charge accumulation in the MoS_2 films is pronounced and is further enhanced when the bonding of the films with the dielectric layers is improved. Additional charges in MoS_2 may occur due to intrinsic impurities as previously discussed.

The band-structure of MoS_2 and hence its optical characteristics can also be influenced by strain (100, 144, 145). The distribution and magnitude of strain cannot be assessed directly in our experiments. Indirect evidence for increased tensile strain in capped samples compared to uncapped films on PECVD may be deduced from the red-shift of the average PL peak energy by up to 30 meV after capping (data in Fig.5.3). On the other hand, doping-dependent Stokes shifts of the trion PL have been found recently (85), which may explain the behaviour we find in charged MoS_2 sheets. One would expect a more uniform strain distribution in the case of uniform mechanical properties of the sample, which as shown by

UFM is achieved for capped MoS_2 films on flat thermally grown SiO_2 substrates.

5.6 Summary of results

In this chapter we demonstrate that it is possible to increase the reproducibility of optical characteristics of mechanically exfoliated few mono-layer MoS_2 films by coating the films with additional dielectric layers of either SiO_2 or Si_xN_y. By comparing PL data with results obtained in UFM, we show that there is a direct correlation between the degree of the mechanical coupling of the MoS_2 films to the surrounding dielectrics and uniformity of the optical properties. We show that a wide spread in PL spectral lineshapes occurs in general as a result of the film-to-film variation of the relative intensities of the negatively charged trion peak A^- and the two other features, neutral exciton peak A^0 and a low energy PL band L. We find that when the mechanical coupling between the films and the dielectrics is improved, the films become increasingly negatively charged, as deduced from the pronounced increase in PL of the trion peak, dominating in the majority of PL spectra. Such charging, and also possibly reduction in strain non-uniformities, underpins the highly uniform PL properties in capped MoS_2 films, leading to the smallest linewidths below 70 meV for thin MoS_2 films deposited on thermally grown SiO_2 and capped with a Si_xN_y layer.

Chapter 6

Conclusions

In this thesis three main topics covered were (i) the effect of a GaAsP shell on the optical properties of self-catalyzed GaAs nanowires grown on silicon, (ii) the exfoliation, characterisation and optical measurements of MoS_2, and (iii) optical investigations of the natural doping of a few monolayer MoS_2 films deposited on dielectric substrates. The key results for each topic were the following:

(i) In Chapter 3 structural and optical properties of core-shell GaAs/GaAsP and uncapped GaAs nanowires grown on Si substrates, using a catalyst-free MBE technique, are studied in detail. We find that while our uncapped GaAs NWs have a relatively small PL yield which is quenched with increasing temperature, the core-shell GaAs/GaAsP NWs have a PL yield exceeding 2000x the uncapped NWs and also emit brightly up to room temperature. We attribute this enhancement to the effect of the NW surface, specifically the competition between optical recombination in the NW length and non-radiative surface states. We suggest that the capping layer reduces the efficiency of non-radiative surface paths and we show that the thermalisation efficiency for non-radiative paths is approximately 8 times less in the GaAs/GaAsP sample. We find that additional surface states, further quenching PL, form on uncapped NWs which are exposed to air and

we attribute these to oxidation of the surface. This process can be reversed by washing the samples in NH_3.

We demonstrate a second PL quenching mechanism at high temperature in capped NWs which we attribute to electrons escaping from the GaAs core into the GaAsP shell. The addition of GaAsP is shown to result in strain imparted on the core NW, which is evident due to a blue shift of PL above the band gap of zinc blende GaAs as well as a relatively broad distribution due to inhomogeneous strain. The ability to tune the absorption energy of NWs by capping has potential application in photovoltaics.

Additionally, to surface effects and strain, we find that crystalline structure of the NWs also play an important role in determining optical properties. In particular we demonstrate type II spacial confinement of electrons and holes between different crystal polytypes of WZ and ZB. This is concluded from relatively long lifetimes measured and also a shift in emission energy below the value for GaAs ZB, which reflects a previously accepted 115meV band offset between GaAs WZ and ZB. The PL lifetime measured is 7.4ns for type-II confinement in uncapped GaAs NWs and 1.45ns for type-I recombination in the high quality pure ZB GaAs/GaAsP NWs.

(ii) In chapter 4 development of fabrication procedures for thin sheets of MoS_2 is presented, which has since been adapted for exfoliation of GaSe, GaS, GaTe and $MoSe_2$ opening a new field of 2D materials. We investigate in detail the morphology of MoS_2 sheets produced this way which we deposited on Si/SiO_2 substrates and we show detailed images of typical defects which break the periodicity of the lattice, which are likely to affect mobilities and optical properties of thin sheets.

We find that MoS_2 sheets under 5 monolayer in thickness produced by our method are bright emitters of light. The signal is composed of peaks A and B originating from a split valence band. The A band is composed of recombination of a neutral and a charged exciton, A^0 and A^-, and a shoulder L which may be related to surface bound impurities. We find that the relative intensity of these states varies between different MoS_2 sheets.

Although we do not measure non-radiative processes directly, we find indirect evidence that they are significant in determining the optical behaviour of MoS_2. We find that temperature dependence of the PL yield is weak. We suggest that this is due to the dominance of non-radiative and indirect processes at low temperatures which means that thermally activated non-radiative paths have less noticeable effect. We also find that, with increasing laser pumping power, the relative intensity of the L band changes. This is also likely related to competition between non-radiative and radiative recombination. A low quantum efficiency of MoS_2 means that non-radiative processes have a high rate, which is reflected by the intensity of PL not saturating with laser pumping power, even at high powers.

We also provide preliminary evidence of the effects of charge transfer between MoS_2 and the SiO_2 substrate, an effect we investigate in greater detail in Chapter 5. We show that the MoS_2 spectrum is dominated by emission from a negative exciton, A^-. We find that, with increasing temperature, the relative intensity of PL emission from neutral exciton A^0 reduces and eventually disappears. We suggest that this is due to the MoS_2 film capturing charges which can thermally activated in the SiO_2 substrate or the MoS_2. We find that the emission of L is also similarly effected by temperature and we suggest that these states are also

sensitive to charge.

We also find that the addition of a capping layer reduces scattering in the fitting parameters for the Varshni dependency of the bandgap with increasing temperature, between different MoS_2 samples. In Chapter 5 we continue work on capped MoS_2 and also MoS_2 on substrates with different roughness. We find that the effects of charging and also strain, as introduced in this chapter, heavily influence optical properties through contact with the substrate. Here we demonstrate that the addition of a capping layer can increases the uniformity of emission properties between different MoS_2 sheets due to increased mechanical bonding with the substrate.

(iii) In Chapter 5 we demonstrate that it is possible to increase the reproducibility of optical characteristics of mechanically exfoliated few mono-layer MoS_2 films by coating the films with additional dielectric layers of either SiO_2 or Si_xN_y. By comparing PL data with results obtained in UFM, we show that there is a direct correlation between the degree of the mechanical coupling of the MoS_2 films to the surrounding dielectrics and uniformity of the optical properties. We show that a wide spread in PL spectral lineshapes occurs in general as a result of the film-to-film variation of the relative intensities of the negatively charged trion peak A^- and the two other features, neutral exciton peak A^0 and a low energy PL band L. We find that when the mechanical coupling between the films and the dielectrics is improved, the films become increasingly negatively charged, as deduced from the pronounced increase in PL of the trion peak, dominating in the majority of PL spectra. Such charging, and also possibly reduction in strain non-uniformities, underpins the highly uniform PL properties in capped MoS_2 films, leading to the smallest linewidths below 70 meV for thin MoS_2 films deposited

on thermally grown SiO_2 and capped with a Si_xN_y layer.

In summary; the optical properties of two photon emitting materials are studied. By understanding the effect of environment and structure, the emission properties could be optimised. These materials have potential for integration into Si and Graphene based electronics.

References

[1] M. Tanenbaum. Silicon n-p-n grown junction transistors. *Proceedings of the IRE*, 26(9):1986–2000, 1955. 1

[2] W.A. Adcock, M.E. Jones, J.W. Thornhill, and E.D. Jackson. Silicon transistor. *Proceedings of the IRE*, 42(7):1192, 1954. 1

[3] S. Amos. *Principles of Transistor Circuits, Ninth Edition: Introduction to the Design of Amplifiers, Receivers and Digital Circuits*. Newnes, 2000. 1, 18

[4] S.A. Wolf, D.D. Awschalom, R.A. Buhrman, J.M. Daughton, S. Von Molnar, M.L. Roukes, A. Yu Chtchelkanova, and D.M. Treger. Spintronics: A spin-based electronics vision for the future. *Science*, 294(5546):1488–1495, 2001. 1, 56

[5] R Menzel. *Photonics: Linear and Nonlinear Interactions of Laser Light and Matter*. Springer, 2001. 1

[6] T. M. Godden, J. H. Quilter, A. J. Ramsay, Yanwen Wu, P. Brereton, S. J. Boyle, I. J. Luxmoore, J. Puebla-Nunez, A. M. Fox, and M. S. Skolnick. Coherent optical control of the spin of a single hole in an

InAs/GaAs quantum dot. *Phys. Rev. Lett.*, 108:017402, Jan 2012. URL http://link.aps.org/doi/10.1103/PhysRevLett.108.017402. 1

[7] C. Bennett, E. Bernstein, G. Brassard, and U. Vazirani. Strengths and weaknesses of quantum computing. *SIAM Journal on Computing*, 26(5): 1510–1523, 1997. doi: 10.1137/S0097539796300933. URL http://epubs.siam.org/doi/abs/10.1137/S0097539796300933. 1

[8] F. Schwierz. Graphene transistors. *Nature nanotechnology*, 5(7):487–96, July 2010. ISSN 1748-3395. doi: 10.1038/nnano.2010.89. URL http://www.ncbi.nlm.nih.gov/pubmed/20512128. 1, 14, 17, 104, 105

[9] K. Peng, Y. Xu, Y. Wu, Y. Yan, S.T. Lee, and J. Zhu. Aligned single-crystalline Si nanowire arrays for photovoltaic applications. *Small*, 1(11): 1062–1067, 2005. 1, 3, 5

[10] M.D. Kelzenberg, B.M. Turner-Evans, D.B. Kayes, M.A. Filler, M.C. Putnam, N.S. Lewis, and H.A. Atwater. Photovoltaic measurements in single-nanowire silicon solar cells. *Nano Letters*, 8(2):710–714, 2008. 1, 5

[11] M.G. Thomas, H.N. Post, and R. Deblasio. Photovoltaic systems: an end-of-millennium review. *Progress in Photovoltaics: Research and Applications*, 7(1):1–19, 1999. 1

[12] S.M Sze and K. Ng Kwok. *Physics Of Semiconductor Devices*. Whiley-Interscience, 2007. 1, 3, 16, 17, 27

[13] N.N. Ledentsov, V.M. Ustinov, V.A. Shchukin, P.S. Kopev, Zh I. Alferov,

and D. Bimberg. Quantum dot heterostructures: Fabrication, properties, lasers (review). *Semiconductors*, 32(4):343–365, 1998. 1

[14] A. Imamog, D. Awschalom, G. Burkard, D.P. DiVincenzo, D. Loss, M. Sherwin, and A. Small. Quantum information processing using quantum dot spins and cavity QED. *Physical Review Letters*, 83(20):4204, 1999. 1

[15] M.A. Zimmler, F. Capasso, S. Müller, and C. Ronning. Optically pumped nanowire lasers: invited review. *Semiconductor Science and Technology*, 25 (2):024001, 2010. 1

[16] M. Dhingra, A. Shankar, and B.B. Tiwari. A review on quantum well structures in photonic devices for enhanced speed and span of the transmission network. *Indian Journal of Physics*, 84(8):1031–1037, 2010. 1

[17] D.A.B. Miller. Quantum well optoelectronic switching devices. *International Journal of High Speed Electronics and Systems*, 1(01):19–46, 1990. 1

[18] P.B. Mirkarimi, K.F. McCarty, and D.L. Medlin. Review of advances in cubic boron nitride film synthesis. *Materials Science and Engineering: R: Reports*, 21(2):47–100, 1997. 1

[19] K. Mak, C. Lee, J. Hone, J. Shan, and T. Heinz. Atomically Thin MoS_2: A New Direct-Gap Semiconductor. *Physical Review Letters*, 105(13):2–5, September 2010. ISSN 0031-9007. doi: 10.1103/PhysRevLett.105.136805. URL http://link.aps.org/doi/10.1103/PhysRevLett.105.136805. 2, 14, 20, 21, 23, 69, 70, 78, 85, 104, 111, 121

[20] A. Splendiani, L. Sun, Y. Zhang, T. Li, J. Kim, C.Y. Chim, G. Galli, and F. Wang. Emerging photoluminescence in monolayer MoS_2. *Nano Letters*, 10(4):1271–5, April 2010. ISSN 1530-6992. doi: 10.1021/nl903868w. URL http://www.ncbi.nlm.nih.gov/pubmed/20229981. xii, 2, 14, 19, 20, 21, 23, 69, 70, 78, 89, 109

[21] Y. Li, F. Qian, J. Xiang, and C.M. Lieber. Nanowire electronic and optoelectronic devices. *Materials Today*, 9(10):18–27, 2006. 3

[22] H.J. Joyce, Q. Gao, H. Hoe Tan, C. Jagadish, Y. Kim, J. Zou, L.M. Smith, H.E. Jackson, J.M. Yarrison-Rice, P. Parkinson, and M.B. Johnston. III-V semiconductor nanowires for optoelectronic device applications. *Progress in Quantum Electronics*, 35(2-3):23–75, March 2011. ISSN 00796727. doi: 10.1016/j.pquantelec.2011.03.002. URL http://linkinghub.elsevier.com/retrieve/pii/S0079672711000036. 3, 4, 5, 7, 9, 11, 39, 47

[23] M.T. Borgstrom and J. Wallentin. Nanowires with promise for photovoltaics. *Selected Topics in Quantum Electronics*, 17(4):1050–1061, 2011. URL http://ieeexplore.ieee.org/xpls/abs_all.jsp?arnumber=5613139. 3, 5, 11

[24] T.J. Kempa, R. W Day, S.K. Kim, H.G. Park, and C.M. Lieber. Semiconductor nanowires: a platform for exploring limits and concepts for nano-enabled solar cells. *Energy & Environmental Science*, 2013. 3

[25] A.M. Fox. *Optical Properties of Solids*. Oxford Master Series, 2001. 3, 4, 27, 28, 61

[26] M. Grundmann. *The Physics Of Semiconductors*. Springer, Condensed Matter Series, 2010. 3, 27, 61, 91

[27] S. Perkowitz. *Optical characterization of semiconductors : infrared, Raman and photoluminescence spectroscopy*. Academic Press, 1993. 3, 26, 28

[28] R.F. Davis. III-V nitrides for electronic and optoelectronic applications. *Proceedings of the IEEE*, 79(5):702–712, 1991. 3

[29] D.L Mathine. The integration of III-V optoelectronics with silicon circuitry. *Selected Topics in Quantum Electronics*, 3(3):952–959, 1997. 3

[30] O. Hayden, A.B. Greytak, and D.C. Bell. Core-shell nanowire light-emitting diodes. *Advanced Materials*, 17(6):701–704, March 2005. ISSN 0935-9648. doi: 10.1002/adma.200401235. URL http://doi.wiley.com/10.1002/adma.200401235. 3, 39

[31] C. Patrik T. Svensson, T.s Mårtensson, J. Trägårdh, C. Larsson, M. Rask, D. Hessman, L. Samuelson, and J.s Ohlsson. Monolithic GaAs/InGaP nanowire light emitting diodes on silicon. *Nanotechnology*, 19(30):305201, 2008. 3, 39

[32] C.G. Fast. Single-nanowire electrically driven lasers. *Nature*, 421(January): 241–245, 2003. doi: 10.1038/nature01289.1. 3

[33] G. Chen, Z. Liu, B. Liang, G. Yu, Z. Xie, H. Huang, B. Liu, X. Wang, D. Chen, M.Q. Zhu, and G. Shen. Single-crystalline p-type Zn_3As_2 nanowires for field-effect transistors and visible-light photodetectors on rigid

and flexible substrates. *Advanced Functional Materials*, 2012. ISSN 1616-3028. doi: 10.1002/adfm.201202739. URL http://dx.doi.org/10.1002/adfm.201202739. 3

[34] M.T. Björk, C. Thelander, A.E. Hansen, L.E. Jensen, M.W. Larsson, L.R. Wallenberg, and L. Samuelson. Few-electron quantum dots in nanowires. *Nano Letters*, 4(9):1621–1625, 2004. 4

[35] M.T. Björk, A. Fuhrer, A.E. Hansen, M.W. Larsson, L.E. Fröberg, and L. Samuelson. Tunable effective g factor in InAs nanowire quantum dots. *Physical Review B*, 72(20):201307, 2005. 4, 7

[36] M.T. Borgström, V. Zwiller, E. Müller, and A. Imamoglu. Optically bright quantum dots in single nanowires. *Nano Letters*, 5(7):1439–1443, 2005. 4, 7, 39

[37] R.L. Havil and A.K Walton. *Elements Of Electronics for Physical Scientists*. Macmillan, 1980. 4, 16

[38] T. Mårtensson and C.P.T. Svensson. Epitaxial III-V nanowires on silicon. *Nano Letters*, (111), 2004. URL http://pubs.acs.org/doi/abs/10.1021/nl0487267. 4, 6, 7

[39] R. Fischer, D. Neuman, H. Zabel, H. Morkoc, C. Choi, and N. Otsuka. Dislocation reduction in epitaxial GaAs on Si(100). *Applied physics letters*, 48(18):1223–1225, 1986. 4

[40] P. Sheldon, K.M. Jones, M.M. Al-Jassim, and B.G. Yacobi. Dislocation density reduction through annihilation in lattice-mismatched semiconduc-

tors grown by molecular-beam epitaxy. *Journal of Applied Physics*, 63(11): 5609–5611, 1988. 4

[41] H. Park, A.W. Fang, S. Kodama, and J.E. Bowers. Hybrid silicon evanescent laser fabricated with a silicon waveguide and III-V offset quantum well. *Optical Society of America*, 2005. 4

[42] R.R. LaPierre, A.C.E. Chia, S.J. Gibson, C.M. Haapamaki, J. Boulanger, R. Yee, P. Kuyanov, J. Zhang, N. Tajik, and N. Jewell. III-V nanowire photovoltaics: Review of design for high efficiency. *Physica Status Solidi (RRL)-Rapid Research Letters*, 2013. 4, 7

[43] L.L. Kazmerski. Photovoltaics: A review of cell and module technologies. *Renewable and Sustainable Energy Reviews*, 1(1):71–170, 1997. 4, 5, 38

[44] D.M. Callahan, J.N. Munday, and H.A. Atwater. Solar cell light trapping beyond the ray optic limit. *Nano Letters*, 12(1):214–218, 2012. 4, 38

[45] A.C. Hamilton and J. Courtial. Metamaterials for light rays: ray optics without wave-optical analog in the ray-optics limit. *New Journal of Physics*, 11(1):013042, 2009. 4, 38, 39

[46] J. Wallentin, N. Anttu, D. Asoli, M. Huffman, I. Åberg, M.H. Magnusson, G. Siefer, P. Fuss-Kailuweit, F. Dimroth, and B. Witzigmann. InP nanowire array solar cells achieving 13.8% efficiency by exceeding the ray optics limit. *Science*, 339(6123):1057–1060, 2013. 5, 38

[47] T.B. Hoang, A.F. Moses, H.L. Zhou, D.L. Dheeraj, B.O. Fimland, and H. Weman. Observation of free exciton photoluminescence emission from

single wurtzite GaAs nanowires. *Applied Physics Letters*, 94(13):133105, 2009. ISSN 00036951. doi: 10.1063/1.3104853. URL http://link.aip.org/link/APPLAB/v94/i13/p133105/s1&Agg=doi. 5, 8, 9, 52

[48] P. Krogstrup, M. Hannibal Madsen, W. Hu, M. Kozu, Y. Nakata, J. Nygard, M. Takahasi, and R. Feidenhansl. In-situ x-ray characterization of wurtzite formation in GaAs nanowires. *Applied Physics Letters*, 100(9):093103, 2012. ISSN 00036951. doi: 10.1063/1.3688489. URL http://link.aip.org/link/APPLAB/v100/i9/p093103/s1&Agg=doi. 5, 8

[49] R.S. Wagner and W.C. Ellis. Vapor-liquid-solid mechanism of single crystal growth. *Applied Physics Letters*, 4(5):89–90, 1964. 5

[50] Z.H. Wu, X.Y. Mei, D. Kim, M. Blumin, and H.E. Ruda. Growth of Au-catalyzed ordered GaAs nanowire arrays by molecular-beam epitaxy. *Applied Physics Letters*, 81(27):5177–5179, 2002. 6, 7

[51] K.A. Dick, C. Thelander, L. Samuelson, and P. Caroff. Crystal phase engineering in single InAs nanowires. *Nano Letters*, 10(9):3494–3499, 2010. 7

[52] T. Martensson, J.B. Wagner, E. Hilner, a. Mikkelsen, C. Thelander, J. Stangl, B.J. Ohlsson, A. Gustafsson, E. Lundgren, L. Samuelson, and W. Seifert. Epitaxial growth of InAs nanowires on silicon using nucleation templates formed by self-assembled organic coatings. *Advanced Materials*, 19(14):1801–1806, July 2007. ISSN 09359648. doi: 10.1002/adma.200700285. URL http://doi.wiley.com/10.1002/adma.200700285. 7

[53] B. Mandl, J. Stangl, T. Må rtensson, A. Mikkelsen, J. Eriksson, L.S. Karlsson, G.U.M Bauer, L. Samuelson, and W. Seifert. Au-free epitaxial growth of InAs nanowires. *Nano Letters*, 6(8):1817–21, August 2006. ISSN 1530-6984. doi: 10.1021/nl060452v. URL http://www.ncbi.nlm.nih.gov/pubmed/16895379. 7

[54] B. Hua, J. Motohisa, Y. Kobayashi, S. Hara, and T. Fukui. Single GaAs/GaAsP coaxial core-shell nanowire lasers. *Nano Letters*, 9(1):112–6, January 2009. ISSN 1530-6984. doi: 10.1021/nl802636b. URL http://www.ncbi.nlm.nih.gov/pubmed/19072060. 7, 10, 57, 58

[55] P. Krogstrup, R. Popovitz-Biro, E. Johnson, M.H. Madsen, J. Nygaard, and H. Shtrikman. Structural phase control in self-catalyzed growth of GaAs nanowires on silicon(111). *Nano Letters*, 10(11):4475–82, November 2010. ISSN 1530-6992. doi: 10.1021/nl102308k. URL http://www.ncbi.nlm.nih.gov/pubmed/20932012. 7, 8, 11, 39, 45

[56] S. Plissard, K. A. Dick, G. Larrieu, S.E. Godey, A. Addad, X. Wallart, and P. Caroff. Gold-free growth of GaAs nanowires on silicon: arrays and polytypism. *Nanotechnology*, 21(38):385602, September 2010. ISSN 1361-6528. doi: 10.1088/0957-4484/21/38/385602. URL http://www.ncbi.nlm.nih.gov/pubmed/20798467. 8, 9, 11, 39, 45

[57] A.F. Morral. Gold-free GaAs nanowire synthesis and optical properties. *Selected Topics in Quantum Electronics, IEEE Journal of*, 17(4):819–828, 2011. 8, 11

[58] O. D. D. Couto, D. Sercombe, J. Puebla, L. Otubo, I. J. Luxmoore, M. Sich,

T. J. Elliott, E. A. Chekhovich, L. R. Wilson, M. S. Skolnick, H. Y. Liu, and A. I. Tartakovskii. Effect of a GaAsP shell on the optical properties of self-catalyzed gaas nanowires grown on silicon. *Nano Letters*, 12(10): 5269–5274, 2012. doi: 10.1021/nl302490y. URL http://pubs.acs.org/doi/abs/10.1021/nl302490y. 8, 31, 39, 43, 56

[59] P. Avouris. Carbon-based electronics. *Nature*, pages 605–615, 2007. URL http://usrexp-sandbox.nature.com/nnano/journal/v2/n10/full/nnano.2007.300.html. 9, 19, 50, 51, 105

[60] M. Heiss, S. Conesa-Boj, J. Ren, H.H. Tseng, A. Gali, A. Rudolph, E. Uccelli, F. Peiro, J. Morante, D. Schuh, E. Reiger, E. Kaxiras, J. Arbiol, and A. Fontcuberta. Direct correlation of crystal structure and optical properties in wurtzite/zinc-blende GaAs nanowire heterostructures. *Physical Review B*, 83(4):1–10, January 2011. ISSN 1098-0121. doi: 10.1103/PhysRevB.83.045303. URL http://link.aps.org/doi/10.1103/PhysRevB.83.045303. 9, 39, 47, 52

[61] D. Spirkoska, J. Arbiol, A. Gustafsson, S. Conesa-Boj, F. Glas, I. Zardo, M. Heigoldt, M. H. Gass, A. L. Bleloch, S. Estrade, M. Kaniber, J. Rossler, F. Peiro, J.R. Morante, G. Abstreiter, L. Samuelson, and A. Fontcuberta I Morral. Structural and optical properties of high quality zinc-blende/wurtzite GaAs nanowire heterostructures. *Physical Review B*, 80 (24):1–9, December 2009. ISSN 1098-0121. doi: 10.1103/PhysRevB.80.245325. URL http://link.aps.org/doi/10.1103/PhysRevB.80.245325. 9, 39, 52

[62] N. Akopian, G. Patriarche, L. Liu, J.C. Harmand, and V. Zwiller. Crystal phase quantum dots. *Nano Letters*, 10(4):1198–201, April 2010. ISSN 1530-6992. doi: 10.1021/nl903534n. URL http://www.ncbi.nlm.nih.gov/pubmed/20205446. 9, 39, 52

[63] D.I. Wang, Y.L. Chang, Q. Wang, J. Cao, D.B. Farmer, R.G. Gordon, and H. Dai. Surface chemistry and electrical properties of germanium nanowires. *Journal of the American Chemical Society*, 126(37):11602–11, September 2004. ISSN 0002-7863. doi: 10.1021/ja047435x. URL http://www.ncbi.nlm.nih.gov/pubmed/15366907. 10, 39

[64] L. Zhang, J.W. Luo, A. Zunger, N. Akopian, V. Zwiller, and J.C. Harmand. Wide InP nanowires with wurtzite/zincblende superlattice segments are type-II whereas narrower nanowires become type-I: an atomistic pseudopotential calculation. *Nano Letters*, 10(10):4055–60, October 2010. ISSN 1530-6992. doi: 10.1021/nl102109s. URL http://www.ncbi.nlm.nih.gov/pubmed/20809611. 10, 52, 58

[65] O. Demichel, M. Heiss, J. Bleuse, H. Mariette, and A. Fontcuberta i Morral. Impact of surfaces on the optical properties of GaAs nanowires. *Applied Physics Letters*, 97(20):201907, 2010. ISSN 00036951. doi: 10.1063/1.3519980. URL http://link.aip.org/link/APPLAB/v97/i20/p201907/s1&Agg=doi. 10, 40, 58, 65

[66] R. Beaudry, S.P. Watkins, X. Xu, and P. Yeo. Photoreflectance study of phosphorus passivation of GaAs(001). *Journal of Applied Physics*, 87(11):

7838, 2000. ISSN 00218979. doi: 10.1063/1.373463. URL http://link.aip.org/link/JAPIAU/v87/i11/p7838/s1&Agg=doi. 10, 11, 40, 41, 65

[67] P. K. Mohseni, a. D. Rodrigues, J. C. Galzerani, Y. a. Pusep, and R. R. LaPierre. Structural and optical analysis of GaAsP/GaP core-shell nanowires. *Journal of Applied Physics*, 106(12):124306, 2009. ISSN 00218979. doi: 10.1063/1.3269724. URL http://link.aip.org/link/JAPIAU/v106/i12/p124306/s1&Agg=doi. 10, 11, 40, 57, 58, 61, 65

[68] P. L. Gourley and R. M. Biefeld. Quantum size effects in GaAs/$GaAs_xP_{1x}$ strained-layer superlattices. *Applied Physics Letters*, 45(7):749, 1984. ISSN 00036951. doi: 10.1063/1.95385. URL http://link.aip.org/link/APPLAB/v45/i7/p749/s1&Agg=doi. 11

[69] M. Montazeri, M. Fickenscher, L. M Smith, H.E. Jackson, J. Yarrison-Rice, J.H. Kang, Q. Gao, H.H. Tan, C. Jagadish, Y. Guo, J. Zou, M.E. Pistol, and C.E. Pryor. Direct measure of strain and electronic structure in GaAs/GaP core-shell nanowires. *Nano Letters*, 10(3):880–6, March 2010. ISSN 1530-6992. doi: 10.1021/nl903547r. URL http://www.ncbi.nlm.nih.gov/pubmed/20131863. 11, 55, 65

[70] L.J. Lauhon, M.S. Gudiksen, D. Wang, and C.M. Lieber. Epitaxial core-shell and core-multishell nanowire heterostructures. *Nature*, 420(6911):57–61, November 2002. ISSN 0028-0836. doi: 10.1038/nature01141. URL http://www.ncbi.nlm.nih.gov/pubmed/12422212. 11

[71] K.S. Novoselov, A.K. Geim, S.V. Morozov, D. Jiang, Y. Zhang, S.V. Dubonos, I.V. Grigorieva, and A.A. Firsov. Electric field effect in atom-

ically thin carbon films. *Science (New York, N.Y.)*, 306(5696):666–9, October 2004. ISSN 1095-9203. doi: 10.1126/science.1102896. URL http://www.ncbi.nlm.nih.gov/pubmed/15499015. 14

[72] Yandong Ma, Ying Dai, Meng Guo, Chengwang Niu, Jibao Lu, and Baibiao Huang. Electronic and magnetic properties of perfect, vacancy-doped, and nonmetal adsorbed $MoSe_2$, $MoTe_2$ and WS_2 monolayers. *Physical Chemistry Chemical Physics*, 13(34):15546–15553, 2011. 14

[73] H.R. Gutiérrez, N. Perea-López, A.L. Elías, A. Berkdemir, B. Wang, R. Lv, F. López-Urías, V.H. Crespi, H. Terrones, and M. Terrones. Extraordinary room-temperature photoluminescence in WS_2 monolayers. *arXiv preprint arXiv:1208.1325*, 2012. 14

[74] C. Jin, F. Lin, K. Suenaga, and S. Iijima. Fabrication of a freestanding boron nitride single layer and its defect assignments. *Physical Review Letters*, 102(19):195505, 2009. 14

[75] G. Eda, T. Fujita, H. Yamaguchi, D. Voiry, M. Chen, and M. Chhowalla. Coherent atomic and electronic heterostructures of single-layer MoS_2. *ACS Nano*, 6(8):7311–7317, 2012. 14, 103

[76] W. Zhang, C.P. Chuu, J.K. Huang, C.H. Chen, M.L. Tsai, Y.H. Chang, C.T. Liang, H. He Jr, M.Y. Chou, and L.J. Li. Ultrahigh-gain phototransistors based on graphene-MoS_2 heterostructures. *arXiv preprint arXiv:1302.1230*, 2013. 14, 103

[77] S. Bertolazzi, D. Krasnozhon, and A. Kis. Nonvolatile memory cells based on MoS_2/graphene heterostructures. *ACS Nano*, 7(4):3246–3252, 2013. 14

[78] L. Britnell, R.V. Gorbachev, R. Jalil, B.D. Belle, F. Schedin, A. Mishchenko, T. Georgiou, M.I. Katsnelson, L. Eaves, S.V. Morozov, et al. Field-effect tunneling transistor based on vertical graphene heterostructures. *Science*, 335(6071):947–950, 2012. 14

[79] B Radisavljevic, A Radenovic, J Brivio, V Giacometti, and A Kis. Single-layer MoS_2 transistors. *Nature nanotechnology*, 6(3):147–50, March 2011. ISSN 1748-3395. doi: 10.1038/nnano.2010.279. URL http://www.ncbi.nlm.nih.gov/pubmed/21278752. 14, 17, 19, 69, 105, 121

[80] Q.H. Wang, K. Kalantar-Zadeh, A. Kis, J.N. Coleman, and M.S. Strano. Electronics and optoelectronics of two-dimensional transition metal dichalcogenides. *Nature Nanotechnology*, 7(11):699–712, November 2012. ISSN 1748-3387. doi: 10.1038/nnano.2012.193. URL http://www.nature.com/doifinder/10.1038/nnano.2012.193. 14, 16, 19, 20, 24, 69, 71, 98, 103, 104

[81] B. Radisavljevic, M.B. Whitwick, and A. Kis. Integrated circuits and logic operations based on single-layer MoS_2. *ACS Nano*, 5(12):9934–8, December 2011. ISSN 1936-086X. doi: 10.1021/nn203715c. URL http://www.ncbi.nlm.nih.gov/pubmed/22073905. 14, 17, 69

[82] K. Alam and R.K. Lake. Monolayer MoS_2 transistors beyond the technology road map. *IEEE transactions on electron devices*, 59(12):3250–3254, 2012. URL http://cat.inist.fr/?aModele=afficheN&cpsidt=26690920. 14, 17, 19, 69

[83] M.L. Lin, L. Liu, Q. Lan, X. Tan, Kulwinder S Dhindsa, P. Zeng,

V.M. Naik, M.M.C. Cheng, and Z. Zhou. Mobility enhancement and highly efficient gating of monolayer MoS_2 transistors with polymer electrolyte. *Journal of Physics D: Applied Physics*, 45(34): 345102, August 2012. ISSN 0022-3727. doi: 10.1088/0022-3727/45/34/345102. URL http://stacks.iop.org/0022-3727/45/i=34/a=345102?key=crossref.4155cf9a31c6116e88e14e6ab335d2ce. 14, 69

[84] K.S. Novoselov, D. Jiang, F. Schedin, T.J. Booth, V.V. Khotkevich, S.V. Morozov, and A.K. Geim. Two-dimensional atomic crystals. *Proceedings of the National Academy of Sciences of the United States of America*, 102(30): 10451–3, July 2005. ISSN 0027-8424. doi: 10.1073/pnas.0502848102. URL http://www.pubmedcentral.nih.gov/articlerender.fcgi?artid=1180777&tool=pmcentrez&rendertype=abstract. 14, 69, 73, 76

[85] K.F. Mak, K. He, C. Lee, G.H. Lee, J. Hone, and T.F. Heinz. Tightly bound trions in monolayer MoS_2. 11(12):1–5, 2012. ISSN 1476-1122. doi: 10.1038/nmat3505. URL http://dx.doi.org/10.1038/nmat3505. 14, 21, 22, 23, 69, 70, 88, 89, 109, 121

[86] D. Xiao, G.B. Liu, W. Feng, X. Xu, and W. Yao. Coupled spin and valley physics in monolayers of MoS_2 and other group-VI dichalcogenides. *Physical Review Letters*, pages 1–5, 2012. URL http://link.aps.org/doi/10.1103/PhysRevLett.108.196802. 14, 23, 69

[87] H. Zeng, J.g Dai, W. Yao, D. Xiao, and X. Cui. Valley polarization in MoS_2 monolayers by optical pumping. *Nature nanotechnology*, 7(8):490–3,

August 2012. ISSN 1748-3395. doi: 10.1038/nnano.2012.95. URL http://www.ncbi.nlm.nih.gov/pubmed/22706701. 14, 23, 69

[88] T. Cao, G. Wang, W. Han, H. Ye, C. Zhu, J. Shi, Q. Niu, P. Tan, E. Wang, B. Liu, and J. Feng. Valley-selective circular dichroism of monolayer molybdenum disulphide. *Nature communications*, 3:887, January 2012. ISSN 2041-1723. doi: 10.1038/ncomms1882. URL http://www.ncbi.nlm.nih.gov/pubmed/22673914. 14, 23, 69

[89] S. Bertolazzi, J. Brivio, and A. Kis. Stretching and breaking of ultrathin MoS_2. *ACS Nano*, 5(12):9703–9, December 2011. ISSN 1936-086X. doi: 10.1021/nn203879f. URL http://www.ncbi.nlm.nih.gov/pubmed/22087740. 14

[90] H. Wang, L. Yu, Y.H. Lee, Y. Shi, A. Hsu, M.L. Chin, L.J. Li, M. Dubey, J. Kong, and T. Palacios. Integrated circuits based on bilayer MoS_2 transistors. *Nano Letters*, 12(9):4674–80, September 2012. ISSN 1530-6992. doi: 10.1021/nl302015v. URL http://www.ncbi.nlm.nih.gov/pubmed/22862813. 14, 19, 69, 70

[91] R.I Christy. Sputtered MoS_2 lubricant coating improvements. *Thin Solid Films*, 73(2):299 – 307, 1980. ISSN 0040-6090. doi: 10.1016/0040-6090(80)90493-9. URL http://www.sciencedirect.com/science/article/pii/0040609080904939. 15

[92] Y. Li, H. Wang, L. Xie, Y. Liang, G. Hong, and H. Dai. MoS_2 nanoparticles grown on graphene: An advanced catalyst for the hydrogen evolution reaction. *Journal of the American Chemical Society*, 133(19):7296–7299, 2011.

doi: 10.1021/ja201269b. URL http://pubs.acs.org/doi/abs/10.1021/ja201269b. 15

[93] G. Seifert, H. Terrones, M. Terrones, G. Jungnickel, and T Frauenheim. Structure and electronic properties of MoS_2 nanotubes. *Phys. Rev. Lett.*, 85:146–149, Jul 2000. doi: 10.1103/PhysRevLett.85.146. URL http://link.aps.org/doi/10.1103/PhysRevLett.85.146. 15

[94] E.S. Kadantsev and P. Hawrylak. Electronic structure of a single MoS_2 monolayer. *Solid State Communications*, 152(10):909–913, May 2012. ISSN 00381098. doi: 10.1016/j.ssc.2012.02.005. URL http://linkinghub.elsevier.com/retrieve/pii/S0038109812000889. 15, 20, 86

[95] T. Floyd. *Electronic Devices, Convential Current Version*. Pearson Eduction International, 2005. 16, 17

[96] M. Levinshtein and G. Simin. *Transistors: From Crystals to Integrated Circuits*. World Scientific Publishing, 1996. 17

[97] K. Kaasbjerg, K.S. Thygesen, and K.W. Jacobsen. Phonon-limited mobility in n-type single-layer MoS_2 from first principles. *Physical Review B*, 115317: 1–16, 2012. doi: 10.1103/PhysRevB.85.115317. URL http://prb.aps.org/abstract/PRB/v85/i11/e115317. 19, 104, 105

[98] D. Jena and A. Konar. Enhancement of Carrier Mobility in Semiconductor Nanostructures by Dielectric Engineering. *Physical Review Letters*, 98 (13):136805, March 2007. ISSN 0031-9007. doi: 10.1103/PhysRevLett.98.136805. URL http://link.aps.org/doi/10.1103/PhysRevLett.98.136805. 19, 105

[99] V. Podzorov and M.E. Gershenson. High-mobility field-effect transistors based on transition metal dichalcogenides. *Applied physics Letters*, 3301 (2004), 2004. doi: 10.1063/1.1723695. URL http://ieeexplore.ieee.org/xpls/abs_all.jsp?arnumber=4872587. 19, 96

[100] H. Peelaers and C. Van de Walle. Effects of strain on band structure and effective masses in MoS_2. *Physical Review B*, 86(24):241401, December 2012. ISSN 1098-0121. doi: 10.1103/PhysRevB.86.241401. URL http://link.aps.org/doi/10.1103/PhysRevB.86.241401. 19, 121

[101] H.P. Komsa and A. Krasheninnikov. Effects of confinement and environment on the electronic structure and exciton binding energy of MoS_2 from first principles. *Physical Review B*, 86(24):241201, December 2012. ISSN 1098-0121. doi: 10.1103/PhysRevB.86.241201. URL http://link.aps.org/doi/10.1103/PhysRevB.86.241201. 19, 20, 21, 86

[102] S. Bhattacharyya and A. Singh. Semiconductor-metal transition in semiconducting bilayer sheets of transition-metal dichalcogenides. *Physical Review B*, 86(7):1–7, August 2012. ISSN 1098-0121. doi: 10.1103/PhysRevB.86.075454. URL http://link.aps.org/doi/10.1103/PhysRevB.86.075454. 19

[103] G. Plechinger, F.X. Schrettenbrunner, J. Eroms, D. Weiss, C. Schueller, and T. Korn. Low-temperature photoluminescence of oxide-covered single-layer MoS_2. *physica status solidi (RRL)-Rapid Research Letters*, 6(3):126–128, 2012. 21, 22, 23, 70, 88, 108

[104] R. Wang, B.A. Ruzicka, and N. Kumar. Optical pump-probe studies of

carrier dynamics in few-layer MoS_2. *arXiv preprint arXiv: ...*, (October): 3–5, 2011. URL http://arxiv.org/abs/1110.6643. 21

[105] T. Olsen, K.W. Jacobsen, and K.S. Thygesen. Large Excitonic Effects in the Optical Properties of Monolayer MoS_2. *arXiv preprint arXiv:1107.0600*, pages 0–3, 2011. URL http://arxiv.org/abs/1107.0600http://adsabs.harvard.edu/abs/2011arXiv1107.0600O. 21, 86

[106] G.A.N. Connell, J.A. Wilson, and A.D. Yoffe. Effects of pressure and temperature on exciton absorption and band structure of layer crystals: Molybdenum disulphide. *Journal of Physics and Chemistry*, 30: 287–296, 1969. URL http://www.sciencedirect.com/science/article/pii/0022369769903102. 21

[107] Kin Fai Mak, Keliang He, Jie Shan, and Tony F Heinz. Control of valley polarization in monolayer MoS2 by optical helicity. *Nature nanotechnology*, 7(8):494–8, August 2012. ISSN 1748-3395. doi: 10.1038/nnano.2012.96. URL http://www.ncbi.nlm.nih.gov/pubmed/22706698. 22, 70, 88

[108] G. Sallen, L. Bouet, X. Marie, G. Wang, C. Zhu, W. Han, Y. Lu, P. Tan, T. Amand, B. Liu, and B. Urbaszek. Robust optical emission polarization in MoS_2 monolayers through selective valley excitation. *Physical Review B*, 86 (8):3–6, August 2012. ISSN 1098-0121. doi: 10.1103/PhysRevB.86.081301. URL http://link.aps.org/doi/10.1103/PhysRevB.86.081301. 22, 23, 86, 97

[109] C. Foot. *Atomic Physics*. Oxford Master Series, 2005. 28

[110] G. Binnig, C. F. Quate, and Ch. Gerber. Atomic force microscope. *Phys. Rev. Lett.*, 56:930–933, Mar 1986. doi: 10.1103/PhysRevLett.56.930. URL http://link.aps.org/doi/10.1103/PhysRevLett.56.930. 32

[111] K. Yamanaka, H. Ogiso, and O.V. Kolosov. Ultrasonic force microscopy for nanometer resolution subsurface imaging. *Applied Physics Letters*, 64 (2):178, 1994. ISSN 00036951. doi: 10.1063/1.111524. URL http://link.aip.org/link/APPLAB/v64/i2/p178/s1&Agg=doi. 33

[112] A. P. McGuigan, B. D. Huey, G. A. D. Briggs, O. V. Kolosov, Y. Tsukahara, and M. Yanaka. Measurement of debonding in cracked nanocomposite films by ultrasonic force microscopy. *Applied Physics Letters*, 80(7):1180, 2002. ISSN 00036951. doi: 10.1063/1.1450058. URL http://link.aip.org/link/APPLAB/v80/i7/p1180/s1&Agg=doi. 33

[113] O. Kolosov, F. Dinelli, and A. Krier. Seeing the invisible-ultrasonic force microscopy for true subsurface elastic imaging of semiconductor nanostructures with nanoscale resolution. *Proceedings of Techconnectworld-2012, Nanotech-2012,(Santa Clara, USA, 2012)*, 1: 24–26, 2012. URL http://www.nano-science.com/docs/d-pub-prs/12-pub-ufm-subsurface-nanotech-2012-1303.pdf. 34, 79

[114] D.B. Williams and C.B. Carter. *The Transmission Electron Microscope*. Springer, 1996. 35

[115] D.P Woodruff. *Modern Techniques of Surface Science*. Cambridge University Press, 1994. 35

[116] N.D. Browning, M.F. Chisholm, and S.J. Pennycook. Atomic-resolution chemical analysis using a scanning transmission electron microscope. *Nature*, 366(6451):143–146, 1993. 35

[117] K. Pemasiri, M. Montazeri, R. Gass, L. M Smith, H.E. Jackson, J. Yarrison-rice, S. Paiman, Q. Gao, H.H. Tan, C. Jagadish, X. Zhang, and J. Zou. Carrier dynamics and quantum confinement in type II ZB-WZ InP nanowire homostructures 2009. *Nano*, 2009. 39, 52

[118] J. Qi, Angela M. Belcher, and J.M. White. Spectroscopy of individual silicon nanowires. *Applied Physics Letters*, 82(16):2616–2618, 2003. 39

[119] S. Piscanec, M. Cantoro, A.C. Ferrari, J.A. Zapien, Y. Lifshitz, S.T. Lee, S. Hofmann, and J. Robertson. Raman spectroscopy of silicon nanowires. *Physical Review B*, 68(24):241312–R, 2003. 39

[120] I. J. Luxmoore, E. D. Ahmadi, N. A. Wasley, A. M. Fox, A. I. Tartakovskii, A. B. Krysa, and M. S. Skolnick. Control of spontaneous emission from InP single quantum dots in GaInP photonic crystal nanocavities. *Applied Physics Letters*, 97(18):181104, 2010. ISSN 00036951. doi: 10.1063/1.3510469. URL http://link.aip.org/link/APPLAB/v97/i18/p181104/s1&Agg=doi. 39

[121] E.D. Minot, F. Kelkensberg, M. Van Kouwen, J.A. Van Dam, L.P. Kouwenhoven, V. Zwiller, M.T. Borgström, O. Wunnicke, M.A. Verheijen, and E.P. Bakkers. Single quantum dot nanowire LEDs. *Nano Letters*, 7(2):367–371, 2007. 39

[122] M.-E. Pistol and C. Pryor. Band structure of segmented semiconductor nanowires. *Physical Review B*, 80(3), July 2009. ISSN 1098-0121. doi: 10.1103/PhysRevB.80.035316. URL http://link.aps.org/doi/10.1103/PhysRevB.80.035316. 39

[123] M. Makhonin, A.P. Foster, A. Krysa, and P. Fry. Homogeneous array of nanowire-embedded quantum light emitters. *Nanoletters*, 2013. URL http://pubs.acs.org/doi/abs/10.1021/nl303075q. 39

[124] A. Aierken, J. Riikonen, M. Mattila, T. Hakkarainen, M. Sopanen, and H. Lipsanen. GaAs surface passivation by ultra-thin epitaxial GaP layer and surface AsP exchange. *Applied Surface Science*, 253(14):6232–6235, May 2007. ISSN 01694332. doi: 10.1016/j.apsusc.2007.01.069. URL http://linkinghub.elsevier.com/retrieve/pii/S0169433207001407. 41, 58

[125] E. Tournie and A. Trampert. MBE growth and interface formation of compound semiconductor heterostructures for optoelectronics. *Physica Status Solidi (B)*, 244(8):2683–2696, 2007. ISSN 1521-3951. doi: 10.1002/pssb.200675623. URL http://dx.doi.org/10.1002/pssb.200675623. 43

[126] B.A. Joyce. Molecular beam epitaxy. *Reports on Progress in Physics*, 48 (12):1637, 1985. URL http://stacks.iop.org/0034-4885/48/i=12/a=002. 43

[127] Wendy L Sarney. *Understanding Transmission Electron Microscopy Diffraction Patterns Obtained From Infrared Semiconductor Materials*. Army Research Laboratory, 2003. 47

[128] J. Bao, D.C. Bell, F. Capasso, J.B. Wagner, T. Må rtensson, J. Tr ä g årdh, and L. Samuelson. Optical properties of rotationally twinned InP nanowire heterostructures. *Nano Letters*, 8(3):836–41, March 2008. ISSN 1530-6984. doi: 10.1021/nl072921e. URL http://www.ncbi.nlm.nih.gov/pubmed/18275163. 47, 52

[129] R. Gurwitz, A. Tavor, L. Karpeles, I. Shalish, W. Yi, G. Seryogin, and V. Narayanamurti. Bandgap and band discontinuity in wurtzite/zincblende GaAs homomaterial heterostructure. *Applied Physics Letters*, 100(19): 191602, 2012. doi: 10.1063/1.4712562. URL http://link.aip.org/link/?APL/100/191602/1. 51

[130] L.C. Andreani, F. Tassone, and F. Bassani. Radiative lifetime of free excitons in quantum wells. *Solid State Communications*, 77(9):641–645, 1991. 54

[131] M. Skowronski, S. T. Neild, and R. E. Kremer. Location of energy levels of oxygen-vacancy complex in GaAs. *Applied Physics Letters*, 57(9):902, 1990. ISSN 00036951. doi: 10.1063/1.103399. URL http://link.aip.org/link/APPLAB/v57/i9/p902/s1&Agg=doi. 59

[132] D. Bimberg, M. Sondergeld, and E. Grobe. Thermal dissociation of excitons bounds to neutral acceptors in high-purity GaAs. *Phys. Rev. B*, 4:3451–3455, Nov 1971. doi: 10.1103/PhysRevB.4.3451. URL http://link.aps.org/doi/10.1103/PhysRevB.4.3451. 63

[133] M.M. Benameur, B. Radisavljevic, J.S. Héron, S. Sahoo, H. Berger, and A. Kis. Visibility of dichalcogenide nanolayers. *Nanotechnology*, 22(12):

125706, March 2011. ISSN 1361-6528. doi: 10.1088/0957-4484/22/12/125706. URL http://www.ncbi.nlm.nih.gov/pubmed/21317494. 69, 78

[134] E. Stolyarova, D. Stolyarov, K. Bolotin, S. Ryu, L. Liu, K.T. Rim, M. Klima, M. Hybertsen, I. Pogorelsky, and I. Pavlishin. Observation of graphene bubbles and effective mass transport under graphene films. *Nano Letters*, 9(1):332–337, 2008. 70, 71, 79, 81

[135] Masa Ishigami, JH Chen, WG Cullen, MS Fuhrer, and ED Williams. Atomic structure of graphene on SiO_2. *Nano Letters*, 7(6):1643–1648, 2007. 70, 79, 82

[136] T. Li and Z. Zhang. Substrate-regulated morphology of graphene. *Journal of Physics D: Applied Physics*, 43(7):075303, 2010. 70, 79

[137] C. Lee, Q. Li, W. Kalb, X.Z. Liu, H. Berger, R.W. Carpick, and J. Hone. Frictional characteristics of atomically thin sheets. *Science (New York, N.Y.)*, 328(5974):76–80, April 2010. ISSN 1095-9203. doi: 10.1126/science.1184167. URL http://www.ncbi.nlm.nih.gov/pubmed/20360104. 70, 79

[138] J. Brivio, D.T.L. Alexander, and A. Kis. Ripples and layers in ultrathin MoS_2 membranes. *Nano Letters*, 11(12):5148–53, December 2011. ISSN 1530-6992. doi: 10.1021/nl2022288. URL http://www.ncbi.nlm.nih.gov/pubmed/22010987. 70

[139] Goki Eda, Hisato Yamaguchi, Damien Voiry, Takeshi Fujita, Mingwei Chen, and Manish Chhowalla. Photoluminescence from chemically exfoliated MoS_2. *Nano Letters*, 11(12):5111–6, December 2011. ISSN 1530-6992.

doi: 10.1021/nl201874w. URL http://www.ncbi.nlm.nih.gov/pubmed/22196516. 70, 73

[140] H.S.S Matte, A. Gomathi, A.K Manna, D.J. Late, R. Datta, S.K. Pati, and C.N.R. Rao. MoS_2 and WS_2 analogues of graphene. *Angewandte Chemie (International ed. in English)*, 49(24):4059–62, June 2010. ISSN 1521-3773. doi: 10.1002/anie.201000009. URL http://www.ncbi.nlm.nih.gov/pubmed/20425874. 73

[141] Y. Lee, X.Q. Zhang, W. Zhang, M. Chang, C. Lin, Y. Yu, J. T. Wang, C. Chang, L. Li, and T. Lin. Synthesis of large-area MoS_2 atomic layers with chemical vapor deposition. *Chemical Vapor Deposition*, pages 1–9. 73

[142] J.N. Coleman, M. Lotya, A. O. Neill, S.D. Bergin, P.J. King, U. Khan, K. Young, A. Gaucher, S. De, R.J. Smith, I.V. Shvets, S.K. Arora, G. Stanton, H. Kim, K. Lee, G.T. Kim, G.S. Duesberg, T. Hallam, J.J. Boland, J.J. Wang, J.F. Donegan, J.C. Grunlan, G. Moriarty, A. Shmeliov, R.J. Nicholls, J.M. Perkins, E.M Grieveson, K. Theuwissen, D.W. Mccomb, P.D. Nellist, and V. Nicolosi. Produced by Liquid Exfoliation of Layered Materials. *Science*, 331(February):568–571, 2011. 73

[143] Won Seok Yun, S. Han, Soon Cheol Hong, In Gee Kim, and J. Lee. Thickness and strain effects on electronic structures of transition metal dichalcogenides: 2H-MX_2 semiconductors (M = Mo, W; X = S, Se, Te). *Physical Review B*, 85(3):033305, January 2012. ISSN 1098-0121. doi: 10.1103/PhysRevB.85.033305. URL http://link.aps.org/doi/10.1103/PhysRevB.85.033305. 78, 82

[144] K. He, C. Poole, K.F. Mak, and J. Shan. Experimental demonstration of continuous electronic structure tuning via strain in atomically thin MoS_2. *Nano Letters*, 2013. 82, 121

[145] H.J. Conley, B. Wang, J.I. Ziegler, R.F. Haglund Jr, S.T. Pantelides, and K.I. Bolotin. Bandgap engineering of strained monolayer and bilayer MoS_2. *arXiv preprint arXiv:1305.3880*, 2013. 82, 121

[146] C.R. Dean, A.F. Young, I. Meric, C. Lee, L. Wang, S. Sorgenfrei, K. Watanabe, T. Taniguchi, P. Kim, and K.L. Shepard. Boron nitride substrates for high-quality graphene electronics. *Nature nanotechnology*, 5(10):722–726, 2010. 83, 104

[147] Y.P. Varshni. Temperature dependence of the energy gap in semiconductors. *Physica*, 34(1):149–154, 1967. 92

[148] Yijin Zhang, Jianting Ye, Yusuke Matsuhashi, and Yoshihiro Iwasa. Ambipolar MoS_2 thin flake transistors. *Nano Letters*, 12(3):1136–40, March 2012. ISSN 1530-6992. doi: 10.1021/nl2021575. URL http://www.ncbi.nlm.nih.gov/pubmed/22276648. 96, 121

[149] Kapildeb Dolui, Ivan Rungger, and Stefano Sanvito. Origin of the n-type and p-type conductivity of MoS_2 monolayers on a SiO_2 substrate. *arXiv preprint arXiv:1301.2491*, 2013. URL http://arxiv.org/abs/1301.2491. 96, 121

[150] K.I. Bolotin, K.J. Sikes, Z.D. Jiang, M. Klima, G. Fudenberg, J. Hone, P. Kim, and H.L. Stormer. Ultrahigh electron mobility in suspended graphene. *Solid State Communications*, 146(9):351–355, 2008. 104

[151] E.H. Hwang and S.D. Sarma. Acoustic phonon scattering limited carrier mobility in two-dimensional extrinsic graphene. *Physical Review B*, 77(11): 115449, 2008. 104

[152] Lei Liao, Jingwei Bai, Yongquan Qu, and Yung-chen Lin. High-κ oxide nanoribbons as gate dielectrics for high mobility top-gated graphene transistors. *PNAS*, 107(15):6711–6715, 2010. doi: 10.1073/pnas.0914117107. URL http://www.pnas.org/content/107/15/6711.short. 105

[153] R. Yan, S. Bertolazzi, J. Brivio, and T. Fang. Raman and Photoluminescence Study of Dielectric and Thermal Effects on Atomically Thin MoS2. *arXiv preprint arXiv: ...*, pages 1–15, 2012. URL http://arxiv.org/abs/1211.4136. 105

[154] A. Boogaard, A.Y. Kovalgin, and R.A.M. Wolters. Net negative charge in low-temperature SiO_2 gate dielectric layers. *Microelectronic engineering*, 86 (7):1707–1710, 2009. 121

[155] Xin Zhou, Qin Chen, QM Zhang, and Shihai Zhang. Dielectric behavior of bilayer films of P(VDF-CTFE) and low temperature PECVD fabricated Si_3N_4. *Dielectrics and Electrical Insulation, IEEE Transactions on*, 18(2): 463–470, 2011. 121